

DEVELOPMENT OF A STATIONARY DIGITAL BREAST TOMOSYNTHESIS SYSTEM
FOR CLINICAL APPLICATIONS

Andrew Wallace Tucker

A dissertation submitted to the faculty of the University of North Carolina at Chapel Hill in
partial fulfillment of the requirements for the degree of Doctor of Philosophy in the
Department of Biomedical Engineering.

Chapel Hill
2014

Approved by:

David Lalush

Otto Zhou

Paul Dayton

Cherie Kuzmiak

Jianping Lu

© 2014
Andrew Wallace Tucker
ALL RIGHTS RESERVED

ABSTRACT

ANDREW WALLACE TUCKER: Development of a Stationary
Digital Breast Tomosynthesis System for Clinical Applications
(Under the direction of Otto Z. Zhou)

Digital breast tomosynthesis (DBT) has been shown to be a very beneficial tool in the fight against breast cancer. However, current DBT systems have poor spatial resolution compared to full field digital mammography (FFDM), the current gold standard for screening mammography. The poor spatial resolution of DBT systems is a result of the single X-ray source design. In DBT systems a single X-ray source is rotated over an angular span in order to acquire the images needed for 3D reconstruction. The rotation of the X-ray source degrades the spatial resolution of the images. DBT systems which are approved for use in the United States for screening mammography are required to also take a full field digital mammogram with every DBT acquisition in order to compensate for the poor spatial resolution. This double exposure essentially doubles the radiation dose to patients.

Over the past few years our research group has developed a carbon nanotube (CNT) based X-ray source technology. The unique nature of CNT X-ray sources allows for multiple X-ray focal spots in a single X-ray source. Using this technology we have recently developed a stationary DBT system (s-DBT) system which is capable of producing a full tomosynthesis image dataset with zero motion of the X-ray source. This system has been shown to have increased spatial resolution over other DBT systems in a laboratory setting. The goal of this thesis work was to optimize the s-DBT system, demonstrate its usefulness over other systems, and finally implement it into the clinic for a clinical trial.

The s-DBT system was optimized using different image quality measurements. The optimized system was then used in a breast specimen imaging trial which compared s-DBT to

magnified 2D mammography and a conventional single source DBT system. Readers preferred s-DBT to magnified 2D mammography for specimen margin delineation and mass detection, these results were not significant. Using physical measures for spatial resolution the s-DBT system was shown to have improved image quality over conventional single source DBT systems in breast tissue. A separate study showed that s-DBT could be a feasible alternative to FFDM for screening patients with breast implants. Finally, a second s-DBT system was constructed and implemented into the Department of Mammography at UNC hospitals. The first patient was imaged on the system in December of 2013.

ACKNOWLEDGEMENTS

I would like to thank my advisor, Dr. Otto Zhou, for his leadership and guidance through my graduate studies. Dr. Zhou has shown a great dedication to the advancement of mammographic imaging. His continued research into the field will one day enable breast cancer to be detected at an early stage thus saving countless lives. I would also like to thank each member of our research group that has helped me through my studies including; Laurel Burk, Jabari Calliste, Guohua Cao, Pavel Chtcheprov, Emily Gidcumb, Mike Hadsell, Christy Inscoe, Marci Potuzco, Xin Qian, Jing Shan, Jerry Zhang, and Lei Zhang. I would personally like to thank Dr. Jianping Lu and Dr. Yueh Lee, without your helpful guidance and insight into my research I would not have been able to complete this endeavor. I would also like to thank each member of my Ph.D. committee for their insight and direction. Dr. Lalush, thank you for your advisement during both my undergraduate studies at NC State and my graduate studies at UNC. I would like to give a special thanks to Dr. Etta Pisano, although I did not get to finish my research under your advisement, I am eternally thankful for the opportunity you gave me in breast cancer research which lead me on the path to my Ph.D.

During my graduate studies I have had many collaborative efforts with our industrial sponsor, Hologic Inc. I would like to thank everyone at Hologic who has helped with implementation of my research into the clinic at UNC. I would also like to thank all of the employees in the Department of Mammography at UNC Hospitals who have helped me countless times during the multiple trials I conducted there. Dr. Cherie Kuzmiak, words cannot express the thanks I have for all the help you have given me. I am so thankful to have been able to work with you and I hope you continue to do the great work you do in the field of mammography.

Finally, I would like to thank all my friends and family for their support throughout my academic career. Mom and Dad, I am so grateful for all the love and support you have given me. I thank you so much for teaching me the value of an education. Brianna, my beautiful wife, thank you for staying by my side through countless late nights and years of school. I love you so much and I could not have done this without you.

TABLE OF CONTENTS

LIST OF TABLES.....	xv
LIST OF FIGURES	xvii
LIST OF ABBREVIATIONS.....	xxiv
Chapter 1: INTRODUCTION.....	1
1.1 Dissertation Overview.....	1
1.2 Specific Aims.....	3
1.3 Dissertation Organization	5
REFERENCES.....	7
Chapter 2: X-RAY PRODUCTION AND INTERACTIONS IN MATTER	9
2.1 Overview	9
2.2 Discovery of X-rays	9
2.3 X-ray Production.....	10
2.3.1 Bremsstrahlung X-rays.....	10
2.3.2 Characteristic X-rays.....	12
2.4 X-ray Tube Design.....	13
2.4.1 The Cathode	14
2.4.2 The Anode	16
2.4.3 Tube Housing.....	17

2.4.4 Effective Focal Spot	19
2.5 X-ray Interactions in Matter.....	19
2.5.1 Photoelectric Absorption	19
2.5.2 Rayleigh Scatter.....	20
2.5.3 Compton Scatter	21
2.5.4 Pair Production	22
2.5.5 Attenuation Coefficient	22
REFERENCES.....	24
Chapter 3: MAMMOGRAPHIC IMAGING FUNDAMENTALS	25
3.1 Overview	25
3.2 The Human Breast	25
3.2.1 Female Breast Anatomy and Positioning.....	25
3.2.2 Breast Density.....	27
3.2.3 Masses	29
3.2.4 Microcalcifications.....	30
3.3 Image Quality	31
3.3.1 Contrast	31
3.3.2 Spatial Resolution	34
3.3.3 Noise.....	37
3.4 Image Interpretation	39
REFERENCES.....	42

Chapter 4: MAMMOGRAPHIC IMAGING MODALITIES	43
4.1 Overview	43
4.2 Screening Mammography Modalities	43
4.2.1 Screen Film Mammography	43
4.2.2 Full Field Digital Mammography	44
4.2.3 Digital Breast Tomosynthesis	47
4.3 Adjunct Mammographic Imaging Modalities.....	48
4.3.1 Ultrasound	48
4.3.2 Magnetic Resonance Imaging	49
4.4 Major Investigative Modality.....	50
4.4.1 Computed Tomography	50
REFERENCES.....	53
Chapter 5: CARBON NANOTUBE BASED X-RAY SOURCES	56
5.1 Overview	56
5.2 Field Emission from CNTs Versus Thermionic Emission	56
5.3 CNT Based X-ray Sources	59
5.4 Applications of CNT Based X-ray Sources.....	62
5.4.1 Micro-Computed Tomography.....	63
5.4.2 Micro-Beam Radiation Therapy.....	66
5.4.3 Chest Tomosynthesis.....	68
5.4.4 Computed Tomography	69

5.4.5 Digital Breast Tomosynthesis	70
REFERENCES.....	72
Chapter 6: STATIONARY DIGITAL BREAST TOMOSYNTHESIS	76
6.1 Overview	76
6.2 Motivation for a Stationary System	76
6.3 First Prototype System	77
6.3.1 CNT Source Array.....	78
6.3.2 Detector	78
6.3.3 Switching System.....	79
6.3.4 Images	79
6.4 Second Prototype System	79
6.4.1 CNT Source Array.....	80
6.4.2 Selenia Dimensions Components	83
6.4.3 Images	83
6.5 Conclusion.....	87
REFERENCES.....	88
Chapter 7: OPTIMIZATION OF AN S-DBT SYSTEM	90
7.1 Overview	90
7.2 Motivation for System Optimization.....	91
7.3 Methods	92
7.3.1 Configuration Parameters	92

7.3.2 Entrance Dose	93
7.3.3 Phantom Imaging	94
7.3.4 Image Processing and Reconstruction	95
7.3.5 Modulation Transfer Function Calculation	96
7.3.6 Signal Difference to Noise Ratio Calculation	96
7.3.7 Artifact Spread Function Analysis.....	97
7.3.8 Overall Image Quality Factor.....	98
7.4 Results	98
7.4.1 Modulation Transfer Function.....	99
7.4.2 Signal Difference to Noise Ratio.....	100
7.4.3 Artifact Spread Function Along the Z-Axis	101
7.4.4 Detector Pixel Size Comparison.....	103
7.4.5 Overall Image Quality Factor.....	104
7.5 Discussion	105
7.6 Conclusions.....	107
REFERENCES.....	108
Chapter 8: BREAST SPECIMEN IMAGING WITH S-DBT	109
8.1 Overview	109
8.2 Motivation for Specimen Imaging.....	110
8.3 Methods	110
8.3.1 Patient Recruitment.....	110

8.3.2 Imaging on the s-DBT System.....	111
8.3.3 Reader Study Design	111
8.4 Results	112
8.5 Discussion	115
8.6 Conclusion.....	117
REFERENCES.....	119
Chapter 9: HIGH RESOLUTION MICROCALCIFICATION IMAGING WITH S-DBT	120
9.1 Overview	120
9.2 Motivation	121
9.3 Methods	122
9.3.1 Stationary digital breast tomosynthesis system	122
9.3.2 Continuous motion digital breast tomosynthesis system.....	124
9.3.3 Imaging protocol	124
9.3.4 Image processing and reconstruction.....	124
9.3.5 Microcalcification analysis	125
9.3.6 Simulated 3D modulation transfer function	126
9.4 Results	128
9.4.1 Microcalcification analysis	128
9.4.2 Simulated 3D modulation transfer function	129
9.5 Discussion	132
9.6 Conclusions.....	133

REFERENCES.....	134
Chapter 10: FEASIBILITY OF S-DBT AS A SCREENING TOOL FOR PATIENTS WITH AUGMENTATION MAMMOPLASTY	136
10.1 Overview	136
10.2 Motivation for Implant Imaging.....	137
10.3 Methods.....	138
10.3.1 Augmentation Mammoplasty Models.....	139
10.3.2 Imaging Configuration	140
10.3.3 Image Processing and Reconstruction	141
10.3.4 Image Analysis.....	141
10.4 Results	144
10.4.1 Masses	145
10.4.2 Fibers.....	146
10.4.3 Spec Clusters.....	147
10.5 Discussion	148
10.6 Conclusions.....	149
REFERENCES.....	150
Chapter 11: CLINICAL IMPLEMENTATION OF AN S-DBT SYSTEM	151
11.1 Overview	151
11.2 Motivation for Clinical Implementation	151
11.3 System Construction and Installation.....	152
11.4 Patient and Operator Safety	154

11.4.1 Electrical Safety	155
11.4.2 Radiation Safety	157
11.4.3 Institutional Review Board Approval	158
11.5 System Characterization	158
11.5.1 Geometry Calibration	159
11.5.2 Spatial Resolution	161
11.5.3 Current Versus Voltage Curve	162
11.5.4 Dose Rate	163
11.6 Patient Imaging	164
11.7 Conclusion	166
REFERENCES	167
Chapter 12: SUMMARY AND IMPLICATIONS	168
12.1 Overview	168
12.2 Summary of Research	169
12.2.1 Optimization of an s-DBT System	169
12.2.2 Breast Specimen Imaging with s-DBT	170
12.2.3 High Resolution Microcalcification Imaging with s-DBT	172
12.2.4 Feasibility of s-DBT as a Screening Tool for Patients with Augmentation Mammoplasty	173
12.2.5 Clinical Implementation of an s-DBT System	175
12.3 Implications	176
REFERENCES	178

LIST OF TABLES

Table 1: Linear attenuation coefficient for various materials at an energy of 50 keV. As the electron density increases the probability of photon interaction increases thus the linear attenuation coefficient increases. Table is recreated from data from Bushberg et al. ²²	23
Table 2: BI-RADS breast density classifications. Data taken from Baker et al. ³⁵	28
Table 3: Typical lesions with their associated locations and disease. Data taken from Kopans. ³¹	29
Table 4: BI-RADS classifications of malignancy. Data taken from Eberl et al. ³⁶	30
Table 5: MC types and their associated diagnosis. Data taken from Baker et al. ³⁵	30
Table 6: Determination of TP, TN, FP, and FN base off disease truth and diagnosis.....	40
Table 7: List of configurations and parameters that were analyzed. Five parameters were changed in order to create different configurations; number of projection views, total angular span, entrance dose, distribution of the mAs, and detector resolution. Some configurations are described by multiple groups and therefore appear multiple times in the table. Differences in entrance dose for equal mAs values can be attributed to different source to object distances for different x-ray sources. MMOC stands for more mAs on central projections. LMOC stands for less mAs on central projections.....	93
Table 8: Calculated results for SdNR, FWHM of the ASF, and MTF. Data is separated into the five groups of configurations that were outlined in Section 7.3.1 . The configuration with 29 projection views, a 28 degree angular span, and an even dose distribution resulted in the highest “QF” value for an exposure of 100 mAs. MMOC stands for more mAs on central projections. LMOC stands for less mAs on central projections.	99
Table 9: Calculated sensitivity and specificity values by modality and reader. Values were calculated from malignancy scores. Malignancy scores from 3 to 5 were considered positive for disease.	113
Table 10: Average reader preference for the shape/morphology of masses, MC assessment, and margin assessment. Positive values represent a preference for stationary digital breast tomosynthesis compared to 2D mammography.	113

Table 11: Results of the secondary analysis performed on the preference portion of the reader study. It was tested whether the mean preference was larger than zero using a linear mixed model with a random intercept effect and Wald test.....	115
Table 12: The results of the MC area calculation and ASF for all 12 individual MCs that were analyzed. FWHM stands for the full width at half maximum of the ASF.....	128
Table 13: Imaging configurations for each augmentation mammoplasty model used. Each configuration corresponds to an exposure index between -35 and -25 on the Selenia Dimensions in 2D imaging mode.	140
Table 14: Average number of lesions counted by reader one and two for both imaging modalities. The configuration number is related to the implant model and will be used in later plots for ease of implementation.....	145
Table 15: List of major system components other than the X-ray tube in the s-DBT system.....	153
Table 16: Peak current draw and electrical input ratings for power generating components of the system.....	157
Table 17: Measured entrance dose for all three configurations and various anode-cathode potentials. The dose rate was calculated by dividing the entrance dose by the total mAs.	164

LIST OF FIGURES

Figure 1: Diagram of three different electron interactions in an atom where Bremsstrahlung radiation would be produced. The numbers indicate locations of X-ray production in order of increasing energy lost. The farther the electron is from the nucleus the less energy is converted to X-rays. This image is for demonstrative purposes and does not represent actual interactions or atoms. Image is modeled after a figure from Bushberg et al.. ²²	11
Figure 2: Simulation of an energy spectrum from a X-ray source with a tungsten target and 1 mm of tungsten filtration. The applied potential difference was 120 kVp. Both the characteristic K_{α} and K_{β} X-ray peaks are labeled as well as the Bremsstrahlung curve. The zoomed in region shows the k edge which is the energy at which the attenuation coefficient of tungsten increases due to the photoelectric absorption of electrons.	13
Figure 3: Diagram of a modern X-ray tube. The major components of an X-ray tube are the cathode, the anode, and the tube housing. The combination of the anode target angle and the anode viewing angle can change the effective focal spot on the detector, thus changing the resolution of the image.	14
Figure 4: Diagram depicting the effect of anode angle on X-ray FOV. In the diagram, the green lines represent electron beams and the red lines represent X-ray beams. The small anode angle on the left results in a small FOV on the detector while the large anode angle on the right results in a large FOV on the detector. Anode angles are exaggerated for demonstrative purposes.....	17
Figure 5: Diagram of the major and surrounding structures of the female breast. Each structure is labeled. Image has been adapted to point to the structures. Original image is copyright Patrick J. Lynch, medical illustrator; and C. Carl Jaffe, MD, cardiologist. And is reprinted with permission from the copyrighter based on the Creative Commons Attribution from Wikipedia.com.	26
Figure 6: Diagram showing the non-uniformity of breast thickness that occurs even after compression of the breast. The air gaps in the image produce differing levels of X-ray intensity on the detector.....	27
Figure 7: Example 2D projection radiographs of breasts with each BI-RADS density classification. Moving from left to right the densities become more dense. This image is reprinted with permission from Dr. Cherie Kuzmiak from UNC Hospitals.....	28
Figure 8: Demonstration of the effect of the attenuation coefficient on the contrast of an image. The green attenuating object will	

attenuate twice the amount of X-rays at the given energy than the blue object. The image on the Left shows that when the objects have the same thickness contrast between the two objects can be seen. However, the image on the Right shows that if the green object has half the thickness of the blue object there is no contrast between the two. This is for demonstrative purposes and does not necessarily represent an actual imaging system.	32
Figure 9: Left - An MLO image of a breast (Above) without adjusting the image (Below). Right - Same image (Above) with adjustment of the histogram (Below). The red bars on the original histogram show the window at which the changed histogram is contained in. This case is greatly exaggerated.	34
Figure 10: Illustration of the effect of radiographic magnification on the penumbra of a non-ideal focal spot. Ideal focal spots are not possible in X-ray tubes so this effect is visible in every radiographic imaging system.	37
Figure 11: A ROC curve that shows a system that has an accuracy of 50%. If such a system existed, a random guess of diagnosis would give you the same results as diagnosing based off the system.	41
Figure 12: Schematic of a typical CNT based X-ray source. Where "C" is the cathode structure, "G" is the gate electrode, "F1" and "F2" are focusing electrodes, "A" is the anode, " V_{gc} " is applied gate cathode voltage, and " V_{anode} " is the applied anode voltage.	60
Figure 13: Image of the final design of the CNT based micro-CT system, Charybdis.	63
Figure 14: A 3D visualization of the lungs of a mouse imaged on the CNT based micro-CT system.	64
Figure 15: Left - Reconstruction of a micro-CT dataset of a mouse which was gated to both the cardiac and respiratory cycle. All four chambers of the heart are visible. Right - Reconstruction of a micro-CT dataset of a mouse pup using the non-contact sensor.	65
Figure 16: Image of the desktop CNT based MRT system.	67
Figure 17: Histological image of microbeam DNA damage in a mouse brain with human brain tumor. Cell staining was done with γ -H2AX labeling four hours after radiation.	68
Figure 18: Left - Image of the prototype stationary chest tomosynthesis system. Right - Reconstruction slice of a chest phantom using the system.	69

Figure 19: Left - Image of the prototype s-DBT system. Right - Reconstruction slice of a breast phantom using the s-DBT system.	71
Figure 20: First prototype s-DBT system.	77
Figure 21: The X-ray spectrum of the first prototype s-DBT system. The Mo/Mo anode filter combination produces characteristic peaks at 17.48 and 19.61 keV.	78
Figure 22: Reconstruction slices of a breast phantom from the first prototype s-DBT system. The slices are at the heights of (a) 6 mm, (b) 11 mm, (c) 16 mm, and (d) 21 mm.	79
Figure 23: Image of the second prototype s-DBT system.	80
Figure 24: X-ray spectra of the second prototype s-DBT system at 40 keV peak energy. The characteristic peaks of the W/Al anode filter combination are at higher energies than 40 keV and therefore do not appear in the spectra.	81
Figure 25: Above - Gate-cathode voltages for the CNT source array at a cathode current of 43mA. The average value was approximately 1.4 kV. Below - Measured nominal focal spot sizes. The average focal spot size was found to be 0.64x0.61 mm.	82
Figure 26: Plot of the transmission rates of each X-ray source in the prototype. The average transmission rate is 61%.	83
Figure 27: Left - Schematic of the structures contained in the ACR mammography accreditation phantom. Right - Schematic of the target slab in the BR3D tomosynthesis phantom.	84
Figure 28: Projection images from beam N14 (Left), 000 (Middle), and P14 (Right) of the ACR phantom from the s-DBT prototype. Images were taken at 30 kVp and 100 mAs total exposure.	85
Figure 29: Reconstruction slice of the ACR phantom dataset. When using fidelity display all fibers and masses are visible in this dataset and four groups of specs.	85
Figure 30: Projection images from beam N14 (Left), 000 (Middle), and P14 (Right) of the BR3D phantom from the s-DBT prototype. There is a large amount of tissue overlap present in the images which will be removed in the reconstruction slices.	86
Figure 31: Reconstruction slice of the ACR phantom dataset. Compared to the projection images Figure 30 most of the underlying and overlying tissue has been removed in the reconstruction.	87

Figure 32: Left: Schematic of simulated masses MCs and fibers located in the ACR phantom. Analysis was conducted on the masses and MCs. Right: ACR phantom reconstructed slice acquired using the s-DBT system.....	95
Figure 33: Left: Plot of an oversampled LSF and the corresponding Gaussian fitted LSF which was used for MTF calculations. Right: MTF of the LSF with the value at 10% highlighted. The MTF was found to be around 4.2 cycles per mm for a detector with a 140 μm pixel size (2x2 binning mode). Since there is no x-ray source motion in an s-DBT system the MTF is found to be primarily dependent on the detector pixel size, and independent of other system parameters (see Figure 38).	100
Figure 34: Left: Magnified view of 2 mm mass found in the ACR phantom. The SdNR of the mass and the surrounding background was calculated for each configuration. Right: Magnified view of the 0.54 mm speck cluster found in the ACR phantom. ASF analysis was completed on all specks in the cluster for each configuration.	101
Figure 35: The plot of the SdNR versus total entrance dose shows a linear increase of the SdNR with entrance dose within the dose range examined. A linear fit was applied to the dataset and plotted.....	101
Figure 36: Plot of the ASF of an angular span of 14 degrees versus an angular span of 28 degrees with the same number of projection images and total entrance dose. Both the raw data and the fitted data are shown. The 14 degree span resulted in a much broader ASF due to the lack of information in the projection space.	103
Figure 37: Results comparing the FWHM of the ASF and the total angular span of the projection images. A smooth fit was also applied to the data and plotted. A very noticeable trend can be seen which shows that an increased angular span results in a better artifact spread function.....	103
Figure 38: Plot of the MTFs for the 70 μm pixel size and the 140 μm pixel size. The value of the MTF at 10% was found to be approximately 25% better for the 70 μm pixel size (5.1 cycles per mm) when compared to the 140 μm case (4.1 cycles per mm).	104
Figure 39: Left - Segmented 2D radiograph of container used to hold specimens. Right - Image of an s-DBT system with specimen container on the detector housing.	111
Figure 40: Left Above - Reconstructed slice of a specimen using an s-DBT system. Left Below - Reconstruction slice located 1.5 mm below the previous slice. Right - 2D mammography image of	

the same specimen. The high spatial resolution of the s-DBT system allows for imaging of small microcalcifications. The added z-axis information allows for better visualization of MC clusters. The blue oval envelopes a cluster of large MCs and the white oval envelopes a cluster of small MCs.....	114
Figure 41: Left - Reconstructed slice of a specimen using an s-DBT system. The spiculated margins and architectural distortion are more apparent along all edges compared to the 2D mammography image of the same specimen (Right).....	115
Figure 42: Left - Reconstructed slice of a specimen using an s-DBT system. Right - 2D mammography image of the same specimen. Biopsy needles are present in the s-DBT reconstructions and not in the 2D mammography image.....	117
Figure 43: Left - An image of the s-DBT system with a specimen container on the detector housing. Right - An image of a Selenia Dimensions.	123
Figure 44: Reconstruction slice of a breast specimen using the s-DBT system.	125
Figure 45: Plot of the ASF for the s-DBT system (solid line) and the Selenia Dimensions system (dashed line) from MC number 2. A line representing the 50% cutoff is shown.....	129
Figure 46: Left - Simulated MTF curves comparing the effect of pixel size and focal spot size in the s-DBT system. Simulations for both a binned and full resolution detector are shown. Right - The same curves but for the Selenia Dimensions system.	130
Figure 47: Above - Simulated 3D MTF for the s-DBT system with a 0.9 mm isotropic focal spot size using a 70 μm (Left) and 140 μm (Right) detector pixel size. Middle - 3D MTF for the s-DBT system with a 0.6 mm isotropic focal spot size using a 70 μm (Left) and 140 μm (Right) detector pixel size. Below - Simulated 3D MTF for the Selenia Dimensions system using a 70 μm (Left) and 140 μm (Right) detector pixel size.	131
Figure 48: Comparison of MC sharpness for MCs number 7 through 12 between the s-DBT system (Above) and the Selenia Dimension system (Below). Aliasing from the large pixel size and effective focal spot size can be seen in the Selenia Dimensions images. Specimens were not imaged in the same orientation and can therefore have artifacts in different directions.	133
Figure 49: Augmentation mammoplasty model under compression. Two BR3D phantom slabs and the 200cc saline implant were used in the above model.	139

Figure 50: Left - s-DBT reconstructed slice through the lesions of the model with the 400cc saline implant and two BR3D slabs. Right - 2D planar image of the same model. A large amount of tissue overlap can be seen in the 2D planar image.	142
Figure 51: Region I Left - s-DBT reconstruction slice Right - 2D planar image	142
Figure 52: Region II Left - s-DBT reconstruction slice Right - 2D planar image	143
Figure 53: Region III Left - s-DBT reconstruction slice Right - 2D planar image	143
Figure 54: Region IV Left - s-DBT reconstruction slice Right - 2D planar image	144
Figure 55: Bar chart showing the average number of masses counted for the 6 implant configuration for both reader one and two. The error bars represent one standard deviation. Missing bars indicate failure to find any lesions.....	146
Figure 56: Bar chart showing the average number of fibers counted for the 6 implant configuration for both reader one and two. The error bars represent one standard deviation. Missing bars indicate failure to find any lesions.....	147
Figure 57: Bar chart showing the average number of spec clusters counted for the 6 implant configuration for both reader one and two. The error bars represent one standard deviation.	148
Figure 58: Pictorial time lapse of the Selenia Dimensions gantry (Left), after X-ray tube removal (Center), and after CNT source array integration (Right).....	152
Figure 59: Picture of the electronics rack with all components labeled.	153
Figure 60: Picture of the fully assembled s-DBT system in the North Carolina Cancer Hospital at UNC Hospitals.....	154
Figure 61: Diagram of the grounding scheme used in the s-DBT system.	156
Figure 62: Room layout for the s-DBT system in the UNC-CH Cancer Hospital. The numbers represent locations for radiation field surveys.	158
Figure 63: Plots of the x locations (Above), y locations (Middle), and z locations (Below) of the 15 sources used in the clinical trial for patient imaging. Each plot shows the measured beam	

locations indicated by the red stars and the interpolated locations indicated by the blue lines. All distances are in millimeters.....	160
Figure 64: Reconstruction image of the line pair phantom (Left). Looking at the zoomed in region (Right) it can be seen that the s-DBT system using binned detector pixels produces approximately 4 line pairs/mm of resolution, which agrees with previous measurements on the other s-DBT system. ¹³	162
Figure 65: Plot of the average I-V curves for the three configurations used in the clinical trial and the plots for the best and worst cathodes.	163
Figure 66: RCC projection images from beams N15 (Left), 000 (Center), and P15 (Right).	165
Figure 67: RMLO projection images from beams N15 (Left), 000 (Center), and P15 (Right).	165
Figure 68: Reconstruction slices from the first patient from the RCC view (Left) and the RMLO view (Right). Images are in the plane of the large MC cluster on the left portion of the images. The grayscale values of these images are inverted compared to their respective projection images to demonstrate what is typically seen by radiologists.	166

LIST OF ABBREVIATIONS

ACR	American College of Radiology
ASF	Artifact Spread Function
BI-RADS	Breast Imaging-Reporting and Data System
CC	Craniocaudal
CLAHE	Contrast Limited Adaptive Histogram Equalization
CNT	Carbon Nanotube
CT	Computed Tomography
DBT	Digital Breast Tomosynthesis
DMIST	Digital Mammographic Imaging and Screening Trial
DNA	Deoxyribonucleic Acid
ECS	Electronic Control System
EHS	Environmental Health and Safety
FBP	Filtered Back-Projection
FDA	Food and Drug Administration
FFDM	Full Field Digital Mammography
FFT	Fast Fourier Transform
FOV	Field of View
FWHM	Full Width at Half Maximum
GFCI	Ground Fault Circuit Interrupter
GPU	Graphics Processing Unit
iFFT	Inverse Fast Fourier Transform
IRB	Institutional Review Board
I-V	Current-Voltage
MC	Microcalcification
micro-CT	Micro Computed Tomography

ML	Maximum Likelihood
MLO	Medio-Lateral Oblique
Mo	Molybdenum
MOSFET	Metal-Oxide-Semiconductor Field-Effect Transistor
MQSA	Mammography Quality Standards Act
MRT	Microbeam Radiation Therapy
MTF	Modulation Transfer Function
PVDR	Peak-to-Valley Dose Ratio
QF	Quality Factor
RT	Radiation Therapy
SA	Specific Aim
s-DBT	Stationary Digital Breast Tomosynthesis
SdNR	Signal Difference to Noise Ratio
SFM	Screen Film Mammography
SID	Source to Imager Distance
TTL	Transistor-Transistor Logic
UC Davis	The University of California, Davis
UNC-CH	The University of North Carolina at Chapel Hill

CHAPTER 1: INTRODUCTION

1.1 Dissertation Overview

Breast cancer is the most common type of cancer found in women in the United States, with more than 200,000 new cases found each year.¹ When the cancer is diagnosed at an early stage the five-year relative survival rate is between 83.9 and 98.4 percent. This number drops to 23.8 percent when the cancer is diagnosed at a stage at which it has already metastasized.¹ Screening mammography is the current gold standard for early detection of breast cancer.^{2, 3} However, 2D mammography imaging lacks depth information, which can cause underlying and overlying tissue to obstruct the view of lesions. This leads to high false positive and false negative rates.^{4, 5}

Digital breast tomosynthesis (DBT) uses multiple low dose projection images distributed over an angular span to create a pseudo-3D reconstruction of the breast. This added depth information allows for otherwise obscured lesions to become visible.⁶⁻⁹ The Hologic Selenia Dimensions is the only DBT system currently FDA approved for use in the United States.

Current DBT systems use a single x-ray source which is rotated over a limited angle arc. The x-ray source rotates in a continuous motion^{10, 11} or using a step-and-shoot motion.¹² In both methods, the motion of the x-ray source can have an adverse effect on tomosynthesis reconstruction quality and total imaging time.^{13, 14} The source motion results in a blurred focal spot. A blurred focal spot decreases the spatial resolution of the projection images which in turn reduces the spatial resolution of the reconstructed images. High spatial resolution is needed in mammography in order to resolve microcalcifications (MCs). MCs are important because the size and shape of them can indicate the likelihood that a particular lesion is benign or malignant. In both continuous motion and step-and-shoot DBT systems the focal spot blurring effect can be

reduced by decreasing the rotation speed and increasing the acquisition time.^{14, 15} However, a long acquisition time leads to patient motion which also degrades image quality.¹⁶

We have developed a stationary digital breast tomosynthesis system by retrofitting a linearly distributed carbon nanotube (CNT) x-ray source array onto a Hologic Selenia Dimensions DBT system.^{13, 17-20} The system is capable of creating a full set of tomosynthesis projection images with no x-ray source motion and a potential acquisition time of less than 4 seconds when coupled with a high frame rate detector.

Results have shown that the system resolution is increased from less than 3 cycles per mm with the Selenia Dimensions DBT system to more than 4 cycles per mm with the s-DBT system (1.08x magnification, 15 projection images, 15° angular span, 100 mAs). Accelerated lifetime measurements demonstrate an estimated x-ray tube lifetime of over 3 years in clinical service.¹³

The goal of this dissertation is to develop an s-DBT system for use in a clinical trial. Current clinical DBT systems in the United States require a 2D mammogram with all screening DBT exams. This doubles the radiation dose given to the patient. A 2D mammogram is required due to the low spatial resolution of continuous motion DBT systems. An s-DBT system has shown to have better spatial resolution than a continuous motion DBT system. Starting a clinical trial on human patients takes the project a large step closer to showing if its image quality is good enough to remove the requirement for a 2D mammogram thus reducing the radiation dose given to each patient.

The secondary goal of this dissertation is to investigate the usefulness of s-DBT for imaging breast specimens and as a screening tool for patients who have undergone augmentation mammoplasty. Breast specimens are imaged in order to determine if the lesion is inside the surgical margins. Currently 2D mammography is used but depth information is lost in a 2D image. Margins can only be assessed perpendicular to the detector. Using s-DBT to image breast specimens will allow for margins to be assessed perpendicular and parallel to the

detector. This would increase the accuracy of surgical margin assessment. Imaging breast specimens will also present the first human tissue imaged on an s-DBT system. The current practice of doing a four view mammogram on patients with implants increases the radiation dose to the patient, examination time, and patient discomfort. Using implant models it will be determined if it is possible to reduce the four views used currently to screen implant patients to two s-DBT views, one CC view and one MLO view, for each breast or possibly just a single s-DBT MLO view. This would reduce the amount of radiation to the patient, time of exam, and patient discomfort.

1.2 Specific Aims

SA 1: Develop a system for clinical use

In this specific aim (SA) an s-DBT system will be analyzed to determine the optimal imaging configuration. A system will then be built for use in a clinical trial involving human patients. The specific work will include: isolating imaging parameters and determining the effect of each one on image quality, comparing the image quality of various configurations using quantitative measures, constructing an s-DBT system for use in a clinical environment, and characterizing the system.

SA 1.1: Optimal configuration parameters

Image datasets of a crosswire phantom and an American College of Radiography (ACR) accreditation phantom will be collected on an s-DBT system using various configurations. The configurations will have differing parameters such as: number of projection views, angular coverage, entrance dose, mAs distribution, and detector pixel size. The effect of each parameter on image quality factors will be determined. Factors include: signal difference to noise ratio (SdNR), z-axis artifact spread function (ASF), and modulation transfer function (MTF). The optimal imaging configuration based on quantitative analysis of these three factors will yield the optimal imaging configuration.

SA 1.2: System characterization and clinical implementation

An s-DBT system will be built for use in a clinical environment. After construction of the system, many system values will be characterized and optimized for use on patients. These values include: system geometry, radiation exposure rate based on kVp, X-ray field of view, spatial resolution, I-V curves, and transmission rates. The values will be implemented into the operating software and a radiologist technician will be trained to use the system.

SA 2: Demonstrate the usefulness of s-DBT

In this SA the usefulness of an s-DBT system for imaging breast specimens and for screening patients with augmentation mammoplasty will be determined. The specific work will include: collecting breast specimen images using s-DBT, determining the effectiveness of s-DBT as an imaging tool for breast specimens, demonstrating the increased spatial resolution of s-DBT, collecting phantom implant images with an s-DBT system and a 2D mammography system, and using the collected images to determine if s-DBT is a feasible alternative to 2D mammography for screening patients with augmentation mammoplasty.

SA 2.1: Breast specimen study

A protocol will be submitted to the UNC-CH Institutional Review Board. Upon acceptance, patients scheduled for lumpectomy procedures at UNC hospitals will be recruited for use in the study. Images of the excised specimen are first taken on a 2D mammography system in the hospital by trained radiologist technicians. The specimen will then be transferred to our facility to be imaged using an s-DBT system and a clinical DBT system. The configuration determined in SA 1.1 will be used for the imaging on the s-DBT system. Once imaging is completed, the specimen will then be transferred to the pathology department in the hospital for malignancy analysis.

After collection of a sufficient number of specimen images for statistical analysis, four trained readers will review the 2D mammography datasets and the s-DBT datasets. Readers will give malignancy scores for the datasets, confidence levels based on the s-DBT dataset, and assess the surgical margins. Statistical analysis will be completed by a trained biostatistician. Based on the results of the reader study, the efficacy of s-DBT as a tool for imaging breast specimens will be determined.

A secondary study will be conducted using the data collected on the clinical DBT system. The increased microcalcification visibility in s-DBT will be analyzed using human tissue. Measurements will be made for the x, y, and z axis resolutions of both the clinical DBT system and the s-DBT system. Finally, a spatial resolution simulation will be used to show further proof of increased spatial resolution in s-DBT. Based on the results of the study, the extent of s-DBT image quality improvement will be determined.

SA 2.2: Feasibility of s-DBT as an implant screening tool

Augmentation mammoplasty models will be created using a combination of a breast tissue phantom with lesions and various sized saline and gel silicone implants. Each model will be imaged on an s-DBT system and a 2D mammography system using the same entrance dose. After collection of the data, the reconstructed images will be shown to trained radiologists. The radiologists will report the number of visual lesions for each dataset. The results will show if s-DBT is more effective than 2D mammography for an implant in the field of view image. Depending on the effectiveness it will be determined if s-DBT is a feasible tool for screening patients with augmentation mammoplasty.

1.3 Dissertation Organization

This dissertation is separated into three major sections: (1) background information, (2) scholarly research completed, (3) clinical trial preparation. Chapters 2 through 6 give background information for the research completed. Chapter 2 gives background information

related to X-ray production and interactions in matter. Chapter 3 gives an overview of mammography fundamentals including, image quality and terminology. Chapter 4 covers mammographic imaging modalities used in the clinic and preclinical systems. Chapter 5 and 6 cover carbon nanotube based X-ray sources and their applications. The completed scholarly research is in chapters 7 through 10. These chapters are written as scholarly journal articles with some of the background information removed. The needed background information can be found in chapters 2 through 6. Chapter 11 overviews the construction of a new s-DBT system for use in a clinical trial. Finally chapter 12 gives a summary of all the research conducted.

REFERENCES

- 1 N. Howlader, A. Noone, M. Krapcho, N. Neyman, R. Aminou, W. Waldron, S. Altekruse, C. Kosary, J. Ruhl, Z. Tatalovich, "SEER Cancer Statistics Review, 1975-2008, National Cancer Institute. Bethesda, MD," SEER website(2011).
- 2 L. Nystrom, I. Andersson, N. Bjurstam, J. Frisell, B. Nordenskjold, L.E. Rutqvist, "Long-term effects of mammography screening: updated overview of the Swedish randomised trials," *Lancet* **359**, 909-918 (2002).
- 3 S.M. Moss, H. Cuckle, A. Evans, L. Johns, M. Waller, L. Bobrow, "Effect of mammographic screening from age 40 years on breast cancer mortality at 10 years' follow-up: a randomised controlled trial," *Lancet* **368**, 2053-2060 (2006).
- 4 J.G. Elmore, M.B. Barton, V.M. Moceris, S. Polk, P.J. Arena, S.W. Fletcher, "Ten-year risk of false positive screening mammograms and clinical breast examinations," *New England Journal of Medicine* **338**, 1089-1096 (1998).
- 5 T. Wu, R.H. Moore, E.A. Rafferty, D.B. Kopans, "A comparison of reconstruction algorithms for breast tomosynthesis," *Med Phys* **31**, 2636 (2004).
- 6 I. Andersson, D.M. Ikeda, S. Zackrisson, M. Ruschin, T. Svahn, P. Timberg, A. Tingberg, "Breast tomosynthesis and digital mammography: a comparison of breast cancer visibility and BIRADS classification in a population of cancers with subtle mammographic findings," *European radiology* **18**, 2817-2825 (2008).
- 7 J.T. Dobbins III, D.J. Godfrey, "Digital x-ray tomosynthesis: current state of the art and clinical potential," *Physics in medicine and biology* **48**, R65 (2003).
- 8 S.P. Poplack, T.D. Tosteson, C.A. Kogel, H.M. Nagy, "Digital breast tomosynthesis: initial experience in 98 women with abnormal digital screening mammography," *AJR. American journal of roentgenology* **189**, 616-623 (2007).
- 9 A.P. Smith, L. Niklason, B. Ren, T. Wu, C. Ruth, Z. Jing, "Lesion visibility in low dose tomosynthesis," in *Digital Mammography* (Springer, 2006), pp. 160-166.
- 10 M. Bissonnette, M. Hansroul, E. Masson, S. Savard, S. Cadieux, P. Warmoes, D. Gravel, J. Agopyan, B. Polischuk, W. Haerer, "Digital breast tomosynthesis using an amorphous selenium flat panel detector," *Proc. SPIE* **5745**, (2005).
- 11 B. Ren, C. Ruth, T. Wu, Y. Zhang, A. Smith, L. Niklason, C. Williams, E. Ingall, B. Polischuk, Z. Jing, "A new generation FFDM/tomosynthesis fusion system with selenium detector," *Proc. SPIE* **7622**, (2010).
- 12 X. Gong, S.J. Glick, B. Liu, A.A. Vedula, S. Thacker, "A computer simulation study comparing lesion detection accuracy with digital mammography, breast tomosynthesis, and cone-beam CT breast imaging," *Med Phys* **33**, 1041-1052 (2006).
- 13 X. Qian, A. Tucker, E. Gidcumb, J. Shan, G. Yang, X. Calderon-Colon, S. Sultana, J. Lu, O. Zhou, D. Spronk, F. Sprenger, Y. Zhang, D. Kennedy, T. Farbizio, Z. Jing, "High

- resolution stationary digital breast tomosynthesis using distributed carbon nanotube x-ray source array," *Med Phys* **39**, 2090 (2012).
- 14 E. Shaheen, N. Marshall, H. Bosmans, "Investigation of the effect of tube motion in breast tomosynthesis: continuous or step and shoot?," *Proc. SPIE* **7961**, (2011).
 - 15 J. Zhou, B. Zhao, W. Zhao, "A computer simulation platform for the optimization of a breast tomosynthesis system," *Med Phys* **34**, 1098-1109 (2007).
 - 16 R.J. Acciavatti, A.D. Maidment, "Optimization of continuous tube motion and step-and-shoot motion in digital breast tomosynthesis systems with patient motion," *Proc. SPIE* **8313**, (2012).
 - 17 X. Qian, R. Rajaram, X. Calderon-Colon, G. Yang, T. Phan, D.S. Lalush, J. Lu, O. Zhou, "Design and characterization of a spatially distributed multibeam field emission x-ray source for stationary digital breast tomosynthesis," *Med Phys* **36**, 4389-4399 (2009).
 - 18 G. Yang, R. Rajaram, G. Cao, S. Sultana, Z. Liu, D. Lalush, J. Lu, O. Zhou, "Stationary digital breast tomosynthesis system with a multi-beam field emission x-ray source array," *Proc. SPIE* **6913**, (2008).
 - 19 O.Z. Zhou, G. Yang, J. Lu, D. Lalush, "Stationary x-ray digital breast tomosynthesis systems and related methods," US Patent No. US7751528 B2 (Jul 6, 2010 2010).
 - 20 F. Sprenger, X. Calderon-Colon, E. Gidcumb, J. Lu, X. Qian, D. Spronk, A. Tucker, G. Yang, O. Zhou, "Stationary digital breast tomosynthesis with distributed field emission x-ray tube," *Proc. SPIE* **7961**, (2011).

CHAPTER 2: X-RAY PRODUCTION AND INTERACTIONS IN MATTER

2.1 Overview

Since the discovery of X-rays in 1895 by Wilhelm Conrad Röntgen, they have become an integral part of the medical field. X-rays are produced when high energy electrons are bombarded onto a high Z material. Once they strike the material, the electrons impart their energy into the high Z target mostly as heat. A very small portion of the energy is transformed into either Bremsstrahlung or characteristic X-rays. Careful consideration must be used when designing a X-ray tube. The size of the cathode and the tilt of the anode will significantly impact the spatial resolution of the X-ray system. Design of the filtration and collimation of an X-ray tube will ensure that the appropriate dose is given to a patient. Once the X-rays interact with the object that is being imaged through the processes of photoelectric absorption, Rayleigh scatter, and Compton scatter an image can be created with differing levels of contrast based on the attenuation of the materials being imaged.

2.2 Discovery of X-rays

Crookes tubes are partially evacuated glass tubes which contain an anode and cathode electrode.²¹ When a high voltage is applied between the two electrodes, a Townsend discharge occurs creating positive ions which are then attracted to the negative voltage of the cathode. The movement of the electrons are called cathode rays. Once they strike the cathode, electrons are released and accelerated toward the anode. The electrons strike the glass tube and fluorescence occurs. On November 8th 1895, Wilhelm Conrad Röntgen, a German physicist, was working with a Crookes tube. He had covered the tube in black cardboard and was using a fluorescent screen to investigate cathode rays. Röntgen noticed that although the tube was covered and no visible light could escape, the fluorescent screen still had a faint glow. He

realized that some invisible ray was traversing through the cardboard and striking the screen. Through a series of experiments he found that these rays could traverse through a variety of items. He called them X-rays, the "X" standing for a mathematical variable that is unknown.²² Röntgen famously imaged his wife's hand using X-rays. This image is the very first use of medical imaging. Röntgen received the first Nobel Prize in Physics for his discovery of X-rays in 1901.

2.3 X-ray Production

X-rays are produced when the kinetic energy of electrons is converted into electromagnetic radiation. X-rays are typically created in a X-ray tube, which, unlike the Crookes tube used by Röntgen, produces electrons by a process called thermionic emission. Thermionic emission is the process of adding enough heat energy to electrons in a metal to overcome the work function of the metal. Once this occurs the electrons are emitted from the metal. In a typical X-ray source, a metal filament is heated (typically thoriated tungsten) in a evacuated chamber. A high voltage is applied between the metal filament and a metal surface in the tube. The filament is at a negative voltage (cathode electrode) while the surface is at a positive voltage (anode electrode). Once the voltage is applied between the cathode and anode, the emitted electrons will accelerate toward the anode with a kinetic energy (keV) proportional to the potential difference (kVp) between the cathode and anode. When the electrons strike the surface of the anode, their energy is converted into other forms. Approximately 99.5% of all energy is converted into heat through small electron collision exchanges.²² The other energy is converted into two types of X-rays: Bremsstrahlung and Characteristic.

2.3.1 Bremsstrahlung X-rays

Bremsstrahlung radiation occurs when an electron passes near the nucleus (positively charged) of an atom. Coulombic forces cause the electron to lose kinetic energy and change direction. The lost energy becomes a X-ray photon produced by Bremsstrahlung radiation.

More energy is lost as the electron's path is closer to the nucleus resulting in higher energy photon production. **Figure 1** is a diagram showing several electron interactions and the difference in photon energy due to distance differences. Since the size of an atom's nucleus is relatively small compared to the total area the electron shells take up, the probability of producing high energy photons is small compared to producing low energy photons. The total photon output, or spectrum, from Bremsstrahlung radiation increases linearly with decreased photon energy. However, the low energies of X-ray production are absorbed by the materials in the path of the X-ray in a process called filtration. More information on filtration can be found in **Section 2.4.3**.

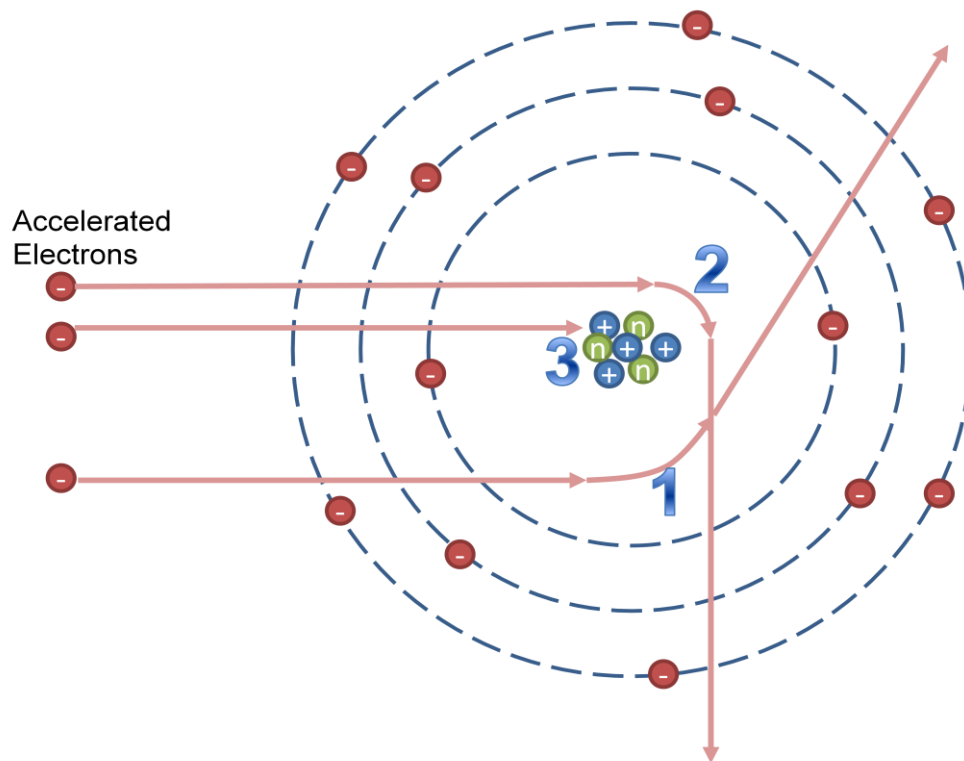


Figure 1: Diagram of three different electron interactions in an atom where Bremsstrahlung radiation would be produced. The numbers indicate locations of X-ray production in order of increasing energy lost. The farther the electron is from the nucleus the less energy is converted to X-rays. This image is for demonstrative purposes and does not represent actual interactions or atoms. Image is modeled after a figure from Bushberg et al.²²

2.3.2 Characteristic X-rays

Some electrons bombarding the anode will collide with an electron in the shell of an atom. If the energy transferred to the shell electron is higher than the binding energy of the electron then the electron could be ejected from the shell. The difference in the transferred energy and the binding energy is the amount of kinetic energy the now free electron will have. The atom has now become an ion. The resultant unstable electron shell will be filled with an outer shell electron at a lower binding energy. When the electron transitions shells, the difference in energy between the two shells can be expelled as a characteristic photon. Since the energy of the expelled photon depends on the different shell energies then every material produces a unique set of characteristic photons, hence the name characteristic. Each characteristic X-ray is given a name. The name corresponds to the letter of the vacant shell being filled. A subscript is also added which designates if the electron filling the shell is from an adjacent (α) or a non-adjacent shell (β). For example: an electron coming from the L shell to the K shell would be named K_{α} . The low energies of non-K shell characteristic X-rays are filtered by the tube housing in medical imaging applications. Together, the characteristic and Bremsstrahlung X-rays make the spectrum of a particular X-ray source. **Figure 2** shows a simulated spectrum of a X-ray source with a tungsten target and a 1 mm thick tungsten filter.

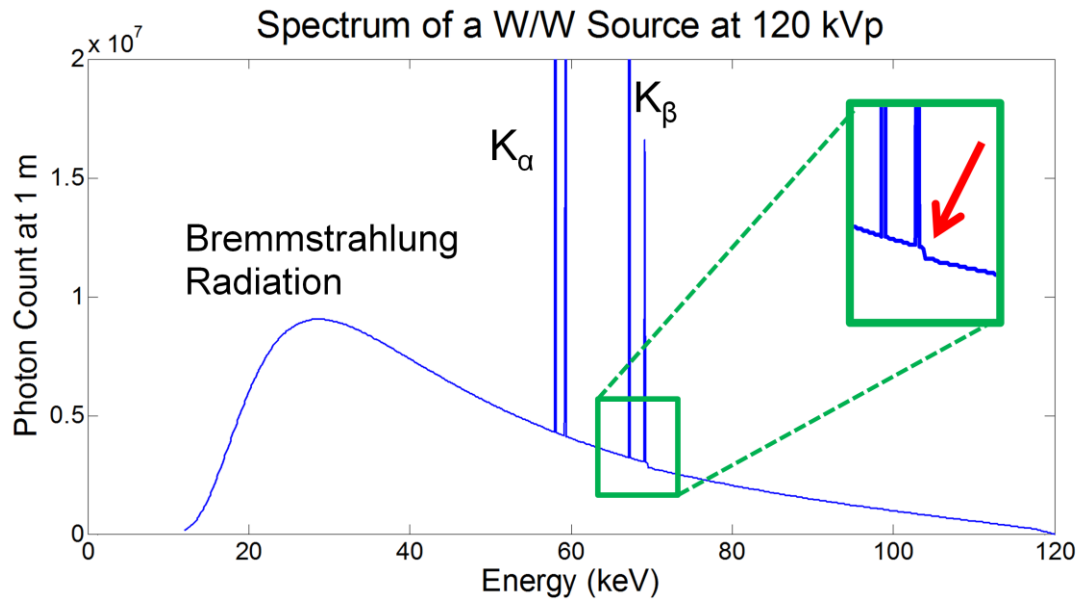


Figure 2: Simulation of an energy spectrum from an X-ray source with a tungsten target and 1 mm of tungsten filtration. The applied potential difference was 120 kVp. Both the characteristic K_{α} and K_{β} X-ray peaks are labeled as well as the Bremsstrahlung curve. The zoomed in region shows the k edge which is the energy at which the attenuation coefficient of tungsten increases due to the photoelectric absorption of electrons.

2.4 X-ray Tube Design

X-ray tube design has not changed significantly William David Coolidge designed and patented the very first modern X-ray tube in 1913.²³ These tubes, as stated in **Section 2.3**, utilize thermionic emission to extract electrons from the cathode. The major components of the modern X-ray tube are: the cathode, the anode, and the tube housing. **Figure 3** shows a diagram of an X-ray tube with all major components labeled.

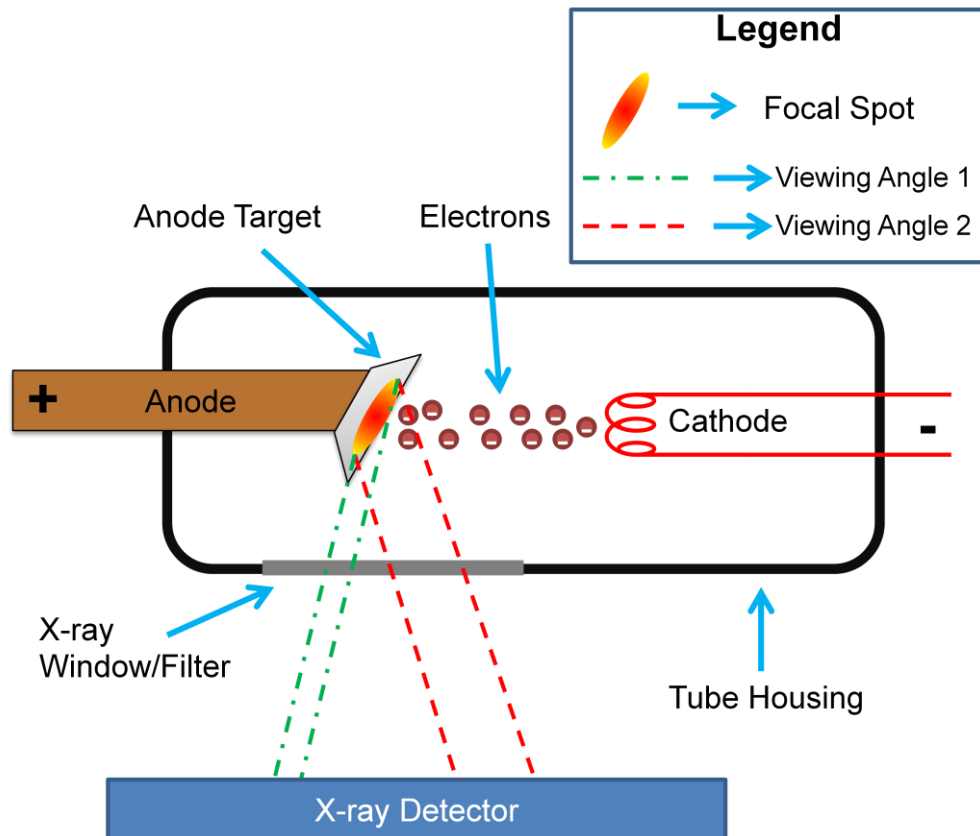


Figure 3: Diagram of a modern X-ray tube. The major components of an X-ray tube are the cathode, the anode, and the tube housing. The combination of the anode target angle and the anode viewing angle can change the effective focal spot on the detector, thus changing the resolution of the image.

2.4.1 The Cathode

The cathode is the source of the electrons in an X-ray tube. A cathode consists of a high melting point metal (typically thoriated tungsten). The metal is shaped into a long thin helical spiral called a filament. The filament is attached to an electric circuit and a small voltage (around 10 V) is applied, producing a current up to 7 A.²² Resistance in the filament creates a large amount of heat (>1000 K) in a short amount of time. The heat added to the filament increases the kinetic energy of the electrons in the metal. Once the kinetic energy of the electrons is greater than the work function of the metal, then through a process called thermionic emission the electrons are emitted into the surrounding vacuum. If a potential difference exists between the anode and the cathode then the electrons will accelerate toward the anode. The current hitting the anode (tube current) is directly related to the amount of

electrons emitting from the cathode. If 1 mA of current is hitting the anode then 6.24×10^{15} electrons per second are hitting the anode. Tube currents for radiology X-ray tubes range from 100 to 1,000 mA with an exposure time as high as 100 ms. In order to change the tube current, the filament current is modulated. For most diagnostic X-ray energies the higher the filament current the higher the tube current. However, for lower tube potentials (potential difference between the anode and cathode) the tube becomes space charge limited. This most often is a problem for mammographic imaging modalities which can have tube potentials as low as 20 kVp. Once the tube potential is sufficiently high (> 40 kVp) the space charge is overcome by the tube potential.

The location that the electron beam hits the anode is called the focal spot. Focal spot size is very important in radiographic imaging due to its direct relationship with image spatial resolution. As the focal spot becomes larger the spatial resolution becomes worse. The effective focal spot is the perceived focal spot on the detector and is what determines the spatial resolution. Although a tube could have a poor focal spot, the effective focal spot could be substantially smaller. The effective focal spot is covered in **Section 2.4.4**. The actual focal spot is directly related to the size of the cathode filament. Since filaments are long and thin, there is a substantial difference in the focal spot size in one direction compared to the other. To compensate for the large focal spot size, the viewing angle of the X-ray detector is changed. The effect of the viewing angle can be seen in **Figure 3**. In the figure, the red dashed line shows a large viewing angle which increases the size of the effective focal spot. The green dashed line shows a small viewing angle which decreases the size of the effective focal spot. The thin direction of the cathode filament produces a much smaller focal spot, however in radiographic imaging even smaller focal spots are needed. Most cathode filaments are surrounded by a focusing cup which is set to a biased voltage. The voltage can range between the voltage of the filament to a more negative voltage (around 100 V less).²² As the focusing

cup voltage becomes more negative, the electrons are repelled from the cup and a thinner focal spot is created.

2.4.2 The Anode

The anode is the source of the X-ray radiation in an X-ray tube. The most common anode material is tungsten due to its high melting point (3695 K) and high atomic number (74). Higher atomic numbers yield a higher X-ray production efficiency. The high melting point is needed because of the approximately 99% inefficiency of X-ray production at radiographic energies. The 99% of energy bombarding the anode that is not converted to X-ray radiation is converted into heat energy. The added heat energy can raise the surface temperature of the anode to several thousand Kelvin within a few milliseconds. For this reason heat dissipation is a very important variable that must be accounted for in X-ray tube production. Typically, an alloy of 10% rhenium and 90% tungsten is used as an anode surface material to further prevent surface damage. Some mammography systems utilize molybdenum or rhodium due to their low energy characteristic peaks. High powered X-ray tubes require the use of rotating anodes to dissipate heat during X-ray exposures. A rotating anode consists of the anode disk, the stem, and the rotor. The anode disk contains a circular track where electrons bombard. The disk is constantly spinning during X-ray exposures to ensure that the surface temperature stays below the melting point of the target. The stem is constructed of a poor heat conductor (typically molybdenum). The stem's purpose is to prevent excessive heat from the anode disk from reaching the heat sensitive components of the rotor. The rotor is a ball-bearing system that uses electromagnetic induction in order to spin the anode disk between 3,000 and 9,000 RPM. The rotating anode adds a large amount of expense and complexity to an X-ray tube. For X-ray tubes not requiring a high power rating, a stationary anode is used with a highly conducting backing which dissipates residual heat between exposures.

A small amount of anode heat dissipation occurs because of the angle of the anode. Anode angles help reduce the size of the effective focal spot in the length direction of the cathode filament. The anode angle is the angle at which the anode is placed perpendicular to the electron beam. Different anode angles are used for different applications. Small anode angles produce small effective focal spots but result in an increase in the heel effect. The heel effect is when emitted X-rays travel through the anode on their path to the X-ray detector. The X-rays are attenuated by the anode and thus reduce the X-ray flux on the detector. Therefore, removing the area of X-ray radiation affected by the heel effect is important. When a small anode angle is used the useful area of the beam is reduced and therefore results in a smaller X-ray field of view (FOV) on the detector. **Figure 4** demonstrates the effect of the anode angle on the X-ray FOV.

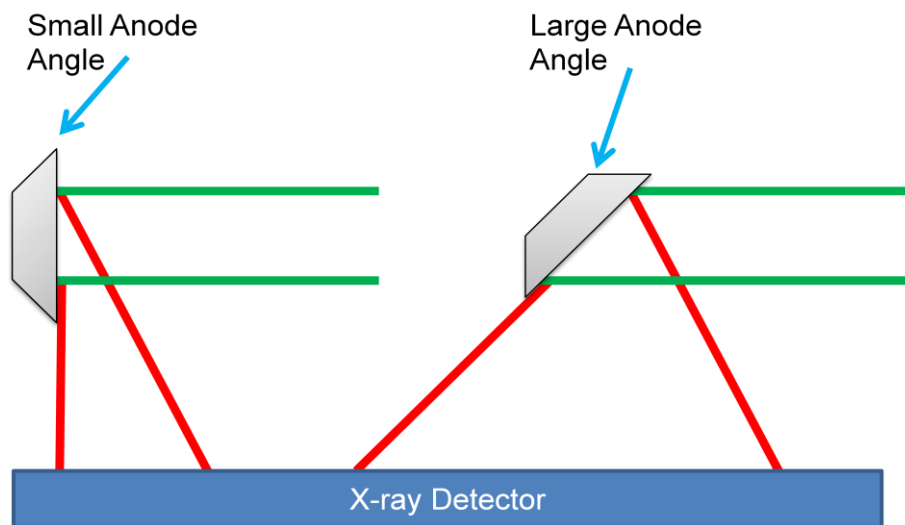


Figure 4: Diagram depicting the effect of anode angle on X-ray FOV. In the diagram, the green lines represent electron beams and the red lines represent X-ray beams. The small anode angle on the left results in a small FOV on the detector while the large anode angle on the right results in a large FOV on the detector. Anode angles are exaggerated for demonstrative purposes.

2.4.3 Tube Housing

In a radiographic X-ray tube, the tube housing is composed of the vacuum housing, X-ray window, filter, and collimator. The vacuum housing is important because it separates the vacuum inside the tube from the environment. It also provides support and a primary source of

X-ray shielding. Since X-rays are produced in every direction when the tube is on, it is very important to shield patients and operators from unwanted radiation. Very dense materials are used around the vacuum housing to absorb unwanted radiation. The Food and Drug Administration (FDA) limits the amount of radiation that penetrates this shielding to 100 mR/hr at a distance of 1 m from the focal spot.²²

The window/filter combination of a X-ray tube determines the beam quality. Beam quality refers to the distribution of X-ray energies in a X-ray beam. A hardened X-ray beam consists of higher energy X-rays. Depending on the application, a variety of beam qualities could be wanted in a radiography system. For most systems, the X-ray window consists of glass or aluminum. Both materials will attenuate the majority of X-rays that are at 15 keV or below.²² In mammography systems, low energy X-rays are essential due to the soft tissue being imaged. Mammography systems typically use beryllium windows which have a much lower atomic number than aluminum and therefore attenuate less low energy X-rays. Further filtration beyond the window is useful in some systems to form the beam quality to a particular purpose. Some mammography systems use rhodium and silver filters.²⁴ Some imaging examinations utilize contrast agents to increase the contrast of suspicious lesions.²⁵ During these examinations two different energies can be used to image the patient. Both a low energy and high energy X-ray exposure is used. The purpose is to have an image with an average energy above and below the K-edge of the contrast agent. Once the images are taken, normalizing and subtracting the images yields an image of only the areas where the contrast agent has pooled. In order to change the average energy of the beam without adding a large amount of radiation dose to the patient a filter is used. Selecting a filter with a K-edge similar to the contrast agent being used can allow for a large low energy dose while filtering out the unwanted high energy. A K-edge is an energy above the binding energy of K shell electrons which has a sudden increase in the attenuation coefficient due to photoelectric absorption of electrons.²⁶ **Figure 2** shows an X-ray spectrum with a K-edge effect highlighted.

The X-ray collimator limits the FOV of the X-ray beam to the X-ray detector. FDA regulations limit the amount of radiation that can pass outside the FOV of the detector. A collimator consists of four sides of highly attenuating metal. The four sides can be adjusted in order to limit the beam to the appropriate area on the detector. More advanced collimators are used in radiation therapy systems to change the trajectory of the X-ray beams to limit the radiation exposure to normal tissue.

2.4.4 Effective Focal Spot

The effective focal spot of an imaging system is directly related to the spatial resolution of images. A smaller effective focal spot results in higher resolution images. The factors effecting the effective focal spot are: the actual focal spot size, the anode angle, and the viewing angle. The focal spot size and viewing angle were covered in **Section 2.4.1** while the anode angle was covered in **Section 2.4.2**. All of these factors convolved together will give the effective focal spot.

2.5 X-ray Interactions in Matter

In order for a X-ray based imaging system to produce usable images, some amount of X-ray radiation must be absorbed by the item being imaged. Variations in the absorption of different materials give contrast to X-ray images. Other forms of X-ray interaction with matter include scattering and pair production. The four major forms of X-ray photon interactions and matter are: (1) photoelectric absorption, (2) Rayleigh scatter, (3) Compton scatter, and (4) pair production.

2.5.1 Photoelectric Absorption

Photoelectric absorption is the major source of contrast in a radiographic image. The process of photoelectric absorption occurs when an incident X-ray photon contains more energy than the work function of an electron in the shell of an atom. All the energy of the photon is transferred to the electron which is subsequently ejected from the atom with a kinetic energy

equal to the energy of the incident photon minus the binding energy of the electron. If the ejected electron was occupying an inner shell, then the vacancy in the shell will be filled by an outer shell electron. The difference in binding energies of the two electron shells will be released as either a characteristic X-ray or as an Auger electron. An Auger electron occurs when the binding energy difference is transferred to an outer shell electron. If the energy is higher than the binding energy of the electron then it will also be ejected with a kinetic energy equal to the impending energy (from the first binding energy difference) minus the binding energy of the Auger electron. After production of the Auger electron or characteristic X-ray, there is now another open position in an electron shell and the process could happen again. This will continue in a cascade from the inner shell to the outer shell. The probability of photoelectric absorption occurring is approximately proportional to the following equation:

Equation 1:

$$P_{pa} \propto \frac{Z^3}{E^3}$$

Where " P_{pa} " is the probability of photoelectric absorption per unit mass, " Z " is the atomic number of the absorbing material, and " E " is the energy of the incident photon. Analyzing this equation shows that higher atomic number elements will have a higher probability of photoelectric absorption for a particular photon energy. This equation also shows why the field of mammography utilizes low energy photons for imaging. The effective atomic number of different breast tissues is between 5 and 6.²⁷ which would require a very low photon energy to keep the probability of absorption high.

2.5.2 Rayleigh Scatter

Scattering in medical imaging produces unwanted image deterioration. It also requires an increase in X-ray dose to compensate for loss of image contrast. There are two types of X-ray scatter: Rayleigh and Compton. In Rayleigh scatter, the incident photon excites the entire atom by imparting energy into the electron cloud causing the electrons to oscillate in phase. As

they begin to oscillate another photon of equal energy but in a different direction is ejected from the atom. This particular type of scattering has a very low probability of occurring at most diagnostic energy levels. It accounts for less than 5% of all X-ray interactions above 70 keV.²² However, Rayleigh scatter becomes more of a problem for mammographic energies. At 30 keV the probability increases to 12%.²²

2.5.3 Compton Scatter

Unlike Rayleigh scatter, Compton scatter is the dominant form of X-ray interaction in matter for the majority of diagnostic X-ray energies. Above approximately 300 keV, Compton scatter is the only attenuation interaction that occurs for soft tissue until pair production begins at around 3,000 keV. For energies above approximately 30 keV, Compton scatter is more prevalent than photoelectric absorption for soft tissue. In Compton scatter, the incident photon imparts enough energy to overcome the work function of the atom and ejects the electron with some kinetic energy. The incident photon has not lost all its energy, so it continues on in a separate trajectory. This type of interaction most often occurs for outer shell electrons. Total energy is conserved so the energy of the incident photon is equal to the energy of scattered photon plus the energy of the ejected electron plus the binding energy of the electron. The energy of the scattered photon can be calculated from the following equation:

Equation 2:

$$E_f = \frac{E_i}{1 + \frac{E_i}{511 \text{ keV}} (1 - \cos \theta)}$$

Where " E_f " is the final energy of the photon, " E_i " is the initial energy of the photon, and " θ " is the angle of the scattered photon with respect to incident trajectory. From the equation it can be seen that higher energy photons will be scattered at a lower angle. These photons can continue on to the X-ray detector but will add scatter to the image which decreases image contrast.

Scatter on a radiographic image can be significant with respect to the total contrast to the image. The scatter to primary ratio is the amount of detected photons from scattered interactions to the amount of unscattered photons. In radiography, scatter to primary ratios can range from 0.4 to 20.^{28, 29} There has been a lot of research conducted into reducing or estimating the scatter in radiographic images. Many systems implement an anti-scatter grid to remove unwanted scattered photons.³⁰ Anti-scatter grids are then sheets of highly attenuating metals which have a series of holes or lines which correspond to detector pixels and are aligned with the location of the X-ray source. Since the holes are aligned they will theoretically only allow photons which are on a direct path from the X-ray source. However, they do not remove all scatter due to secondary scatter and misalignment. They also reduce the amount of primary X-rays that are reaching the detector. In order to compensate for the loss in primary X-rays, longer exposures are required.

2.5.4 Pair Production

Pair production does not occur in the diagnostic energy range. X-ray energies higher than 1.02 MeV are required in order for pair production to take place.²² An electron-positron pair is produced when high energy X-rays interact with electric field of an atom's nucleus. The energies of the matter and antimatter pair are both 0.511 MeV, which is the rest mass energy of an electron. The positron will lose energy through excitation and ionization until it comes to rest. Once it comes to rest it will interact with an electron and produce an annihilation event will occur producing two photons which travel in opposite directions.

2.5.5 Attenuation Coefficient

The total attenuation of a photon is a combination of the four aforementioned photon-matter interactions. The total attenuation depends on the incident photon energy and the material composition. For a particular material and energy, the attenuation of photons per unit

thickness is called the linear attenuation coefficient " μ ". The Beer-Lambert law shows the correlation between the linear attenuation coefficient and the number of transmitted photons:

Equation 3:

$$I = I_0 e^{-\mu x}$$

Where " I " is the number of photons exiting the material, " I_0 " is the number of photons incident on the material, " μ " is the linear attenuation coefficient of the material, and " x " is the distance traveled through the material. The linear attenuation coefficient decreases with increased X-ray energies for a given material unless a K-edge is present. **Table 1** shows various materials and the relationship between electron density and attenuation coefficient at 50 keV. Materials with higher electron densities give higher probabilities that an incident electron will interact with the atom. Thus the likelihood of attenuation and the attenuation coefficient increases.

Table 1: Linear attenuation coefficient for various materials at an energy of 50 keV. As the electron density increases the probability of photon interaction increases thus the linear attenuation coefficient increases. Table is recreated from data from Bushberg et al.²²

Material	Density (g/cm ³)	Electrons per Mass (e/g) x 10 ²³	Electron Density (e/cm ³)	μ (cm ⁻¹)
Hydrogen	0.000084	5.97	0.0005	0.000028
Water vapor	0.000598	3.34	0.002	0.000128
Air	0.00129	3.006	0.0038	0.000290
Fat	0.91	3.34	3.04	0.193
Ice	0.917	3.34	3.06	0.196
Water	1	3.34	3.34	0.214
Compact bone	1.85	3.192	5.91	0.573

REFERENCES

- 1 W. Crookes, "On the Illumination of Lines of Molecular Pressure, and the Trajectory of Molecules," *Proceedings of the Royal Society of London* **28**, 102-111 (1878).
- 2 J.T. Bushberg, J.M. Boone, *The essential physics of medical imaging*. (Lippincott Williams & Wilkins, 2011).
- 3 W.D. Coolidge, "X-ray tube," US Patent No. 1,355,126 (1920).
- 4 S.S.J. Feng, I. Sechopoulos, "Clinical Digital Breast Tomosynthesis System: Dosimetric Characterization," *Radiology* **263**, 35-42 (2012).
- 5 B. Ren, C. Ruth, Y. Zhang, A. Smith, D. Kennedy, B. O'Keefe, I. Shaw, C. Williams, Z. Ye, E. Ingall, "Dual energy iodine contrast imaging with mammography and tomosynthesis," *SPIE Medical Imaging*, (2013).
- 6 E. Roessl, R. Proksa, "K-edge imaging in x-ray computed tomography using multi-bin photon counting detectors," *Physics in medicine and biology* **52**, 4679 (2007).
- 7 M. Antoniassi, A. Conceição, M. Poletti, "Study of effective atomic number of breast tissues determined using the elastic to inelastic scattering ratio," *Nuclear Instruments and Methods in Physics Research Section A: Accelerators, Spectrometers, Detectors and Associated Equipment* **652**, 739-743 (2011).
- 8 G.T. Barnes, "Contrast and scatter in x-ray imaging," *Radiographics* **11**, 307-323 (1991).
- 9 Z. Jing, W. Huda, J.K. Walker, "Scattered radiation in scanning slot mammography," *Med Phys* **25**, 1111 (1998).
- 10 J.M. Boone, J.A. Seibert, C.-M. Tang, S.M. Lane, "Grid and Slot Scan Scatter Reduction in Mammography: Comparison by Using Monte Carlo Techniques¹," *Radiology* **222**, 519-527 (2002).

CHAPTER 3: MAMMOGRAPHIC IMAGING FUNDAMENTALS

3.1 Overview

In order to completely understand the research and work done in this dissertation, background information is needed on mammographic imaging. The following sections will cover anatomy of the breast and associated lesions of the breast, including masses and microcalcifications (MCs). Following the anatomy section, there will be an overview of image quality and assessment.

3.2 The Human Breast

The human breast is a complex component of the human body. It is also the source of the second leading cause of cancer in women in the United States affecting more than 200,000 women each year.¹ The following section contains information about the structure of the human breast and associated lesions. Although men are also susceptible to breast cancer, this section will only cover the female breast.

3.2.1 Female Breast Anatomy and Positioning

The human breast is a skin gland which develops from the mammary ridge. It lies between the clavicle bone and the eighth rib on the chest wall. The breast lies on the pectoralis major muscle but frequently wraps around the lateral side of the muscle.

There are 6 major components to a female breast; (1) the nipple, (2) the areola, (3) the ducts, (4) the lobules, (5) fat and connective tissue, and (6) skin. The lobules are the glands of the breast which secrete milk. They are the starting point of the duct system in breast anatomy but are referred to as the terminal portion. Each lobule secretes milk to a terminal duct. Clusters of lobules and their associated terminal duct are called the terminal duct lobular unit. The ducts traverse the breast and reach the nipple where milk is secreted out of the body. The

structure surrounding the nipple is the areola. The breast is held together by varying sized sheets of connective tissue. Subcutaneous fat surrounds and is interdispersed within the connective tissue. Skin envelopes the entirety of the breast except the areola and nipple area.³¹

Figure 5 shows a schematic of a typical female breast. In the image the major components and the surrounding components of the breast are labeled.

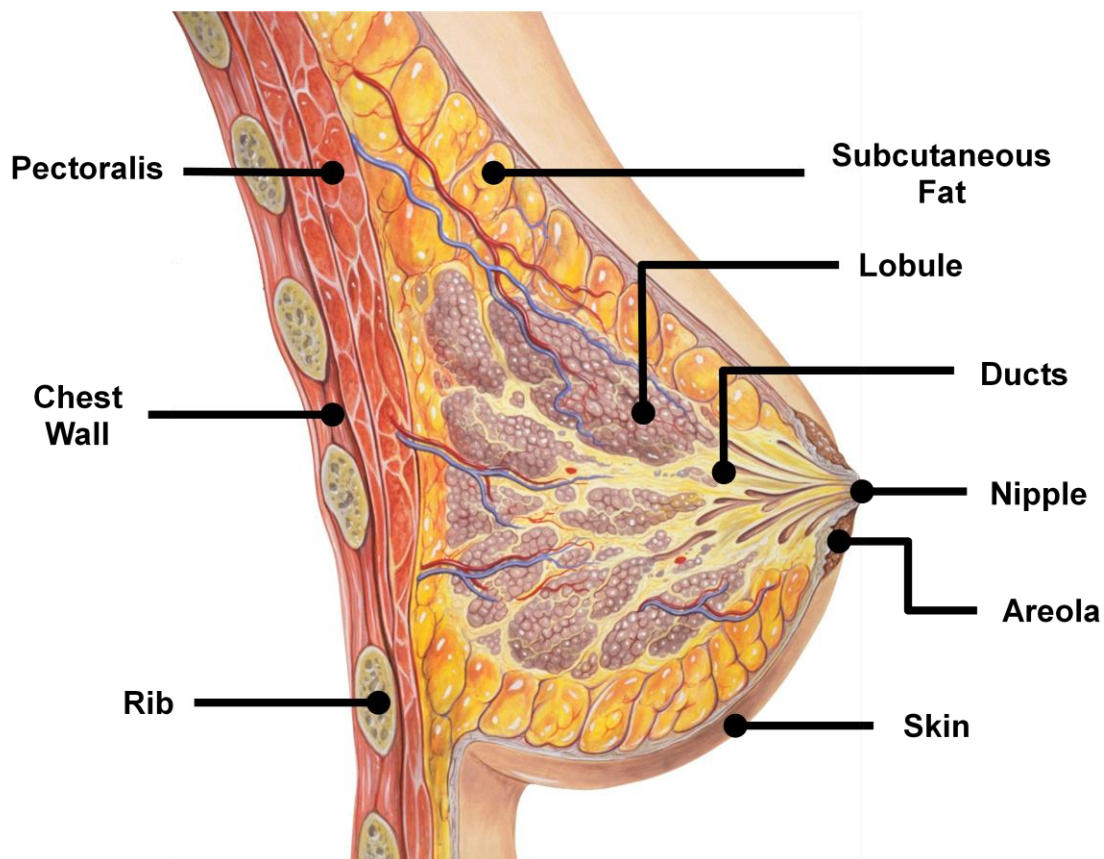


Figure 5: Diagram of the major and surrounding structures of the female breast. Each structure is labeled. Image has been adapted to point to the structures. Original image is copyright Patrick J. Lynch, medical illustrator; and C. Carl Jaffe, MD, cardiologist. And is reprinted with permission from the copyrighter based on the Creative Commons Attribution from Wikipedia.com.

Due to the overlapping of tissue in a 2D radiograph, multiple views are required in a screening mammogram. A typical screening mammogram consists of both a craniocaudal (CC) view and a mediolateral oblique (MLO) view of each breast.³² The MLO view is useful for an alternative view of breast structures and for visibility of the chest wall portion of the breast which is not visible in the CC view.³¹ Patients are positioned in either view and are compressed using

a near radiolucent paddle. The compression is needed to further reduce the amount of tissue overlap present in a 2D mammogram.³³ Compression leads to severe discomfort for patients. The average compression force used in screening mammography is greater than 22 lbs.³³ Even with compression, variations in breast thickness are apparent in mammograms. Variations occur specifically at the periphery of the breast where it is not possible to get uniform breast thickness. **Figure 6** shows a diagram of a compressed breast and the resultant non-uniform breast thickness. The air gaps in the image produce differing levels of X-ray intensity on the detector. Periphery equalization is an image processing technique used to reduce the effect of air gaps.³⁴

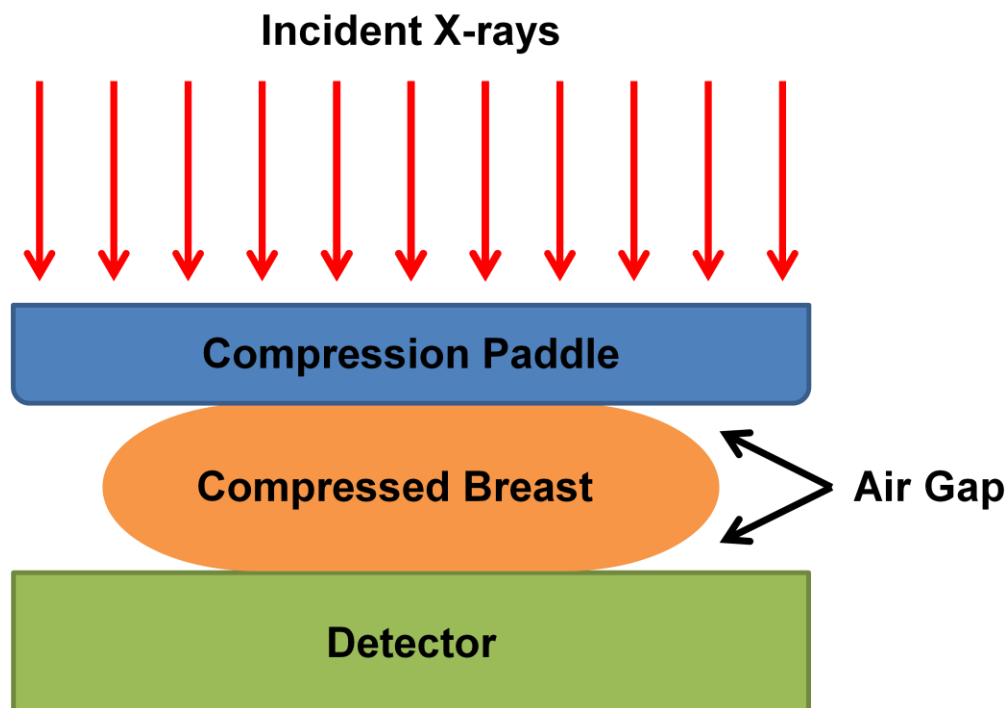


Figure 6: Diagram showing the non-uniformity of breast thickness that occurs even after compression of the breast. The air gaps in the image produce differing levels of X-ray intensity on the detector.

3.2.2 Breast Density

Breast density refers to the amount of fat and fibrous connective tissue that is found in a breast. The Breast Imaging-Reporting and Data System (BI-RADS), is a quality assurance tool designed to keep mammographic standards equivalent for all mammography facilities. BI-

RADS classifies breast density into four categories based on the amount of fibrous tissue present in the breast. **Table 2** shows the BI-RADS classifications for breast density and their respective fatty and fibrous tissue percentages. **Figure 7** shows example 2D radiographs with each BI-RADS density classification. From the figure it can be seen as the breast density increases the image contrast decreases for 2D imaging modalities.

Table 2: BI-RADS breast density classifications. Data taken from Baker et al.³⁵

Classification	Description	Percentage Fatty Tissue	Percentage Fibrous Tissue
BI-RADS 1	Mostly Fat	> 75%	< 25%
BI-RADS 2	Scattered Fibroglandular	51 - 75%	25 - 50%
BI-RADS 3	Heterogeneously Dense	25 - 50%	51 - 75%
BI-RADS 4	Extremely Dense	< 25%	> 75%

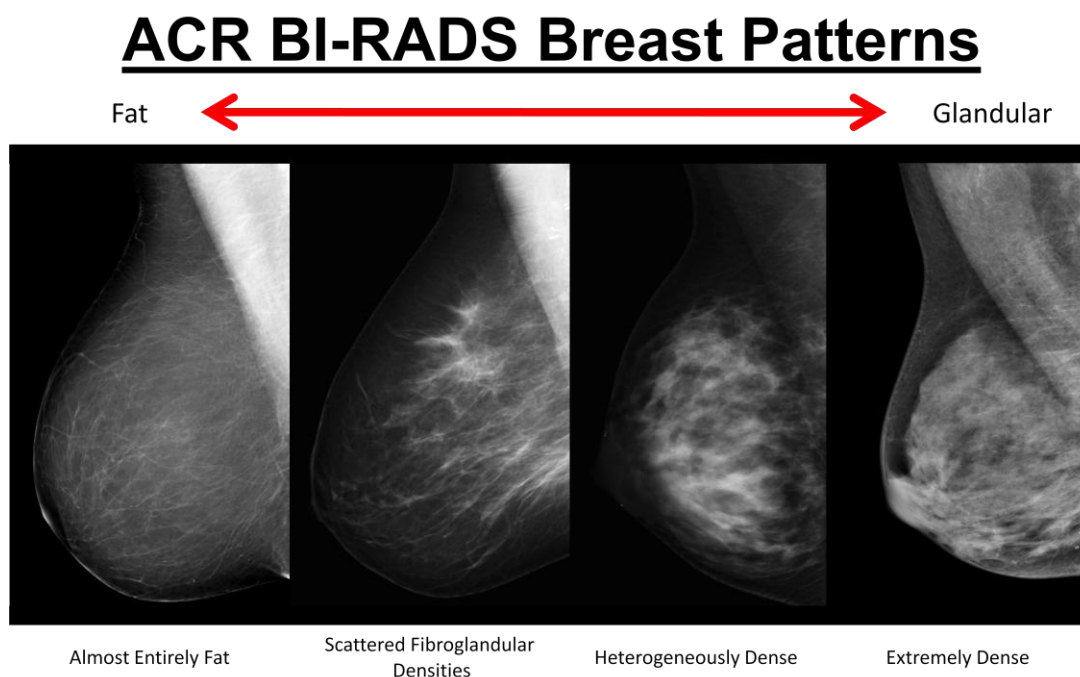


Figure 7: Example 2D projection radiographs of breasts with each BI-RADS density classification. Moving from left to right the densities become more dense. This image is reprinted with permission from Dr. Cherie Kuzmiak from UNC Hospitals.

3.2.3 Masses

There are two types of breast lesions typically associated with breast cancer, masses and MCs. Masses are abnormal groups of cells which could be benign (non-cancerous) or malignant (cancerous). There are a variety of lesions that can be found in the human breast.

Table 3 lists a number of common lesions in the breast with their associated locations and disease.

Table 3: Typical lesions with their associated locations and disease. Data taken from Kopans.³¹

Benign - non-cancerous

Atypical - not associated with benign or malignant

Malignant - cancerous

Name	Location	Disease
Duct ectasia	Major ducts	Benign
Large duct papilloma	Major ducts	Benign
Intraductal carcinoma extending from the terminal ducts	Major ducts	Malignant
Hyperplasia	Minor and terminal ducts	Atypical
Peripheral duct papillomas	Minor and terminal ducts	Benign
Ductal carcinoma	Minor and terminal ducts	Malignant
Cyst	Lobule/Major ducts	Benign
Fibroadenoma	Lobule	Benign
Adenosis	Lobule	Benign
Phylloides tumor	Lobule	Benign
Lobular carcinoma	Lobule	Malignant
Sarcoma	Interlobular connective tissue	Malignant

The BI-RADS system also gives classification of disease. The categorical numbers range from 1 to 6 with 1 being negative and 6 being biopsy proven malignancy. There is also a category 0 which is used in situations where additional evaluation is needed such as a lookup of previous mammograms. **Table 4** shows the BI-RADS categories and their descriptions.

Table 4: BI-RADS classifications of malignancy. Data taken from Eberl et al.³⁶

BI-RADS Category	Description
0	Additional evaluation needed
1	Negative
2	Benign
3	Probably benign
4	Suspicious abnormality
5	High probability of malignancy
6	Biopsy proven malignancy

3.2.4 Microcalcifications

The second type of lesion that is commonly found in a mammogram is MCs. MCs are small deposits of calcium in the breast. Characteristics such as size, distribution, morphology, and variability of the MCs help in the assessment.^{37, 38} MC sizes range from less than 100 μm to more than 1 mm. MCs are present in most post-menopause women. Although not typically associated with cancer, there are some distributions of MCs which can be indicative of cancer.

Table 5 lists various MC distributions and types along with their associated diagnosis.

Table 5: MC types and their associated diagnosis. Data taken from Baker et al.³⁵

Benign - non-cancerous

Atypical - not associated with benign or malignant

Malignant - cancerous

Type of MC	Typical Diagnosis
Milk of calcium	Benign
Rim	Benign
Skin	Benign
Vascular	Benign
Spherical	Benign
Suture	Benign
Coarse	Benign
Large rod like	Benign
Round	Benign
Dystrophic	Benign
Punctate	Benign
Indistinct	Atypical
Pleomorphic	Malignant
Fine branching	Malignant

3.3 Image Quality

Image quality is very important in mammographic imaging. Without a high standard of image quality set by the FDA, different imaging centers could have markedly different diagnoses. The quality of an image can be quantitatively described from three different variables; (1) contrast resolution, (2) spatial resolution, and (3) noise.

3.3.1 Contrast

The contrast of an object in an image is the difference in its apparent attenuation from the background of the image. As the contrast between the object and background becomes smaller, the ability to discern the two becomes more difficult. The contrast of an object can be calculated using the following equation:

Equation 4:

$$C_O = \frac{S_O - S_B}{S_B}$$

Where " C_O " is the contrast of the object, " S_O " is the signal intensity of the object, and " S_B " is the signal intensity of the background near the object. In an X-ray based medical imaging system the contrast resolution is affected by 4 major factors; (1) radiation dose, (2) X-ray attenuation coefficient of the object being imaged, (3) X-ray scatter, (4) and (5) image processing.

Two factors can be adjusted in a X-ray system to change the radiation dose. Decreasing the anode potential will decrease the dose and increase the contrast of the image. Higher energy X-rays are less likely to be attenuated by soft tissue. The caveat of decreasing the anode potential is that lower energy X-rays will be absorbed more readily and if the object is sufficiently dense, no X-rays will reach the X-ray detector. Increasing the X-ray tube exposure (current times pulse width) will increase the contrast of the image, unless the anode potential is too low to allow for X-rays to pass through the object. Increasing the exposure increases the

number of photons exiting the X-ray tube thus increasing the number of photons reaching the detector. Looking back at **Equation 4** it can be seen that increasing the number of photons reaching the detector will increase the signal intensity of the object and the signal intensity of the background. Since the X-ray attenuation coefficient is larger for the object than the background, the signal will increase at a faster rate for the background compared to the object thus increasing the contrast in a given period of time. Since increasing the radiation dose to the patient could increase the chance of having cancer at a later time, careful consideration must be taken into the tradeoff of contrast versus radiation dose.

The difference in the attenuation coefficient of an object and its background, along with differences in thickness, is the underlying reason why there is contrast in an X-ray based imaging system. If all objects in an image had the same thickness and attenuation coefficient then there would be no contrast in the resultant image. **Figure 8** shows the effect of attenuation coefficient on image contrast. In the figure the green attenuating object will attenuate twice the amount of X-rays at the given energy than the blue object. The image on the right shows how all contrast is lost when the green object is exactly half the thickness of the blue object. This is due to the apparent equal total attenuation of the two objects.

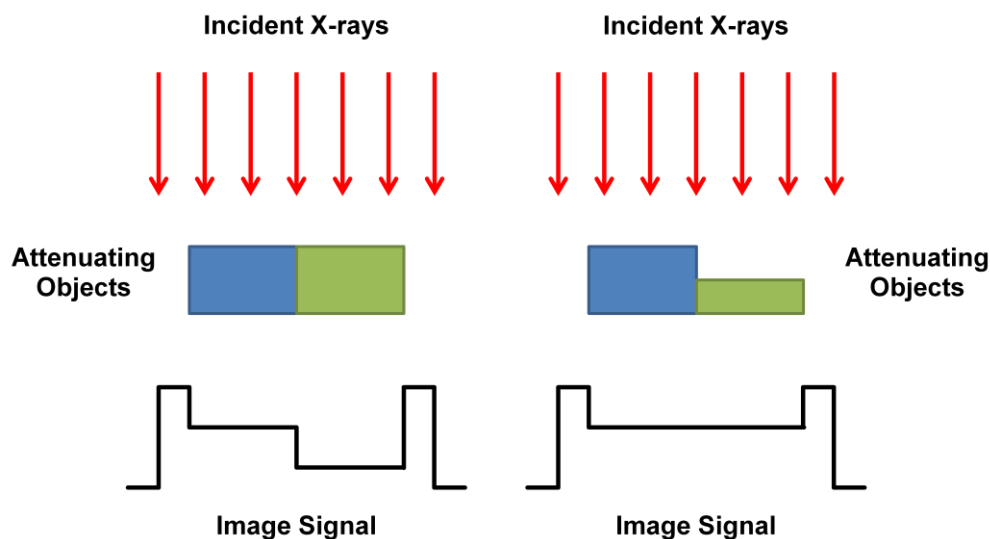


Figure 8: Demonstration of the effect of the attenuation coefficient on the contrast of an image. The green attenuating object will attenuate twice the amount of X-rays at the given energy than the blue object.

The image on the **Left** shows that when the objects have the same thickness contrast between the two objects can be seen. However, the image on the **Right** shows that if the green object has half the thickness of the blue object there is no contrast between the two. This is for demonstrative purposes and does not necessarily represent an actual imaging system.

X-ray scatter is detrimental to image contrast. Scatter is present in all X-ray based imaging. For absorption based X-ray imaging it causes a decrease in image contrast. Scatter produces a continuous low frequency baseline across the whole image. When looking at **Equation 4**, scatter would add constant number to the object and background signal. Since the numerator would cancel out the constant number, the number would only be added to the denominator. This effectively reduces contrast.

Image processing can be used in digital mammography to enhance the contrast of lesions. Pisano et al. used contrast limited adaptive histogram equalization (CLAHE) on digital mammograms in order to increase the contrast of spiculated masses.³⁹ Low contrast spiculated masses were simulated in dense mammograms. A group of readers reviewed the images. It was found that mass visualization was significantly improved for cases where CLAHE had been used.³⁹ There are many other image processing techniques which improve contrast. A simple adjustment of the histogram will increase image contrast. An image histogram is a chart displaying all the grayscale levels (typically 0 to 2^{16}) and their total densities in the image. **Figure 9** shows an image before adjustment of the histogram (**Left**) and after adjustment of the histogram (**Right**). After adjustment of the histogram, the contrast is increased and structures in the image become visible. These methods of contrast adjustment will cause an increase in noise in the images. Noise reduces the visibility of both masses and MCs in mammograms. Noise will be covered more in depth in **Section 3.3.3**.

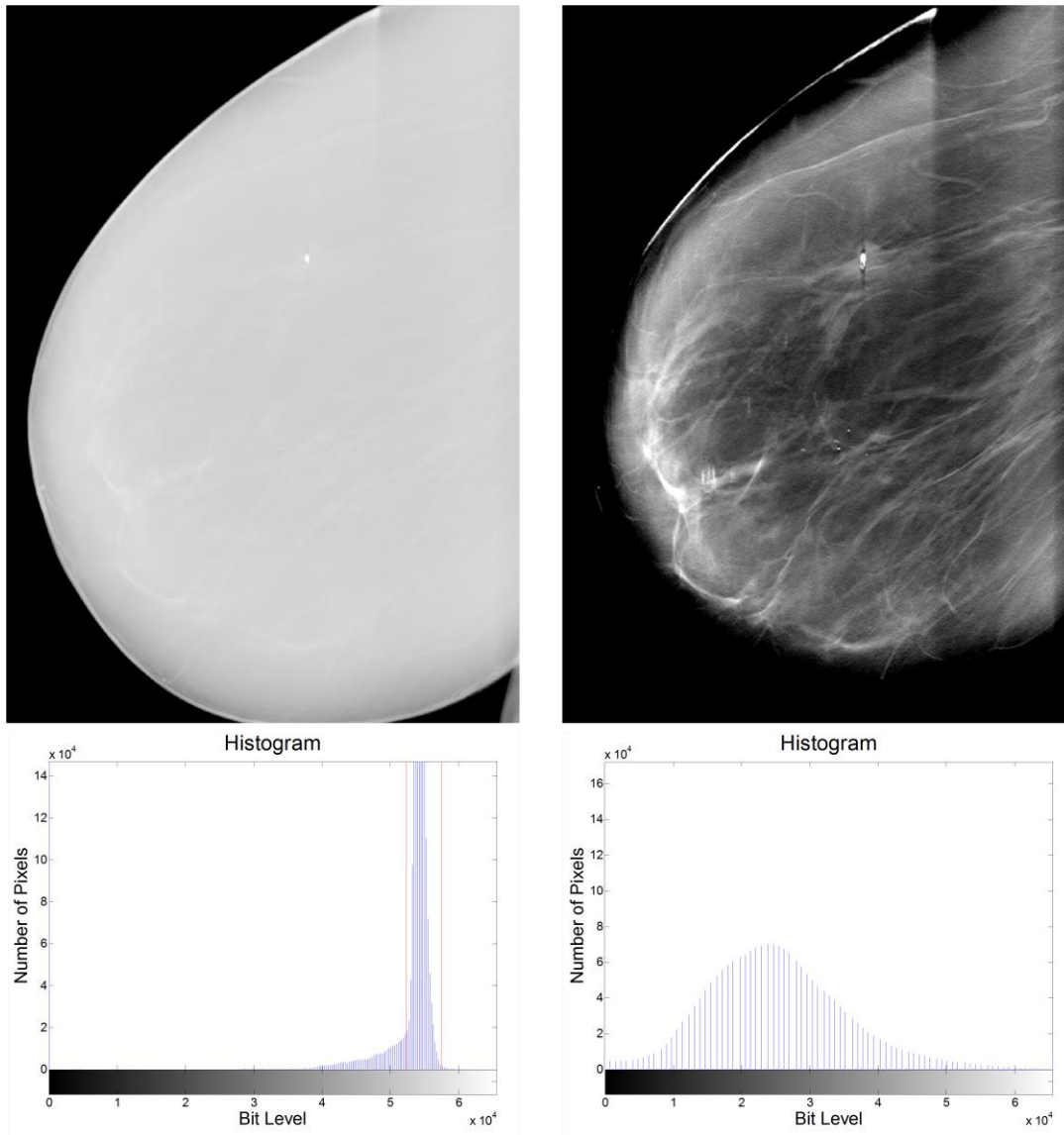


Figure 9: Left - An MLO image of a breast (**Above**) without adjusting the image (**Below**). Right - Same image (**Above**) with adjustment of the histogram (**Below**). The red bars on the original histogram show the window at which the changed histogram is contained in. This case is greatly exaggerated.

3.3.2 Spatial Resolution

The term spatial resolution describes the ability of an imaging system to resolve objects in the spatial domain. A simple explanation is the ability of a system to resolve two objects as they become smaller and closer together. Large objects that are far apart can be visualized as two distinct objects. A system that can resolve smaller objects that are closer together, as distinct objects, is said to have better spatial resolution. In a x-ray based medical imaging systems the spatial resolution is affected by 4 major factors; (1) focal spot size and viewing

angle, (2) detector pixel size, (3) reconstruction and post-processing algorithms, and (4) radiographic magnification factor.

The focal spot size has a direct effect on the spatial resolution of a system. A smaller focal spot size will result in a higher spatial resolution. Another factor affecting the spatial resolution is the viewing angle of the focal spot on the detector (effective focal spot). Viewing angles that are closer to perpendicular with the anode surface have a smaller effective focal spot size thus a higher spatial resolution. This effect is only applicable in the anode-cathode direction of the system. The focal spot size is constant in the other direction.

Since medical imaging uses sampled signals even with an ideal system in other aspects the spatial resolution of the system is still degraded by the size of the samples, detector pixel size. As a rule of thumb, smaller pixel sizes result in better spatial resolution. The crystals in screen film systems are smaller in size than current digital detector pixel sizes, resulting in a higher spatial resolution for screen film systems. This was a particularly large concern for mammography when the change from screen film systems to digital systems was first proposed.⁴⁰ High spatial resolution is needed in mammography in order to visualize MCs which depending on size and structure can indicate if a particular lesion is benign or malignant.³⁷

For tomographic imaging modalities, like digital breast tomosynthesis, the reconstruction algorithm can affect the spatial resolution of the system. Wu et al. compared filtered backprojection (FBP) to a maximum likelihood (ML) method. They reported that FBP had higher spatial resolution but higher noise than ML.⁵ Resolution can also be increased by reconstructing pixel sizes which are smaller than the detector pixel size. Acciavatti and Maidment investigated using sub-pixel resolution in a DBT system.⁴¹ They found that they could reconstruct objects smaller than the detector pixel size without aliasing occurring.

For systems with small focal spot sizes, radiographic magnification can be used in order to increase the size of the objects being imaged. Since x-rays are divergent, objects closer to the x-ray source will appear larger on the detector than the same sized object closer to the

detector. The equation below can be used to determine the magnification factor of the object being imaged:

Equation 5:

$$M = \frac{SID}{SOD}$$

Where "M" is the radiographic magnification factor, "SID" is the source to imager distance, and "SOD" is the source to object distance. In practice large magnification factors are not useful because of the large detector size needed and the increased penumbra of the focal spot. **Figure 10** shows the effect of the magnification on the penumbra of the focal spot. The penumbra can be calculated from the following equation:

Equation 6:

$$Pn = F * \frac{SID - SOD}{SOD} = F * (M - 1)$$

Where "Pn" is the size of the penumbra on the detector, "M" is the radiographic magnification factor, "SID" is the source to imager distance, "SOD" is the source to object distance, and "F" is the focal spot size in a plane parallel to the detector. If small focal spots are used then the dominant factor of the spatial resolution is the detector pixel size and not the penumbra of the focal spot.

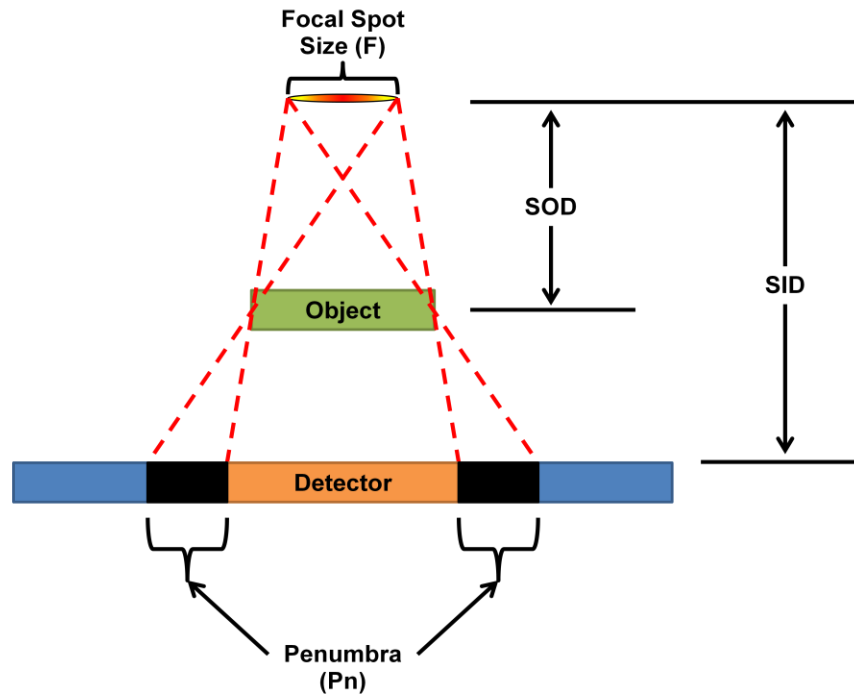


Figure 10: Illustration of the effect of radiographic magnification on the penumbra of a non-ideal focal spot. Ideal focal spots are not possible in X-ray tubes so this effect is visible in every radiographic imaging system.

In practice the spatial resolution depends on all four of these factors. However, another factor must be taken into account while imaging live patients, patient motion. This is a large concern for adjunct mammographic imaging modalities such as digital breast tomosynthesis as it has been shown that patient motion can have a more adverse effect on spatial resolution than the previous mentioned factors.¹⁶ Faster acquisition times will result in average decreases in patient motion. All these factors must be taken into account when creating a system with high spatial resolution. However, system cost must be taken into account as well.

3.3.3 Noise

Both contrast and spatial resolution allow for visualization of objects in radiographic images. However, noise reduces visualization of objects in images. Noise is random fluctuations in images. If noise is sufficiently large compared to the contrast or spatial resolution, it could completely cover up a lesion in a X-ray image. The following equation shows the relationship between object visibility and noise:

Equation 7:

$$CNR = \frac{C_o}{\sigma}$$

Where "CNR" is the contrast to noise ratio, "C_O" is the object contrast as calculated by **Equation 4**, and "σ" is the standard deviation of the region of interest. Using this equation, a large standard deviation would result in reduced visibility of the object. This equation, although commonly used, does not properly quantify the visibility of an object. For example, if the signal of an object was 20, the background signal was 10, and the standard deviation was 4, then the CNR would be 0.25. If a constant number of 5 was removed from the entire image, the standard deviation would stay the same, the object signal would become 15 and the background signal would become 5. Now the CNR is 0.5, but looking at the image there would be no visible difference in the image. A more useful equation is the signal difference to noise ratio (SdNR), which removes the denominator in the contrast calculation resulting in the following equation:

Equation 8:

$$SdNR = \frac{S_o - S_B}{\sigma}$$

Where the variables are equivalent to the previously described variables of the same name. Using this equation, the removal of the constant number 5 would result in the same value as without the removal, 2.5. Resolution and noise are very important in mammographic imaging due to the extremely small size of MCs. Some MCs can be near the size of a detector pixel.³⁷ Small pixel by pixel fluctuations caused by noise could either be mistaken as MCs which could lead to false positive diagnosis, or worse, could cover up MCs which could lead to false negative diagnosis. There are many factors in an imaging system that can contribute to noise. However, there are two types of noise that contribute the most; (1) quantum noise and (2) electronic noise.

Quantum noise comes from the fact that X-ray production is a random process. If a single electron is bombarded onto the anode, the direction, energy, and number of photons created will vary from those of different electrons bombarding the anode. If the number of electrons is sufficiently high, then the X-ray source will create its spectrum in every direction. Even when sufficiently high, there are random fluctuations in photon counts at the X-ray detector. In most circumstances, quantum noise accounts for the majority of noise in images. Increasing the exposure of an image increases the noise as well as the photon count. However, the photon count will increase at a higher rate than the noise will. If the signal increases by a factor of N then the noise will increase by a factor of \sqrt{N} .

Electronic noise is a problem for digital imaging systems. It comes from random electrical spikes. In imaging systems, the noise is closer to a constant. It becomes a non-factor at a certain dose. But if the dose is low, the electronic noise could have similar effects on contrast as quantum noise.

3.4 Image Interpretation

The interpretation of mammographic images is very important for diagnosis of breast cancer. Even well trained radiologists misdiagnose patients. The misdiagnosis is not necessarily the radiologist's fault, the imaging system also plays an important part in the image interpretation. All of radiology use a set of terms to describe the interpretation of images with respect to disease truth. The following paragraphs will cover the majority of these terms.

True positive (TP), true negative (TN), false positive (FP), and false negative (FN) relate to the ability of a imaging system and image viewer (CAD or human) to accurately determine if a patient is positive or negative for the disease being screened. **Table 6** is a chart that will be used in order to more easily explain these terms. In the chart, columns represent the disease truth and rows represent the diagnosis of the radiologist based off the acquired images.

Table 6: Determination of TP, TN, FP, and FN base off disease truth and diagnosis.

		Disease Truth	
		Positive	Negative
Diagnosis	Positive	TP	FP
	Negative	FN	TN

TP is defined as the number of people diagnosed as positive that were actually positive.

TN is defined as the number of people diagnosed as negative that were actually negative. FP is defined as the number of people that were diagnosed as positive but were later determined to be negative. FN is the number of people that were diagnosed as negative but were later determined to be positive.

Sensitivity and specificity are statistical measures which describe the performance of the imaging system and the reader. Sensitivity is defined as the fraction of people who are accurately diagnosed as positive for disease. It can be calculated using this equation:

Equation 9:

$$Sensitivity = \frac{TP}{(TP + FN)}$$

Specificity is defined as the fraction of people who are accurately diagnosed as negative for disease. It can be calculated using this equation:

Equation 10:

$$Specificity = \frac{TN}{(TN + FP)}$$

A receiver operating characteristic (ROC) curve is a visual representation of the performance of a imaging system. It is created by plotting the sensitivity on the y-axis versus varying levels of the false positive rate (1-specificity) on the x-axis. For comparison between two systems the area under the ROC curve (AUC) is used. A larger AUC would indicate that a system is more likely to produce TPs and TNs than FPs and FNs.

Accuracy is equivalent to the ratio of the number of patients accurately diagnosed to the total number of patients. A system that has a point at the exact upper left corner of the ROC curve would be a system that is 100% accurate. If a system was equivalent to completely random guesses then the accuracy of the system would be 50%. **Figure 11** is a ROC curve of a system which has an accuracy of 50%. Such systems do not exist in actual practice but serve well as a demonstration of a ROC curve. A system that has a point anywhere in the bottom right of the ROC curve would be a system where you are statistically more likely to get the diagnosis wrong than right. If that is the case just take the opposite of what is diagnosed as the actual diagnosis. This would invert the ROC curve and give you an imaging system which is in the upper left portion of the curve.

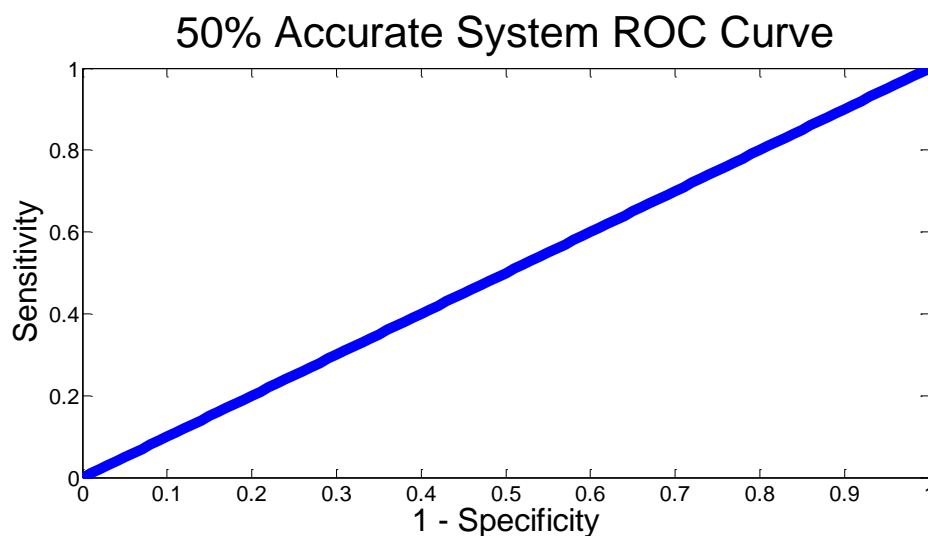


Figure 11: A ROC curve that shows a system that has an accuracy of 50%. If such a system existed, a random guess of diagnosis would give you the same results as diagnosing based off the system.

REFERENCES

- 1 N. Howlader, A. Noone, M. Krapcho, N. Neyman, R. Aminou, W. Waldron, S. Altekruse, C. Kosary, J. Ruhl, Z. Tatalovich, "SEER Cancer Statistics Review, 1975-2008, National Cancer Institute. Bethesda, MD," SEER website(2011).
- 2 D.B. Kopans, *Breast imaging*. (Wolters Kluwer Health, 2007).
- 3 K. Kerlikowske, D. Grady, S.M. Rubin, C. Sandrock, V.L. Ernster, "Efficacy of screening mammography," JAMA: the journal of the American Medical Association **273**, 149-154 (1995).
- 4 A. Poulos, D. McLean, M. Rickard, R. Heard, "Breast compression in mammography: How much is enough?," Australasian radiology **47**, 121-126 (2003).
- 5 E.D. Pisano, E.B. Cole, B.M. Hemminger, M.J. Yaffe, S.R. Aylward, A.D. Maidment, R.E. Johnston, M.B. Williams, L.T. Niklason, E.F. Conant, "Image Processing Algorithms for Digital Mammography: A Pictorial Essay1," Radiographics **20**, 1479-1491 (2000).
- 6 J.A. Baker, P.J. Kornguth, C. Floyd Jr, "Breast imaging reporting and data system standardized mammography lexicon: observer variability in lesion description," AJR. American journal of roentgenology **166**, 773-778 (1996).
- 7 M.M. Eberl, C.H. Fox, S.B. Edge, C.A. Carter, M.C. Mahoney, "BI-RADS classification for management of abnormal mammograms," The Journal of the American Board of Family Medicine **19**, 161-164 (2006).
- 8 M. Itani, A.T. Griffin, G.J. Whitman, "Mammography of breast calcifications," Imaging **5**, 63-74 (2013).
- 9 E.A. Sickles, "Breast calcifications: mammographic evaluation," Radiology **160**, 289-293 (1986).
- 10 E.D. Pisano, S. Zong, B.M. Hemminger, M. DeLuca, R.E. Johnston, K. Muller, M.P. Braeuning, S.M. Pizer, "Contrast limited adaptive histogram equalization image processing to improve the detection of simulated spiculations in dense mammograms," Journal of Digital Imaging **11**, 193-200 (1998).
- 11 N. Karssemeijer, J.T. Frieling, J.H. Hendriks, "Spatial resolution in digital mammography," Investigative radiology **28**, 413-419 (1993).
- 12 T. Wu, R.H. Moore, E.A. Rafferty, D.B. Kopans, "A comparison of reconstruction algorithms for breast tomosynthesis," Med Phys **31**, 2636 (2004).
- 13 R.J. Acciavatti, A.D. Maidment, "Investigating the potential for super-resolution in digital breast tomosynthesis," SPIE Medical Imaging, (2011).
- 14 R.J. Acciavatti, A.D. Maidment, "Optimization of continuous tube motion and step-and-shoot motion in digital breast tomosynthesis systems with patient motion," Proc. SPIE **8313**, (2012).

CHAPTER 4: MAMMOGRAPHIC IMAGING MODALITIES

4.1 Overview

Due to the unique nature of breast cancer and the complex imaging needed to visualize breast masses and MCs, the food and drug administration (FDA) has developed the Mammography Quality Standards Act (MQSA) which outlines the requirements for mammography accreditation. The MQSA allows for three modalities to be used in screening mammography: (1) screen film mammography (SFM), (2) full field digital mammography (FFDM), and (3) digital breast tomosynthesis (DBT). Some adjunct imaging modalities may be used in certain situations to enhance the findings in these three modalities. The major adjunct imaging modalities are ultrasound and magnetic resonance imaging (MRI). There are also many imaging modalities which are under investigation for use in mammography. The major investigative modality is computed tomography (CT). The following chapter will cover the above mentioned modalities and cover some clinical papers involving said modalities.

4.2 Screening Mammography Modalities

4.2.1 Screen Film Mammography

SFM utilizes a film to record, display, and storage an image. The film contains three layers: the base, the adhesive layer, and the emulsion layer. The adhesive layer keeps the base and emulsion layers together. The emulsion layer contains silver halide crystals. Photons are absorbed by the silver halide and electrons are ejected. These electrons collect on the sensitivity center. The negative charge build up attracts the silver ions and neutralizes them. This deposits the black silver particles permanently into the emulsion. Afterwards, the excess granules are washed away. The contrast in these images exist between areas of silver concentration and the areas with less silver concentration.^{31, 42} Sometimes intensifying screens

are used in conjunction with the film. Intensifying screens are made of fluorescing materials (gadolinium oxysulfide for example) which produce light when they absorb X-ray photons. These screens are typically located below the film so that X-rays must pass through the film first before reaching the intensifying screen. Intensifying screens produce exponentially higher amounts of light at the entrance of the X-ray photons. In order to preserve the spatial resolution of SFM, the film must be located at the closest location to where the light is emitted which is why they are located on top of the intensifying screen. In the past SFM was the gold standard for mammography screening examinations. In more recent years, although still in use in some areas, SFM has become less popular than FFDM

4.2.2 Full Field Digital Mammography

In recent years the continued development of digital detectors has allowed for their use in mammographic imaging. The ease of image acquisition, manipulation, and storage has made full field digital mammography (FFDM) the gold standard for screening mammography. The major differences between SFM and FFDM is the image collection method, storage, and display. This section will cover the major differences between the two modalities and the implications of using FFDM in the clinic.

There are two types of digital detectors that are currently used in FFDM; indirect conversion detectors and direct conversion detectors. Indirect conversion detectors are the older of the two detector technologies. Images are acquired in a two step process, similar to SFM. X-rays are first absorbed by a scintillator (Cesium Iodide doped with Thallium is a common scintillator material) which then produces a light scintillation. The light photons are then detected by an array of photodiodes. These diodes convert the light to electrical signals which are then detected by either thin film transistors (TFTs) or charge-coupled devices (CCDs). The signals generated by the TFTs or CCDs are then sent to a computer to generate the image. Unlike SFM, the scintillator layer is located above the light detection layer since photodiodes are

not X-ray transparent as intensifying screens. This causes spatial resolution degradation which can become a problem when imaging MCs. Each individual photodiode represents a pixel. Smaller pixels lead to increased spatial resolution. Smaller pixels become superfluous at some point due to light scatter. The Cesium Iodide scintillator is commonly used due to the reduction in light scatter, this comes at a cost to sensitivity. Indirect conversion detectors using a Cesium Iodide scintillator will have a quantum efficiency between 50 and 70%. For these reasons, careful consideration must be made when determining the scintillator thickness in a indirect detector.⁴²

Direct conversion detectors use a single step process for conversion of X-ray photons to electrical signals. This removes the problems associated with light scatter that hampers indirect conversion detectors. In each pixel in a direct conversion detector, a photoconductor transforms a X-ray photon to an electron-hole pair through the photoelectric effect. When an external electric field is applied, these electron-hole pairs drift toward an electrode and are collected on a capacitor. Minimal charge spreading occurs because the electron-hole pairs travel along the axis of the electric field, leading to a narrow point spread function.¹⁰ The charge on the capacitor directly correlates to the amount of absorbed photons and is sent to the computer for image creation. Typical FFDM systems use amorphous selenium as the photoconductor. Amorphous selenium is useful as a photoconductor due to its high efficiency of X-ray absorption. Large thicknesses of selenium can be used to increase stopping power without a loss in spatial resolution due to the method of electron-hole pair collection used in direct conversion detectors. With a thickness of 250 μm of selenium, a direct conversion detector can stop more than 95% of X-rays in the mammographic range.⁴²

The direct conversion detector is superior to the indirect conversion detector in terms of spatial resolution. A direct conversion detector will have a higher detective quantum efficiency (DQE) compared to an indirect conversion detector with the same pixel size. DQE is a quantitative measure of the efficiency of a detector based on image contrast and resolution.

The high resolution needed mammography requires the use of small pixel sizes and therefore direct conversion detectors are typically preferred over indirect conversion detectors.⁴²

When FFDM was first introduced into the screening population, concerns over system cost and spatial resolutions came up.⁴³ With screen film systems capable of producing spatial resolutions up to 20 lp/mm and at a substantially lower cost, the contrast benefit of digital mammography systems was diminished.⁴² A benefit of FFDM over SFM is the linear nature of the intensity profile. As the X-ray intensity increases on the detector, the image contrast increases at the same rate. This is in contrast to SFM where there is a nonlinear relationship between X-ray intensity and film contrast. For optimal contrast in a SFM system, the exposure must be adjusted to account for the nonlinearity. Another benefit of FFDM is the ability to digitally store and post-process images. This allows for rapid display and transfer of images, and for image processing techniques which can increase lesion contrast.³⁴ SFM also has reduced visibility in radiographically dense breasts.⁴⁴

The diagnostic performance of FFDM and SFM mammography were compared in a large multisite clinical trial called the Digital Mammographic Imaging Screening Trial (DMIST). DMIST had a total of 49,528 patients at 33 sites in the United States and in Canada. Patients with no previous breast cancers were imaged using both SFM and FFDM. The images were then interpreted by two radiologists. ROC analysis was used as evaluation. For all patients, the diagnostic accuracy of FFDM was similar to SFM (difference in AUC = 0.03; P = 0.002). Comparing the results for patients under the age of 50 showed a significantly higher accuracy in FFDM (difference in AUC = 0.15; P = 0.002). Higher accuracies for FFDM were also recorded for heterogeneously and extremely dense breasts (difference in AUC = 0.11; P = 0.003) and pre or perimenopausal women (difference in AUC = 0.15; P = 0.002). The study concluded that although the overall accuracy of the two modalities was similar, FFDM is more beneficial than SFM in some populations.⁴³

4.2.3 Digital Breast Tomosynthesis

Breast cancer is the most common type of cancer found in women in the United States, with more than 200,000 new cases found each year.¹ When the cancer is diagnosed at an early stage the five-year relative survival rate is between 83.9 and 98.4 percent. This number drops to 23.8 percent when the cancer is diagnosed at a stage at which it has already metastasized.¹ Screening mammography is the current gold standard for early detection of breast cancer.^{2, 3} However, 2D mammography imaging lacks depth information, which can cause underlying and overlying tissue to obstruct the view of lesions. This leads to high false positive and false negative rates.^{4, 5}

Digital breast tomosynthesis (DBT) uses multiple low dose projection images distributed over an angular span to create a pseudo-3D reconstruction of the breast. The reconstruction method is based on the Fourier Slice Theorem. This added depth information allows for otherwise obscured lesions to become visible.^{6, 8, 9} Two acquisition methods are used in current DBT systems: step-and-shoot, and continuous motion. In both methods, a single X-ray source is rotated about the angular span. In continuous motion DBT, the X-ray source is rotated continuously over the angular span even during image acquisition.^{10, 11} This leads to short acquisition times at the cost of spatial resolution. In step-and-shoot, the X-ray source is rotated and stops at the angle at which the projection will be taken. It then continues rotating until the next angle is reached.¹² This method has higher spatial resolution than the continuous motion system but has long acquisition times which lead to patient motion which is more detrimental to image quality than focal spot blur.¹⁶

The Hologic Selenia Dimensions DBT system was FDA approved for use in screening mammography in early 2011. It is currently the only FDA approved DBT system. In the system the DBT acquisition is followed by a traditional FFDM. This double acquisition is called combination mode (combo mode) and effectively doubles the dose to the patient. The FFDM is used to visualize MCs which the DBT acquisition cannot otherwise visualize. Many recent

clinical trials have shown that the combo mode of the Selenia Dimensions increases in the AUC compared to FFDM alone^{45, 46}. Recall rates for benign cases significantly decrease when using a combination of DBT and FFDM^{8, 45-47}. However, for cases with microcalcifications (MCs), the use of DBT along with a FFDM image has shown no significant improvement in the AUC⁴⁶.

4.3 Adjunct Mammographic Imaging Modalities

4.3.1 Ultrasound

Ultrasound imaging uses high frequency sound waves, above the frequency at which humans can hear, to image variations in tissue densities.²² It is a useful tool in mammography due to its low cost, portability, and use of non-ionizing radiation. In ultrasound, the sound waves are produced by a handheld transducer. As these waves propagate through tissue they will either be reflected, absorbed, refracted, or scattered when tissue boundaries are crossed. Waves that are reflected back to the transducer the waves amplitude and delay can be measured. Based on this, a 2D image can be calculated.

Ultrasound is typically used in mammography as a supplemental view to 2D screening mammography. It is especially useful in breasts with BI-RADS density classifications between 3 and 4. A study by Corsetti et al. compared screening mammography for fatty breast versus screening mammography and breast ultrasound for dense breasts.⁴⁸ A total of 8865 women were imaged over a six year span. The cancer rates for women with dense breasts was higher (8.3/1000) than women with fatty breasts (6.3/1000). An average of 4.4/1000 more cancers were found in dense breasts using ultrasound and mammography compared to mammography alone. The overall screening sensitivity was 83.5% for mammography in fatty breasts and 86.7% for mammography and ultrasound in dense breasts.⁴⁸

Ultrasound is useful as an adjunct imaging modality in mammography. The high sensitivity to density changes in tissue allows for visualization of masses that would otherwise

have been undetected by 2D mammography. It is especially useful in women with dense breasts, which have severe tissue overlap in images which results in false diagnosis. It is also useful in determining if masses are cysts (non-cancerous) due to the fluid filled nature of such lesions. This helps reduce the number of needle core biopsies. Even with its low cost, use of non-ionizing radiation, and high sensitivity for masses ultrasound cannot be used for screening mammography alone. It has poor depth penetration which becomes a problem for thicker breasts. It also has poor spatial resolution and high levels of noise, both of which are detrimental to MC visibility. Even with these caveats ultrasound serves an important role in mammography.⁴²

4.3.2 Magnetic Resonance Imaging

MRI is based on the nuclear magnetic resonance of nuclei. Nuclei with odd atomic numbers have spin. When a large external magnetic field is applied to the nuclei the spins will align. The protons will absorb radiofrequency pulses thus changing the dipole alignment. The absorbed energy is re-emitted after the pulse. The remitted energy can then be measured based on frequency and phase and an image can be created. MRI produces high contrast images of soft tissue, due to the abundance of hydrogen. The high soft tissue contrast is beneficial in mammographic imaging. MRI is sometimes used for preoperative imaging for better visualization of disease extent.^{22, 42}

Mann et al. studied the impact of preoperative breast MRI on the rate of re-excision in invasive lobular carcinomas. A total of 267 patients were enrolled in the study. Of the 267 patients, 99 had preoperative MRIs along with standard clinical care imaging. The other 168 patients only had standard clinical care imaging. A significant decrease in the re-excision rate when using preoperative MRI, 9% compared to 27% in the non-MRI group. There was also a decrease in the mastectomy rate, 48 versus 59%. They concluded that preoperative MRI can reduce re-excision rates and mastectomies in patients with invasive lobular carcinomas.⁴⁹

However, another study conducted by Peters et al. was setup similarly but for patients with nonpalpable lesions (BI-RADS Classification 3-5). There were 207 patients in the MRI group and 211 patients in the non-MRI group. The re-excision rate was higher for the MRI group (45%) compared to the non-MRI group (28%).⁵⁰ In general, MRI is not recommended for all patients. In some situations the MRI does not change the surgery outcome. Even worse, in some situations the MRI could cause more re-excisions.⁵¹

The high soft tissue contrast of MRI allows for great visualization of some types of lesions. However, due to low spatial resolution and high false positive rates it should not be used for screening purposes and is more ideally suited as a complementary modality. Careful consideration should be used when using MRI in preoperative situations.^{42, 51}

4.4 Major Investigative Modality

4.4.1 Computed Tomography

Breast CT is a 3D imaging system which uses a large number of low dose angular projection images to reconstruct the 3D volume. The 3D representation removes the tissue overlap that is found in planar imaging and thus has significantly higher lesion contrast compared to 2D imaging modalities. Although not currently used in the clinic, many groups are investigating the potential benefits of breast CT.

The Fourier Slice Theorem is the basis for which CT is able to produce 3D images based on 2D projection images. The Fourier Slice Theorem states that the Fourier transform (FFT) of a projection of a 2D object onto a 1D array will produce a slice of the 2D FFT of the object at the angle from which the projection is taken. The Radon transform is an integral of the 1D projection image. Thus the FFT of the Radon transform at angle \emptyset is the slice of the 2D FFT in polar coordinates at angle \emptyset . If sufficient 1D projections are taken at different angles, then enough information can be constructed in the Fourier domain to reconstruct the object by using the inverse FFT (iFFT). As the number of angular projections approaches infinity the Fourier

domain will be filled in. In clinical practice it is unfeasible to approach an infinite number of projections. This leads to under sampling of the Fourier domain especially in the higher frequencies. Interpolation is needed to fill in the information. Typically, a ramp filter is applied to the iFFT in order to compensate for the low signal strength in the high frequency range compared to the low frequency range. The iFFT gives the estimation of the 2D object. For a 3D object the process must be repeated by stepping in the z-direction or by using a cone beam X-ray. When using a cone beam X-ray, further calculations must be made to account for the X-rays which are not in the perpendicular plane of the X-ray beam.

The use of CT in medical imaging has increased rapidly since the inception of it in the 1970s.⁵² Even compared with the relatively high X-ray dose associated with the soft tissue in mammography imaging, medical CT has more than three times the dose than screening mammography.⁵² The high contrast associated with CT would be extremely beneficial in mammographic imaging. However, reducing the X-ray dose to the patient would be of the utmost concern due to the almost yearly screening mammograms. Breast CT was originally developed in the 1970s but to little avail due to long acquisition times and poor image quality.⁵³ Further research into breast CT was not initiated until flat panel detectors became widely available and reliable. A group out of the University of California, Davis (UC Davis) has recently developed a dedicated breast CT system with a lot of promise.⁵⁴ As with other recent dedicated breast CT systems,^{55, 56} the system is a single breast tabletop design, which is in contrast to the early systems which imaged the entire thoracic cavity. In this design the patient lays flat on a table with the breast lowered into a hole in the tabletop. A single thermionic X-ray source is then rotated around the patient's breast. This setup is similar to current dedicated stereotactic breast biopsy systems. A characterization study conducted by Kwan et al. showed that with an acquisition time of 17s for 500 projection images, the system was capable of producing modulation transfer function values between 1 and 2 cycles/mm with a 10% cutoff.⁵⁷ This is significantly lower than the spatial resolution in FFDm which can be higher than 8

cycles/mm.⁵⁸ The system was used in a small clinical trial where 69 patients were imaged. Breast CT images were compared to SFM. It was found that Breast CT performed similar to screen film mammography with respect to masses in the breast. However, MCs were not as well visualized on the breast CT system compared to SFM. The patients reported that breast CT was significantly more comfortable than the SFM.⁵⁹ This is due to the fact that breast CT requires no breast compression. From this early paper it can be seen that the only added benefit of breast CT at this time was reduced pain to the patient. However, the reduction in MC visibility could cause a serious problem for screening patients.

REFERENCES

- 1 D.B. Kopans, *Breast imaging*. (Wolters Kluwer Health, 2007).
- 2 M.K. Markey, *Physics of Mammographic Imaging*. (CRC Press, 2012).
- 3 M. Bissonnette, M. Hansroul, E. Masson, S. Savard, S. Cadieux, P. Warmoes, D. Gravel, J. Agopyan, B. Polischuk, W. Haerer, "Digital breast tomosynthesis using an amorphous selenium flat panel detector," *Proc. SPIE* **5745**, (2005).
- 4 E.D. Pisano, C. Gatsonis, E. Hendrick, M. Yaffe, J.K. Baum, S. Acharyya, E.F. Conant, L.L. Fajardo, L. Bassett, C. D'Orsi, "Diagnostic performance of digital versus film mammography for breast-cancer screening," *New England Journal of Medicine* **353**, 1773-1783 (2005).
- 5 E.D. Pisano, E.B. Cole, B.M. Hemminger, M.J. Yaffe, S.R. Aylward, A.D. Maidment, R.E. Johnston, M.B. Williams, L.T. Niklason, E.F. Conant, "Image Processing Algorithms for Digital Mammography: A Pictorial Essay1," *Radiographics* **20**, 1479-1491 (2000).
- 6 F. Shtern, "Digital mammography and related technologies: a perspective from the National Cancer Institute," *Radiology* **183**, 629-630 (1992).
- 7 N. Howlader, A. Noone, M. Krapcho, N. Neyman, R. Aminou, W. Waldron, S. Altekruse, C. Kosary, J. Ruhl, Z. Tatalovich, "SEER Cancer Statistics Review, 1975-2008, National Cancer Institute. Bethesda, MD," SEER website2011).
- 8 S.M. Moss, H. Cuckle, A. Evans, L. Johns, M. Waller, L. Bobrow, "Effect of mammographic screening from age 40 years on breast cancer mortality at 10 years' follow-up: a randomised controlled trial," *Lancet* **368**, 2053-2060 (2006).
- 9 L. Nystrom, I. Andersson, N. Bjurstam, J. Frisell, B. Nordenskjold, L.E. Rutqvist, "Long-term effects of mammography screening: updated overview of the Swedish randomised trials," *Lancet* **359**, 909-918 (2002).
- 10 J.G. Elmore, M.B. Barton, V.M. Moceris, S. Polk, P.J. Arena, S.W. Fletcher, "Ten-year risk of false positive screening mammograms and clinical breast examinations," *New England Journal of Medicine* **338**, 1089-1096 (1998).
- 11 T. Wu, R.H. Moore, E.A. Rafferty, D.B. Kopans, "A comparison of reconstruction algorithms for breast tomosynthesis," *Med Phys* **31**, 2636 (2004).
- 12 I. Andersson, D.M. Ikeda, S. Zackrisson, M. Ruschin, T. Svahn, P. Timberg, A. Tingberg, "Breast tomosynthesis and digital mammography: a comparison of breast cancer visibility and BIRADS classification in a population of cancers with subtle mammographic findings," *European radiology* **18**, 2817-2825 (2008).
- 13 S.P. Poplack, T.D. Tosteson, C.A. Kogel, H.M. Nagy, "Digital breast tomosynthesis: initial experience in 98 women with abnormal digital screening mammography," *AJR. American journal of roentgenology* **189**, 616-623 (2007).

- 14 A.P. Smith, L. Niklason, B. Ren, T. Wu, C. Ruth, Z. Jing, "Lesion visibility in low dose tomosynthesis," in *Digital Mammography* (Springer, 2006), pp. 160-166.
- 15 B. Ren, C. Ruth, T. Wu, Y. Zhang, A. Smith, L. Niklason, C. Williams, E. Ingall, B. Polischuk, Z. Jing, "A new generation FFDM/tomosynthesis fusion system with selenium detector," *Proc. SPIE* **7622**, (2010).
- 16 X. Gong, S.J. Glick, B. Liu, A.A. Vedula, S. Thacker, "A computer simulation study comparing lesion detection accuracy with digital mammography, breast tomosynthesis, and cone-beam CT breast imaging," *Med Phys* **33**, 1041-1052 (2006).
- 17 R.J. Acciavatti, A.D. Maidment, "Optimization of continuous tube motion and step-and-shoot motion in digital breast tomosynthesis systems with patient motion," *Proc. SPIE* **8313**, (2012).
- 18 E.A. Rafferty, J.M. Park, L.E. Philpotts, S.P. Poplack, J.H. Sumkin, E.F. Halpern, L.T. Niklason, "Assessing radiologist performance using combined digital mammography and breast tomosynthesis compared with digital mammography alone: results of a multicenter, multireader trial," *Radiology* **266**, 104-113 (2013).
- 19 M. Michell, A. Iqbal, R. Wasan, D. Evans, C. Peacock, C. Lawinski, A. Douiri, R. Wilson, P. Whelehan, "A comparison of the accuracy of film-screen mammography, full-field digital mammography, and digital breast tomosynthesis," *Clinical radiology* **67**, 976-981 (2012).
- 20 D. Bernardi, S. Ciatto, M. Pellegrini, P. Tuttobene, C. Fanto, M. Valentini, S.D. Michele, P. Peterlongo, N. Houssami, "Prospective study of breast tomosynthesis as a triage to assessment in screening," *Breast cancer research and treatment* **133**, 267-271 (2012).
- 21 J.T. Bushberg, J.M. Boone, *The essential physics of medical imaging*. (Lippincott Williams & Wilkins, 2011).
- 22 V. Corsetti, N. Houssami, M. Ghirardi, A. Ferrari, M. Speziani, S. Bellarosa, G. Remida, C. Gasparotti, E. Galligioni, S. Ciatto, "Evidence of the effect of adjunct ultrasound screening in women with mammography-negative dense breasts: Interval breast cancers at 1year follow-up," *European Journal of Cancer* **47**, 1021-1026 (2011).
- 23 R.M. Mann, C.E. Loo, T. Wobbes, P. Bult, J.O. Barentsz, K.G. Gilhuijs, C. Boetes, "The impact of preoperative breast MRI on the re-excision rate in invasive lobular carcinoma of the breast," *Breast cancer research and treatment* **119**, 415-422 (2010).
- 24 N. Peters, S. Van Esser, M. van den Bosch, R. Storm, P. Plaisier, T. van Dalen, S. Diepstraten, T. Weits, P. Westenend, G. Stapper, "Preoperative MRI and surgical management in patients with nonpalpable breast cancer: the MONET–randomised controlled trial," *European Journal of Cancer* **47**, 879-886 (2011).
- 25 L.J. Solin, "Counterintuitive: pre-operative breast MRI (magnetic resonance imaging) is not recommended for all patients with newly diagnosed breast cancer," *The Breast* **19**, 7-9 (2010).

- 26 D.J. Brenner, E.J. Hall, "Computed tomography—an increasing source of radiation exposure," *New England Journal of Medicine* **357**, 2277-2284 (2007).
- 27 J.J. Gisvold, D.F. Reese, P.R. Karsell, "Computed tomographic mammography (CTM)," *American Journal of Roentgenology* **133**, 1143-1149 (1979).
- 28 J.M. Boone, T.R. Nelson, K.K. Lindfors, J.A. Seibert, "Dedicated Breast CT: Radiation Dose and Image Quality Evaluation," *Radiology* **221**, 657-667 (2001).
- 29 B. Chen, R. Ning, "Cone-beam volume CT breast imaging: Feasibility study," *Med Phys* **29**, 755 (2002).
- 30 M.P. Tornai, R.L. McKinley, C.N. Bryzmialkiewicz, P. Madhav, S.J. Cutler, D.J. Crotty, J.E. Bowsher, E. Samei, C.E. Floyd, "Design and development of a fully 3 D dedicated X-ray computed mammotomography system," *Proc. SPIE* **5745**, (2005).
- 31 A.L. Kwan, J.M. Boone, K. Yang, S.-Y. Huang, "Evaluation of the spatial resolution characteristics of a cone-beam breast CT scanner," *Med Phys* **34**, 275 (2007).
- 32 N. Oberhofer, A. Fracchetti, E. Nassivera, A. Valentini, E. Moroder, "Comparison of two novel FFDM systems with different a-se detector technology: physical characterization and phantom contrast detail evaluation in clinical conditions," in *Digital Mammography* (Springer, 2010), pp. 459-466.
- 33 K.K. LINDFORS, J.M. BOONE, T.R. NELSON, K. YANG, A.L. KWAN, D.F. MILLER, "Dedicated Breast CT: Initial Clinical Experience," *Radiology* **246**, 725-733 (2008).

CHAPTER 5: CARBON NANOTUBE BASED X-RAY SOURCES

5.1 Overview

Carbon nanotube (CNT) based X-ray sources utilize field emission instead of thermionic emission which is used in most X-ray sources. The unique design of CNT sources give them some advantages over thermionic sources. There are three main benefits of CNT based X-ray sources which give them an advantage over conventional thermionic X-ray sources; (1) near instantaneous turn on time, (2) compact design, (3) flexibility in cathode shape. Current applications of CNT based X-ray sources utilize one or more of these advantages in order to improve upon current X-ray systems. Some of the current applications of CNT based X-ray sources include: micro-computed tomography (micro-CT), micro-beam radiation therapy (MRT), chest tomosynthesis, computed tomography (CT), and digital breast tomosynthesis (DBT).

5.2 Field Emission from CNTs Versus Thermionic Emission

Medical X-ray tubes produce X-ray radiation by extracting electrons from a cathode, accelerating the electrons towards an anode and bombarding the anode with electrons. The most common method of electron extraction in current X-ray tubes is thermionic emission. Another less used method of electron extraction is field emission. Thermionic emission is the process of heating up a material (a metal cathode in the case of X-ray production) in a vacuum (less than 1×10^{-6} torr) until the kinetic energy of the "free" floating electrons in the metal is greater than the work function of the metal. At this point, electrons will cross the fermi-barrier at a current density equivalent to the following equation:

Equation 11:

$$J = (1 - r)A_o T^2 \exp\left(\frac{-\phi}{kT}\right)$$

Where A_0 approximately equals $1.2 \times 10^6 \text{ Am}^{-2}\text{K}^{-2}$, k = Boltzmann's constant, ϕ equals the work function of the cathode, and r is the mean electron reflection coefficient. Increasing the temperature, T , increases the emission current density. Temperature is increased by increasing the kinetic energy of the electrons. Typical cathode filaments are made of tungsten with a small amount of added thorium, and are operated at around 10V. Thorium is used to increase filament lifetime and current density. For a typical tungsten filament the work function is approximately 4.5 eV this decreases to 2.6 eV in a thoriated tungsten filament. Current densities in excess of 1000 mA/cm^2 can be obtained using a thoriated tungsten filament.⁶⁰ However, actual current densities are space charge limited as defined by Child's Law:

Equation 12:

$$J = K \frac{V_d^{\left(\frac{3}{2}\right)}}{d^2}$$

Where K is a constant approximately equal to $0.002334 \text{ mA/V}^{-3/2}$ for an electron, V_d is the potential difference between the anode and cathode, and d is the distance in cm between the anode and cathode.⁶¹ For higher potential differences the space charge limitation is negligible, but for the lower end of the diagnostic imaging range this can become a problem. Using a gap distance of 3.5 cm (design value of the s-DBT tube) and an anode potential of 25 kV the actual current density cannot exceed 753 mA/cm^2 .

Field emission was first derived in 1928 by Fowler and Nordheim.⁶² Instead of emitting electrons by increasing the kinetic energy of the electrons, field emission emits electrons by application of an electrostatic field. Application of a strong electric field lowers the work function of the material. If the work function is sufficiently lowered then the electrons will have enough energy to tunnel through the fermi-barrier. These strong electric fields are only feasible due to the field enhancement factor, Y . In a parallel-plate geometry, the electric field between the two plates is given as:

Equation 13:

$$F = V/d$$

Where F is the electric field, V is the applied voltage, and d is the gap distance between the two plates. If there is a high aspect ratio object on one plate then the electric field at that point is enhanced by:

Equation 14:

$$F_e = YF$$

Where F_e is the enhanced field. From this it can be seen that objects with high field enhancement factors will have higher electric fields at their apex. As described by Fowler et al. the current density produced from field emission is as follows:

Equation 15:

$$J = \frac{aF_e^2}{\phi} e^{\frac{-b\phi^{3/2}}{F_e}}$$

Where J is the current density in A/cm^2 , "a" and "b" are constants with values $1.54 \times 10^{-6} A eV V^{-2}$ and $6.83 \times 10^7 eV^{3/2} V cm^{-1}$, respectively, ϕ is the work function of the material, and F_e is the enhanced field calculated from **Equation 14**.⁶²

Carbon nanotubes (CNT) have a very high field enhancement factor due to their large aspect ratio. Due to this and their high mechanical and chemical stability, CNTs are ideal candidates for field emitters.⁶³ For operation of a stationary digital breast tomosynthesis (s-DBT) system, which utilizes 31 CNT based field emission sources, a cathode current of 43 mA is typically used. The CNT deposition area of these cathodes are 2.5 mm x 13 mm or .325 cm^2 . This gives a current density of 132.3 mA/cm^2 for typical operation of the s-DBT system. This should not be taken as an absolute number for current density of a CNT based field emission cathode. A few different variables contribute to the current density of a cathode including: gap distance between the cathode and gate electrode (or anode in diode mode), potential voltage

between the two electrodes. Assuming the current density could double if the system was pushed to its highest potential, that would give a current density of 264.6 mA/cm^2 .

Comparing the two types of emission shows that both require tunneling through the fermi-barrier. In thermionic emission, energy is added to the electrons in the form of heat to cross the barrier, while in field emission the energy required to cross the barrier is lowered by an electric field. Thermionic emission yields current densities on the order of 1 A/cm^2 while field emission from CNTs yields current densities on the order of 100s of mA/cm^2 . Thermionic emission is affected by space charge but it has negligible effects except at low anode potential. Thermionic emission requires temperatures in the 1000 K range while field emission occurs at room temperature. Both techniques require a high vacuum enclosure.

5.3 CNT Based X-ray Sources

A carbon nanotube based field emission X-ray source works in a triode design (it will also work in diode mode but is not as stable or useful).⁶⁴ The entire tube is under a steady state vacuum around 10^{-10} Torr. A schematic of a typical CNT based X-ray source can be found in **Figure 12**.

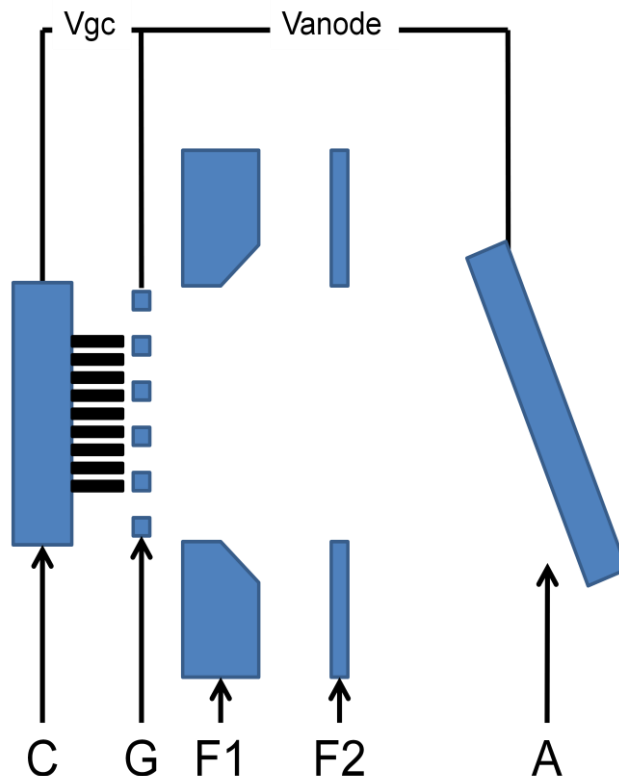


Figure 12: Schematic of a typical CNT based X-ray source. Where "C" is the cathode structure, "G" is the gate electrode, "F1" and "F2" are focusing electrodes, "A" is the anode, " V_{gc} " is applied gate cathode voltage, and " V_{anode} " is the applied anode voltage.

The main parts of the X-ray tube are the cathode (C), gate electrode (G), and the anode (A). The two focusing electrodes (F1 and F2) are secondary structures that can change the shape of the focal spot but are not necessary for operation. CNTs are deposited on the cathode by an electrophoretic deposition method developed in our lab.⁶⁵ Approximately 275 microns (in an s-DBT cathode) above the cathode is the gate electrode. The gate electrode consists of a mesh of tungsten bars 0.05 mm in width separated by a 0.2 mm distance (in this design). The gate is grounded in the s-DBT design. The first focusing structure (F1) is 0.762 mm above the gate and the second focusing structure (F2) is 1.178 mm above that. The anode is located 35 mm above the cathode and is made of tungsten attached to a copper backing. It is at an anode angle of 16° . For operation of the tube, a positive high potential difference near 30 kVp is applied between the gate electrode and the anode. This voltage determines the maximum energy of the X-ray spectrum (with the addition of the gate-cathode voltage). If there are small

irregularities on the focusing structure or gate electrode a high anode kVp could produce a dark current. This effect is more noticeable around 80 kVp. Assuming perfect interior structures in this case, the anode voltage produces little to no X-rays. If in a diode design, the potential difference would be applied between cathode and anode and that would produce a current. In the triode case, a smaller negative potential on the order of -1400V must be applied between the cathode and gate electrode. This voltage will start field emission on the cathodes and create a tube current on the order of 40mA (for a -1400V potential in the s-DBT design). As electrons are accelerated to the anode, some of these will bombard the gate structure and focusing structures. This produces a smaller current on the anode than was initially produced from the cathode. Typical transmission rates are around 60%. A diode setup with no focusing structures would produce 100% transmission rates but would lose the ability of instantaneous on and off (due to ramp up time of anode power supply) and would produce larger focal spots. Once the electrons bombard the anode bremsstrahlung and characteristic X-rays are produced in all directions. Of all the electrons bombarding the anode only about 0.5% of them produce X-ray radiation. The rest of the energy is converted into heat. Heating of the anode is a severe problem and can cause the anode to melt and then the entire tube to fail. Careful considerations of anode heat load must be taken into account when designing or operating any X-ray source.

Many factors affect the X-ray tube current of a CNT based field emission X-ray source. A major factor is the density of CNTs across the cathode. More densely packed CNTs can produce a higher current density.⁶⁴ The length of the CNTs also have an effect on current. Longer CNTs can more easily align with the electric field and thus produce a higher current. Beyond the CNTs, another factor affecting tube current is the applied electric field to the cathode. In general a larger electric field will produce a larger tube current.⁶⁴ The spacing of the gate mesh also affects the tube current. Larger spacing will increase the transmission rate but will require a larger applied voltage to get the same electric field, this could add cost to the

system or might not be feasible due to arcing distances. The transmission rate is also affected by the focusing voltages. Simulations and tests must be conducted to find the optimal point for transmission rate and focal spot size.^{20, 66}

The tube lifetime depends mostly on the tube operation. Overtime, the CNTs will vaporize. As this occurs the current will begin to drop for the same applied voltage and the quality of the vacuum will degrade. If the tube is operated at very high current and anode voltage then the inherent degradation of the CNTs will be accelerated. The quality of the CNT cathodes also affects tube lifetime. If there are large variations in the CNTs distance to the gate electrode, then different electric fields will be applied to different CNTs. The ones closer to the gate electrode will degrade faster than the ones farther away. This will cause a decrease in maximum tube current over time. A poor vacuum will also cause the CNT X-ray source to degrade. Poor vacuums lead to arcing of the cathodes and anodes. Both can be fatal to the tube. When properly designed, created, and maintained; CNT X-ray sources have shown lifetimes of more than three years in a busy hospital.¹³

CNT field emission X-ray sources have some shortcomings and some strengths when compared to thermionic sources. If properly designed a CNT X-ray source can overcome its shortcomings and be a useful tool in X-ray imaging.

5.4 Applications of CNT Based X-ray Sources

There are three main benefits of CNT based X-ray sources which give them an advantage over conventional thermionic X-ray sources; (1) near instantaneous turn on time, (2) compact design, (3) flexibility in cathode shape. Current applications of CNT based X-ray sources utilize one or more of these advantages in order to improve upon current X-ray systems. Some of the current applications of CNT based X-ray sources include: micro-CT, MRT, chest tomosynthesis, CT, and DBT. The following sub-sections will outline these systems and some of the results from research conducted using them.

5.4.1 Micro-Computed Tomography

A micro-CT system is useful for imaging of small animals in pre-clinical studies.^{67, 68}

Imaging of mice is difficult due to their very short respiratory and cardiac cycles. Gating to the periodic cycles is not possible in thermionic X-ray sources due to their slow turn on times. A CNT based X-ray source has extremely fast turn on and off times and is therefore ideally suited for use in micro-CT. An image of the CNT based micro-CT system can be found in **Figure 13**.



Figure 13: Image of the final design of the CNT based micro-CT system, Charybdis.

Lee et al. demonstrated respiratory gating of free breathing mice using the CNT micro-CT system.⁶⁹ Twelve mice were imaged during peak inspiration and end exhalation.

Respiration was monitored using a contact sensor pad which was placed under the abdomen of the mice. The near instantaneous turn on time of the CNT source allowed for consistent gating to the respiratory cycle. **Figure 14** shows a 3D visualization of the reconstructed lungs from a mouse image on the micro-CT. The average acquisition time for each phase of the respiratory cycle was 13.4 minutes with an average respiration rate of 96.2 breaths/min. It was concluded

that the CNT based micro-CT is capable of producing high resolution images which are physiologically gated to the respiratory cycle.⁶⁹



Figure 14: A 3D visualization of the lungs of a mouse imaged on the CNT based micro-CT system.

Cao et al. utilized the CNT micro-CT to image mice using dual gating to the respiratory and cardiac cycles.⁷⁰ Ten free breathing mice were imaged. The CT datasets were obtained a 15 ms temporal resolution and a 6.2 cycles/mm spatial resolution. The average total imaging time was 44 minutes with an average respiration rate of 101 breaths/min and an average heart rate of 418 beats per minute. **Figure 15** (Left) shows a reconstruction of one of the mice. In the image the four chambers of the heart are visible due to the high gating precision only possible with the CNT based micro-CT. It was concluded that the CNT based system is capable of producing high resolution CT datasets of free breathing mice that are gated to both the respiratory and cardiac cycle.⁷⁰



Figure 15: Left - Reconstruction of a micro-CT dataset of a mouse which was gated to both the cardiac and respiratory cycle. All four chambers of the heart are visible. **Right** - Reconstruction of a micro-CT dataset of a mouse pup using the non-contact sensor.

A physical contact sensor is difficult or impossible to use on mice with severe deterioration of rib bones or mouse pups which do not create enough force during respiration to trigger the sensor. For these reasons, Burke et al. replaced the contact sensor pad used in previous studies for a fiber optic contactless sensor.⁷¹ Four adult mice were imaged using the contact and contactless sensor. Similar image quality was found for both sensors but the contactless sensor created a artifact where the fiber optic cable was located. Eleven mouse pups and four mice with congenital diaphragmatic hernias were imaged with the contactless sensor only. These types of mice cannot be imaged with a contact sensor. **Figure 15** (Right) shows a reconstruction of one of the mouse pups. It was concluded that the contactless sensor allowed for gated imaging of certain mice types that would otherwise not have been achievable. For cases without a need for a contactless sensor, the contact sensor is more preferred due to the artifact created from the fiber optic cable.⁷¹

5.4.2 Micro-Beam Radiation Therapy

Traditional radiation therapy (RT) techniques involve the use of ionizing radiation to irradiate cancerous lesions in the body. A large concern of RT is the damage done to the normal tissue surrounding the cancer which inevitable will also be irradiate and can therefore be damaged.⁷² Even though new techniques allow for substantial reduction in dose to normal tissue, no method exists which results in zero damage to normal tissue while still irradiating the cancer.⁷³ Many decades ago a method for tissue sparing RT, MRT, was developed using a synchrotron as the source of radiation. MRT uses alternating "peaks" of high dose radiation (approximately 100 μm in diameter) with "valleys" of non-primary low dose radiation. The "peak" to "valley" ratio (PVDR) is kept extremely high at greater than ten.^{74, 75} This method of RT has been shown to spare normal tissue in a variety of animal models.⁷⁶⁻⁷⁸ Large strides in the advancement of this technology have not been achieved due to the fact that synchrotron is needed for the method to work properly. Synchrotrons are very large and require a significant financial investment which is not feasible for more than a few locations in the world. A small compact system could advance the technology to the clinic one day. However conventional X-ray sources are not suited for MRT. Megavoltage tubes used in conventional RT would produce scattered radiation and secondary charge particles in tissue which would drop the PVDR too low to be beneficial.⁷⁹ The large dose needed is not feasible using an orthovoltage tube in the time scale that RT procedures are performed in. Micro-focus tubes would produce the correct sized focal spot but are not capable of producing the dose rate,⁸⁰ while a conventional tube with a larger focal spot would require a collimation system which would reduce the dose rate to a unreasonable level.⁸¹ Using a CNT based X-ray source with a long narrow cathode structure and a micro-beam collimator Hadsell et al. was able to create the world's first desktop MRT system.⁷⁹ An image of the prototype system can be found in **Figure 16**.

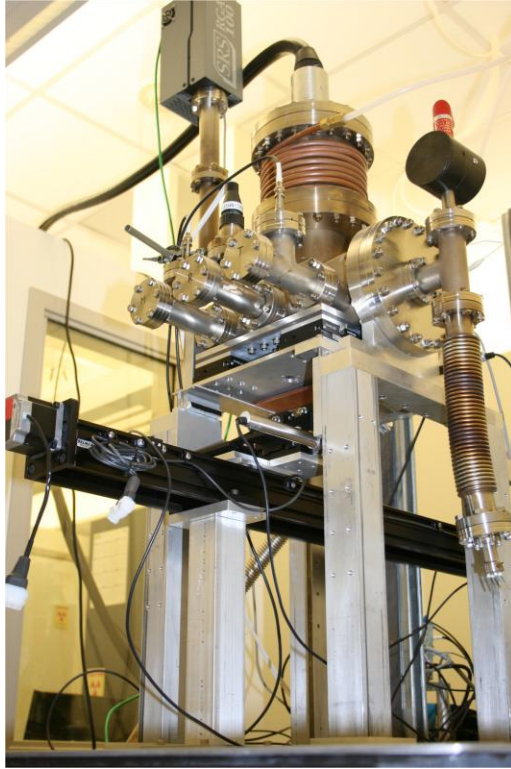


Figure 16: Image of the desktop CNT based MRT system.

Hadsell et al. reported that the system could produce a 300 μm wide line of radiation. An instantaneous dose rate of 2 Gy/s was measured with a PVDR of more than 17 when a 1.4 mm distance between microbeams was used. They demonstrated that it could produce MRT dose distribution in phantoms and live mice. A histological stain of a mouse brain with DNA damage produced from the CNT based MRT system can be found in **Figure 17**.

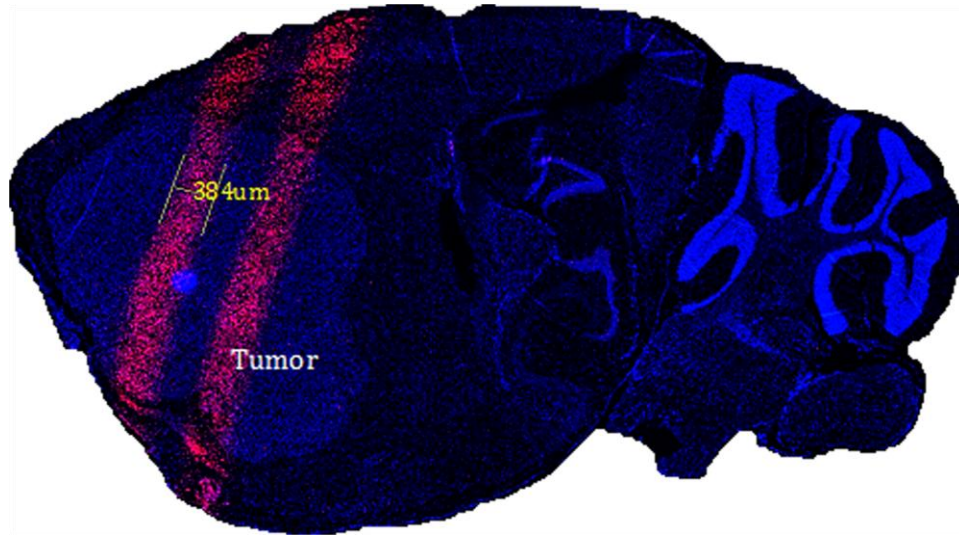


Figure 17: Histological image of microbeam DNA damage in a mouse brain with human brain tumor. Cell staining was done with γ -H2AX labeling four hours after radiation.

5.4.3 Chest Tomosynthesis

Lung cancer is the leading cause of cancer related deaths in developed countries with more than 1.3 million deaths per year.⁸² When the disease is diagnosed at an early stage the 5-year survival rate is greater than 70%.⁸³ However, the overall (for all stages at diagnosis) 5-year survival rate is approximately 10% for Europeans.⁸⁴ Early detection is the best way to survive the disease. Chest CT has been shown to be more effective at diagnosing the disease at an early stage compared to planar chest imaging.⁸⁵ However, the high cost and dose from CT means it is not feasible for screening purposes on a large scale. More recently, digital tomosynthesis has been used for diagnosing lung cancer. Digital chest tomosynthesis uses a series of projection images distributed over a small angular span to reconstruction a pseudo 3D representation of the chest.^{86, 87} Chest tomosynthesis has been shown to be more effective than 2D radiography at identifying nodules but at a significantly lower dose compared to CT.⁸⁸⁻⁹⁰ Current chest tomosynthesis systems utilize a single thermionic X-ray source which is rotated over the angular span.⁸⁶ This source motion reduces the spatial resolution of the system and increases the total acquisition time which can lead to patient motion.⁹¹ A stationary approach with multiple X-ray sources would allow for fast acquisitions with no lose in spatial resolution. A

conventional thermionic X-ray source is large and cannot be packed closely together to allow for a stationary system. Shan et al. have developed a stationary chest tomosynthesis system using an array of CNT based X-ray sources.⁹¹ **Figure 18 (Left)** shows an image of the prototype system. They reported that the system is capable of producing a full set of tomosynthesis images with zero motion blur. Although the current tube was designed for security purposes and therefore is limited on anode voltage and angular span, a future tube could be designed and implemented with the correct angular span and anode voltage.⁹¹

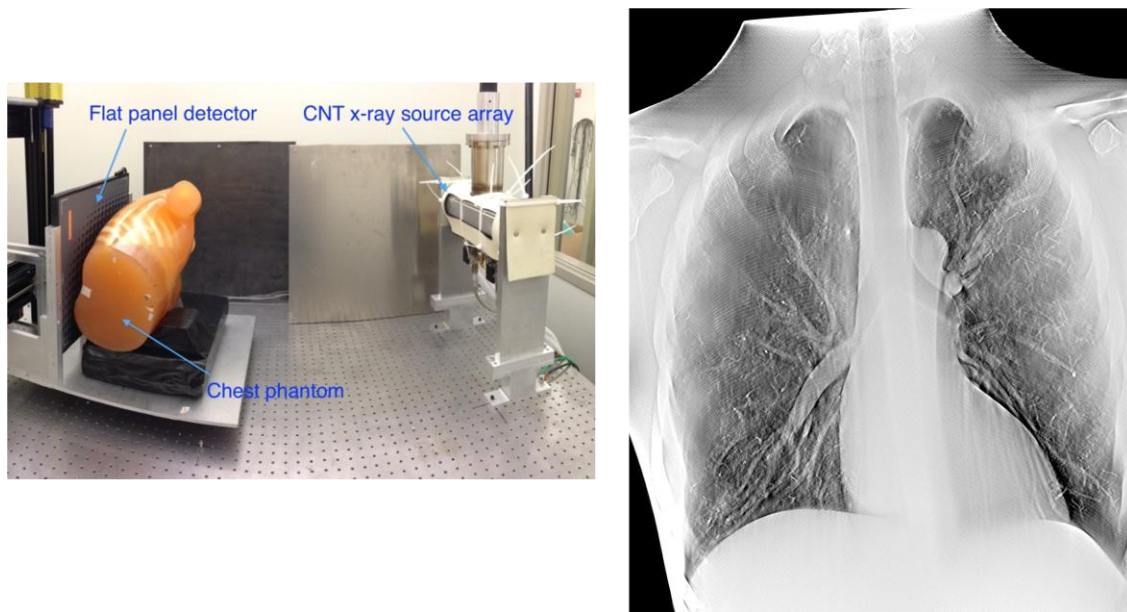


Figure 18: Left - Image of the prototype stationary chest tomosynthesis system. **Right** - Reconstruction slice of a chest phantom using the system.

5.4.4 Computed Tomography

Computed tomography is useful in many X-ray based imaging applications.^{92, 93} A conventional CT system uses a single thermionic X-ray source which is mounted on a large gantry and is rotated around a fixed point. Not only does this rotation add mechanical instability, but it also adds a large amount of size and weight to the system. Previous research has gone into using multiple thermionic X-ray sources to produce the CT dataset.^{94, 95} These systems suffer from under sampling of the Fourier domain due to the large distance between X-ray sources. Conventional thermionic X-ray sources are large and cannot be packed close together.

A CNT X-ray source can be manufactured in a compact design which allows for close packing between sources. Gonzalez et al. constructed a rectangular stationary CT for imaging of luggage.⁹⁶ The system utilizes two banks of CNT X-ray sources which produce fan beams. Luggage is sent through the system using a conveyor belt. Reconstructions are completed using an iterative algorithm on a graphics processing unit (GPU). The GPU allows for fast iterative reconstruction which is necessary for busy luggage check stations. They concluded that the non-circular setup could open the door to more efficient task based CT systems which could be used in medical imaging as well as security.⁹⁶

5.4.5 Digital Breast Tomosynthesis

Conventional DBT systems utilize a single rotating X-ray source.^{11, 97, 98} Rotation of the source during image acquisition leads to decreased spatial resolution and therefore, decreased MC visibility.^{46, 99} A stationary DBT (s-DBT) system has been created using a linear array of CNT based X-ray sources.¹³ An image of the system (**Left**) and a reconstruction slice of a breast phantom using the system (**Right**) can be found in **Figure 19**.

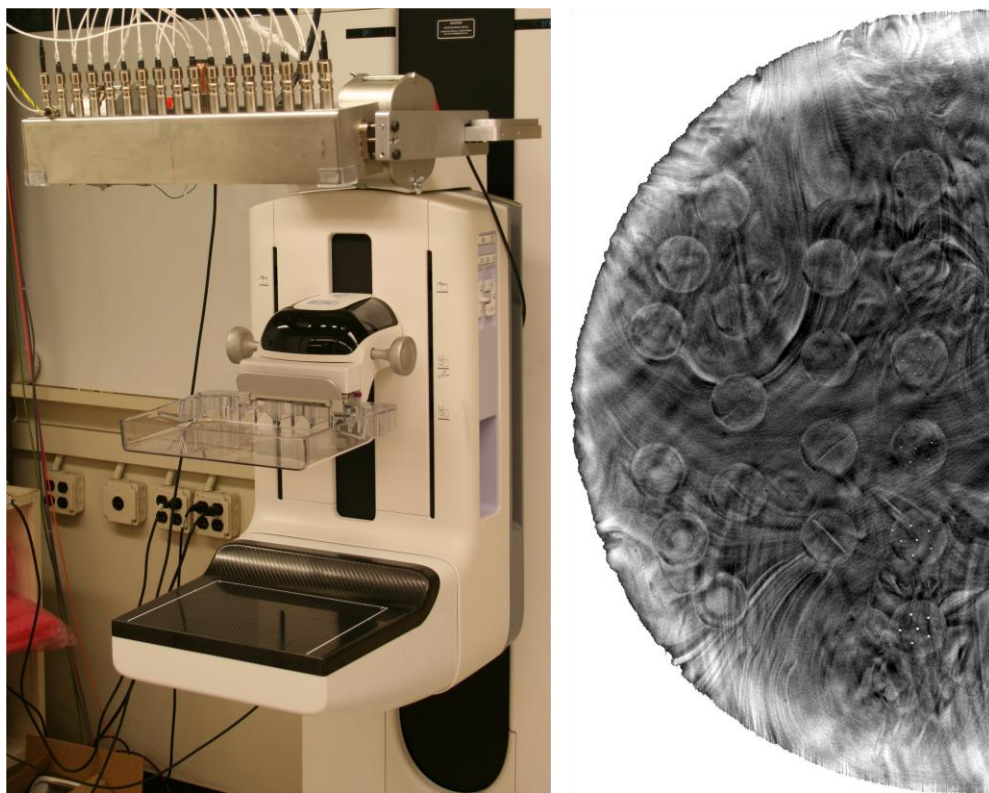


Figure 19: **Left** - Image of the prototype s-DBT system. **Right** - Reconstruction slice of a breast phantom using the s-DBT system.

REFERENCES

- 1 E. Lassner, W.-D. Schubert, *Tungsten: properties, chemistry, technology of the elements, alloys, and chemical compounds*. (Springer, 1999).
- 2 C. Child, "Discharge from hot CaO," *Physical Review (Series I)* **32**, 492 (1911).
- 3 R.H. Fowler, L. Nordheim, "Electron emission in intense electric fields," *Proceedings of the Royal Society of London. Series A, Containing Papers of a Mathematical and Physical Character* **119**, 173-181 (1928).
- 4 W. Zhu, *Vacuum microelectronics*. (Wiley. com, 2004).
- 5 Y. Saito, *Carbon Nanotube and Related Field Emitters: Fundamentals and Applications*. (Wiley. com, 2010).
- 6 S.J. Oh, J. Zhang, Y. Cheng, H. Shimoda, O. Zhou, "Liquid-phase fabrication of patterned carbon nanotube field emission cathodes," *Applied Physics Letters* **84**, 3738 (2004).
- 7 Z. Liu, G. Yang, Y.Z. Lee, D. Bordelon, J. Lu, O. Zhou, "Carbon nanotube based microfocus field emission x-ray source for microcomputed tomography," *Applied Physics Letters* **89**, 103111-103111-103113 (2006).
- 8 F. Sprenger, X. Calderon-Colon, E. Gidcumb, J. Lu, X. Qian, D. Spronk, A. Tucker, G. Yang, O. Zhou, "Stationary digital breast tomosynthesis with distributed field emission x-ray tube," *Proc. SPIE* **7961**, (2011).
- 9 X. Qian, A. Tucker, E. Gidcumb, J. Shan, G. Yang, X. Calderon-Colon, S. Sultana, J. Lu, O. Zhou, D. Spronk, F. Sprenger, Y. Zhang, D. Kennedy, T. Farbizio, Z. Jing, "High resolution stationary digital breast tomosynthesis using distributed carbon nanotube x-ray source array," *Med Phys* **39**, 2090 (2012).
- 10 M.J. Paulus, S.S. Gleason, S.J. Kennel, P.R. Hunsicker, D.K. Johnson, "High resolution X-ray computed tomography: an emerging tool for small animal cancer research," *Neoplasia (New York, NY)* **2**, 62 (2000).
- 11 E.L. Ritman, "Micro-computed tomography-current status and developments," *Annu. Rev. Biomed. Eng.* **6**, 185-208 (2004).
- 12 Y.Z. Lee, L.M. Burk, K.-h. Wang, G. Cao, J. Volmer, J. Lu, O. Zhou, "Prospective respiratory gated carbon nanotube micro computed tomography," *Academic radiology* **18**, 588-593 (2011).
- 13 G. Cao, L.M. Burk, Y.Z. Lee, X. Calderon-Colon, S. Sultana, J. Lu, O. Zhou, "Prospective-gated cardiac micro-CT imaging of free-breathing mice using carbon nanotube field emission x-ray," *Med Phys* **37**, 5306 (2010).
- 14 L.M. Burk, Y.Z. Lee, J.M. Wait, J. Lu, O.Z. Zhou, "Non-contact respiration monitoring for in-vivo murine micro computed tomography: characterization and imaging applications," *Physics in Medicine and Biology* **57**, 5749 (2012).

- 15 E.J. Hall, A.J. Giaccia, *Radiobiology for the Radiologist*. (Wolters Kluwer Health, 2006).
- 16 J. Van Dyk, *The modern technology of radiation oncology*. (Medical Physics Publ., 1999).
- 17 M. De Felici, R. Felici, M.S. del Rio, C. Ferrero, T. Bacarian, F. Dilmanian, "Dose distribution from x-ray microbeam arrays applied to radiation therapy: An EGS4 Monte Carlo study," *Med Phys* **32**, 2455 (2005).
- 18 D. Slatkin, P. Spanne, F. Dilmanian, M. Sandborg, "Microbeam radiation therapy," *Med Phys* **19**, 1395 (1992).
- 19 F. Dilmanian, G. Morris, G. Le Duc, X. Huang, B. Ren, T. Bacarian, J. Allen, J. Kalef-Ezra, I. Orion, E. Rosen, "Response of avian embryonic brain to spatially segmented x-ray microbeams," *Cellular and molecular biology (Noisy-le-Grand, France)* **47**, 485 (2001).
- 20 J.A. Laissue, H. Blattmann, M. Di Michiel, D.N. Slatkin, N. Lyubimova, R. Guzman, W. Zimmermann, S. Birrer, T. Bley, P. Kircher, "Weanling piglet cerebellum: a surrogate for tolerance to MRT (microbeam radiation therapy) in pediatric neuro-oncology," *International Symposium on Optical Science and Technology*, (2001).
- 21 J.A. Laissue, N. Lyubimova, H.-P. Wagner, D.W. Archer, D.N. Slatkin, M. Di Michiel, C. Nemoz, M. Renier, E. Brauer, P.O. Spanne, "Microbeam radiation therapy," *Proc. SPIE* **3770**, (1999).
- 22 M. Hadsell, J. Zhang, P. Laganis, F. Sprenger, J. Shan, L. Zhang, L. Burk, H. Yuan, S. Chang, J. Lu, "A first generation compact microbeam radiation therapy system based on carbon nanotube X-ray technology," *Applied physics letters* **103**, 183505 (2013).
- 23 F. Verhaegen, P. Granton, E. Tryggestad, "Small animal radiotherapy research platforms," *Physics in Medicine and Biology* **56**, R55 (2011).
- 24 K. Huang, K. Yan, T. Podder, Y. Hu, Y. Yu, "Feasibility Analysis On Converting Conventional Orthovoltage Biological Irradiator to a Micro- Beam Array for Small Animal/cell Irradiation," *Med Phys* **36**, 2514 (2009).
- 25 U. Pastorino, "Lung cancer screening," *British journal of cancer* **102**, 1681-1686 (2010).
- 26 P. Goldstraw, J. Crowley, K. Chansky, D.J. Giroux, P.A. Groome, R. Rami-Porta, P.E. Postmus, V. Rusch, L. Sobin, "The IASLC Lung Cancer Staging Project: proposals for the revision of the TNM stage groupings in the forthcoming (seventh) edition of the TNM Classification of malignant tumours," *Journal of thoracic oncology* **2**, 706-714 (2007).
- 27 A. Verdecchia, S. Francisci, H. Brenner, G. Gatta, A. Micheli, L. Mangone, I. Kunkler, "Recent cancer survival in Europe: a 2000–02 period analysis of EURO CARE-4 data," *The lancet oncology* **8**, 784-796 (2007).
- 28 M. Kaneko, K. Eguchi, H. Ohmatsu, R. Kakinuma, T. Naruke, K. Suemasu, N. Moriyama, "Peripheral lung cancer: screening and detection with low-dose spiral CT versus radiography," *Radiology* **201**, 798-802 (1996).

- 29 J.T. Dobbins III, H.P. McAdams, "Chest tomosynthesis: technical principles and clinical update," *European journal of radiology* **72**, 244-251 (2009).
- 30 A. Tingberg, "X-ray tomosynthesis: a review of its use for breast and chest imaging," *Radiation protection dosimetry* **139**, 100-107 (2010).
- 31 M. Båth, A. Svalkvist, A. von Wrangel, H. Rismyhr-Olsson, Å. Cederblad, "Effective dose to patients from chest examinations with tomosynthesis," *Radiation protection dosimetry* **139**, 153-158 (2010).
- 32 E.Y. Kim, M.J. Chung, H.Y. Lee, W.-J. Koh, H.N. Jung, K.S. Lee, "Pulmonary Mycobacterial Disease: Diagnostic Performance of Low-Dose Digital Tomosynthesis as Compared with Chest Radiography1," *Radiology* **257**, 269-277 (2010).
- 33 J. Vikgren, S. Zachrisson, A. Svalkvist, Å.A. Johnsson, M. Boijesen, A. Flinck, S. Kheddache, M. Båth, "Comparison of Chest Tomosynthesis and Chest Radiography for Detection of Pulmonary Nodules: Human Observer Study of Clinical Cases1," *Radiology* **249**, 1034-1041 (2008).
- 34 J. Shan, P. Chtcheprov, A.W. Tucker, Y.Z. Lee, X. Wang, D. Foos, M.D. Heath, J. Lu, O. Zhou, "Stationary chest tomosynthesis using a CNT x-ray source array," *SPIE Medical Imaging*, (2013).
- 35 A. Berrington de Gonzalez, M. Mahesh, K.-P. Kim, M. Bhargavan, R. Lewis, F. Mettler, C. Land, "Projected cancer risks from computed tomographic scans performed in the United States in 2007," *Archives of internal medicine* **169**, 2071 (2009).
- 36 G. Zentai, "X-ray imaging for homeland security," *International Journal of Signal and Imaging Systems Engineering* **3**, 13-20 (2010).
- 37 K. Hori, T. Fujimoto, K. Kawanishi, "Development of ultra-fast X-ray computed tomography scanner system," *Nuclear Science, IEEE Transactions on* **45**, 2089-2094 (1998).
- 38 J. Kinsey, R. Robb, E. Ritman, E. Wood, "The DSR--a high temporal resolution volumetric roentgenographic CT scanner," *Herz* **5**, 177 (1980).
- 39 B. Gonzales, D. Spronk, Y. Cheng, Z. Zhang, X. Pan, M. Beckmann, O. Zhou, J. Lu, "Rectangular computed tomography using a stationary array of CNT emitters: initial experimental results," *SPIE Medical Imaging*, (2013).
- 40 A. Maidment, M. Albert, S. Thunberg, L. Adelow, O. Blom, J. Egerstrom, M. Eklund, T. Francke, U. Jordung, T. Kristoffersson, "Evaluation of a photon-counting breast tomosynthesis imaging system," *Proc. SPIE* **5745**, (2005).
- 41 B. Ren, C. Ruth, T. Wu, Y. Zhang, A. Smith, L. Niklason, C. Williams, E. Ingall, B. Polischuk, Z. Jing, "A new generation FFDM/tomosynthesis fusion system with selenium detector," *Proc. SPIE* **7622**, (2010).

- 42 T. Wu, A. Stewart, M. Stanton, T. McCauley, W. Phillips, D.B. Kopans, R.H. Moore, J.W. Eberhard, B. Opsahl-Ong, L. Niklason, "Tomographic mammography using a limited number of low-dose cone-beam projection images," *Med Phys* **30**, 365 (2003).
- 43 D. Bernardi, S. Ciatto, M. Pellegrini, V. Anesi, S. Burlon, E. Cauli, M. Depaoli, L. Larentis, V. Malesani, L. Targa, "Application of breast tomosynthesis in screening: incremental effect on mammography acquisition and reading time," *British Journal of Radiology* **85**, e1174-e1178 (2012).
- 44 M. Michell, A. Iqbal, R. Wasan, D. Evans, C. Peacock, C. Lawinski, A. Douiri, R. Wilson, P. Whelehan, "A comparison of the accuracy of film-screen mammography, full-field digital mammography, and digital breast tomosynthesis," *Clinical radiology* **67**, 976-981 (2012).

CHAPTER 6: STATIONARY DIGITAL BREAST TOMOSYNTHESIS

6.1 Overview

Current DBT systems are limited in spatial resolution due to motion of the X-ray source during image acquisition which blurs the focal spot of the source. High spatial resolution is needed in mammography imaging in order to visualize MCs which can be less than 100 μm in diameter. We have developed a stationary digital breast tomosynthesis system which is capable of producing a full set of tomosynthesis projection images with no focal spot blurring. The first prototype system was capable of producing a full DBT dataset but needed revisions in order to be ready for human imaging. The current prototype system has been shown to have 33% better spatial resolution than the Selenia Dimensions DBT system (Hologic Inc., Bedford, MA) which is the only DBT system currently FDA approved for screening mammography. The new prototype has been designed and is ready for human imaging.

6.2 Motivation for a Stationary System

Screening mammography is the current gold standard for early detection of breast cancer.^{2,3} However, 2D mammography imaging lacks depth information, which can cause underlying and overlying tissue to obstruct the view of lesions. This leads to high false positive and false negative rates.^{4,5} Digital breast tomosynthesis (DBT) uses multiple low dose projection images distributed over an angular span to create a pseudo-3D reconstruction of the breast. This added depth information allows for otherwise obscured lesions to become visible.^{6,8,9,100} Currently only one DBT system is FDA approved for use in the United States.

Current DBT systems use a single x-ray source which is rotated over a limited angle arc. The x-ray source rotates in a continuous motion^{10,11} or using a step-and-shoot motion.¹² In both methods, the motion of the x-ray source can have an adverse effect on tomosynthesis

reconstruction quality and total imaging time.^{13, 14} The source motion results in a blurred focal spot. A blurred focal spot decreases the spatial resolution of the projection images which in turn reduces the spatial resolution of the reconstructed images. High spatial resolution is needed in mammography in order to resolve microcalcifications (MCs). MCs are important because the size and shape of them can indicate the likelihood that a particular lesion is benign or malignant. In both continuous motion and step-and-shoot DBT systems the focal spot blurring effect can be reduced by decreasing the rotation speed and increasing the acquisition time.^{14, 15} However, a long acquisition time leads to patient motion which also degrades the image quality.¹⁶ We have developed a stationary digital breast tomosynthesis (s-DBT) system which gives the acquisition speed of a continuous motion system but with no motion blur. The system utilizes an array of CNT based X-ray focal spots. This chapter outlines the s-DBT system and some of the early research completed using it.

6.3 First Prototype System

The first prototype s-DBT system consisted of a CNT based X-ray source array, a flat panel detector, and a metal–oxide–semiconductor field-effect transistor (MOSFET) based X-ray switching system. **Figure 20** shows an image of the bench top prototype system.

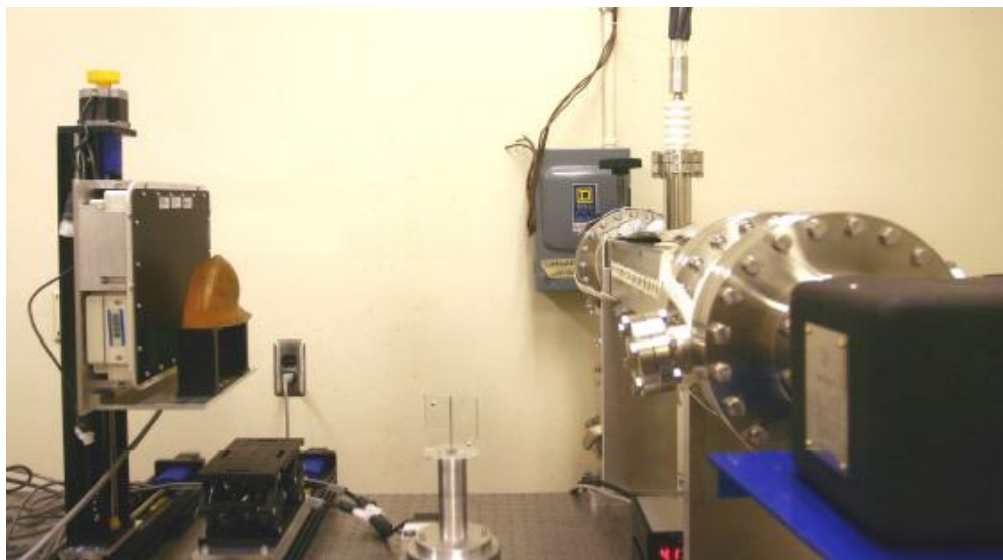


Figure 20: First prototype s-DBT system.

6.3.1 CNT Source Array

The CNT based X-ray source array utilized 25 X-ray generating focal spots in a linear design. The source was kept at an active vacuum of around $1.0\text{e-}8$ Torr using a turbo pump. The tube was not sealed to allow for maintenance on the sources when needed. The source-to-imager distance (SID) was approximately 70 cm. This SID resulted in an angular coverage of 48 degrees with a 2 degree distance between focal spots. The molybdenum anode and $30\text{ }\mu\text{m}$ window produce the X-ray spectrum found in **Figure 21**. The average projection MTF values were found to be 2.2 and 2.5 cycles/mm in the horizontal and vertical directions, respectively.¹⁷

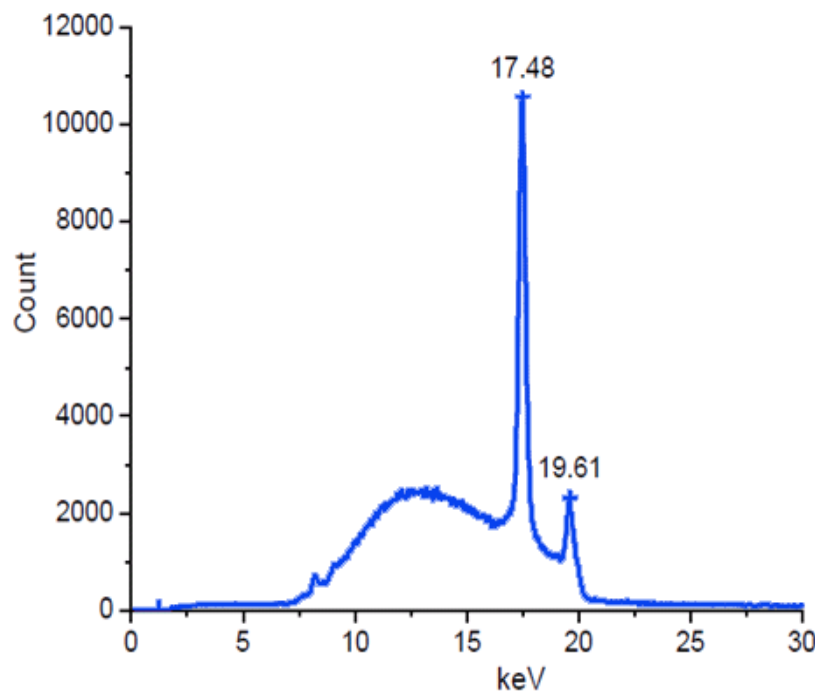


Figure 21: The X-ray spectrum of the first prototype s-DBT system. The Mo/Mo anode filter combination produces characteristic peaks at 17.48 and 19.61 keV.

6.3.2 Detector

The flat panel detector used in the system was a Paxscan 2520 manufactured by Varian Medical Systems (Salt Lake City, Utah). The detector has a $127\text{ }\mu\text{m}$ pixel size with a 0.128 s readout time. The detector MTF was measured to be 3.1 cycles/mm.¹⁷

6.3.3 Switching System

Fast acquisition times for the s-DBT system depends on the speed at which the gate-cathode voltage can be switched between cathodes. The first prototype system utilized a MOFSET based switching system. Transistor-transistor logic (TTL) signals triggered the individual MOFSETs to fire the X-ray beams in sequential order. The delay time from the TTL signal arrival to the switching of the voltage was between 35-45 ns, which was sufficiently small given the tens of milliseconds of exposure time per beam.

6.3.4 Images

Image reconstruction was completed using an iterative ordered-subset convex algorithm based on a maximum-likelihood model.¹⁰¹ **Figure 22** shows reconstruction slices of a breast phantom from the system.

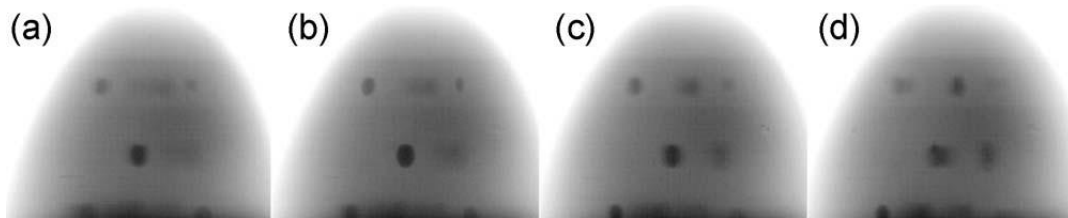


Figure 22: Reconstruction slices of a breast phantom from the first prototype s-DBT system. The slices are at the heights of (a) 6 mm, (b) 11 mm, (c) 16 mm, and (d) 21 mm.

6.4 Second Prototype System

The second prototype system consists of a CNT based X-ray source array integrated into a Selenia Dimensions DBT system (Hologic Inc., Bedford, MA) and an electronic control system (ECS). **Figure 23** shows the constructed prototype system.

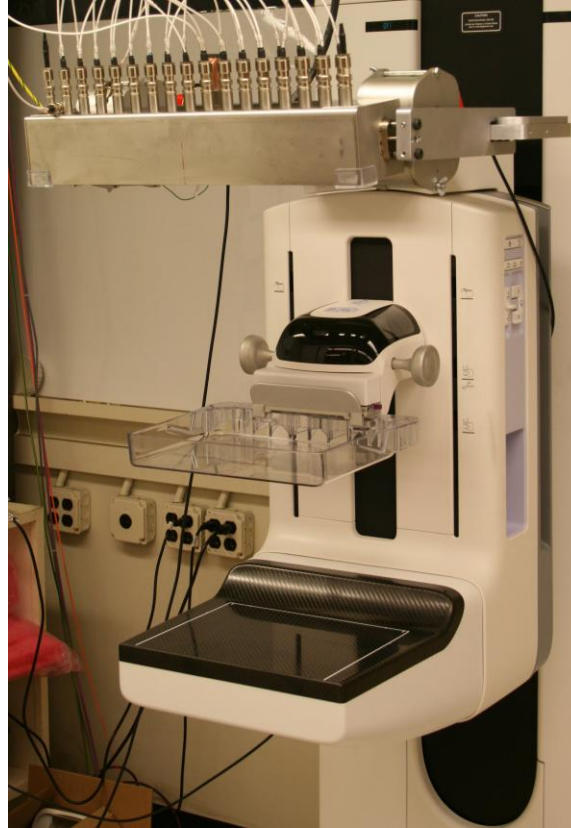


Figure 23: Image of the second prototype s-DBT system.

6.4.1 CNT Source Array

The source contains 31 X-ray generating focal spots in a linear design in a stainless steel housing. The system SID is 70 cm which gives an angular span of 30 degrees with an angular distance between focal spots of 1 degree. The anode is made of tungsten (W) with a 1 mm thick aluminum (Al) window which produces the spectrum found in **Figure 24**. The characteristic peaks of the W/Al anode filter combination are at higher energies than 40 keV and therefore do not appear in the spectra. Unlike the original prototype source, the second source is vacuum sealed and is kept at a pressure of around $1.0\text{e-}10$ when not in use by two ion pumps. This allows for greater stability and a longer lifetime.

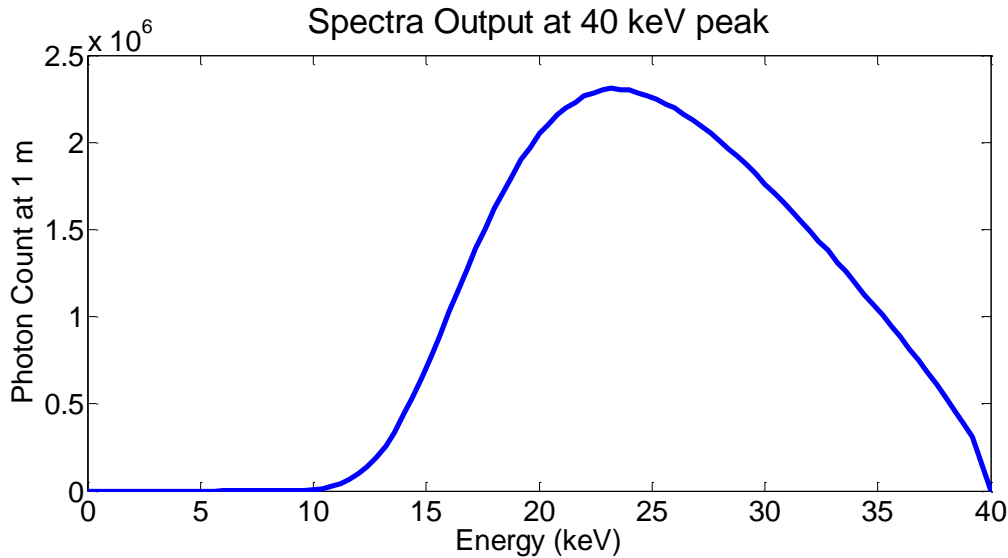


Figure 24: X-ray spectra of the second prototype s-DBT system at 40 keV peak energy. The characteristic peaks of the W/AI anode filter combination are at higher energies than 40 keV and therefore do not appear in the spectra.

The tube is designed for operation at up to 45 keV anode potential. However, typical operation does not exceed 40 keV. The cathodes were conditioned to operate at up to 43 mA of current. The average gate-cathode voltage for the 31 beams at 43 mA cathode current was 1.4 kV. The measured gate-cathode voltages for 43 mA cathode current are plotted in **Figure 25** (Above). Since the triode design of the CNT X-ray sources prevents every electron extracted from the cathode from reaching the anode each source has an electron transmission rate. The average measured transmission rate of the prototype system was 61%. **Figure 26** shows the transmission rate of every X-ray beam in the array. The value of the MTF for the system was measured to be approximately 4 cycles/mm, which is 33% higher than the value measured on the Selenia Dimensions system (3.0 cycles/mm).¹³

The entrance dose of the system was measured using a dosimeter (Radcal Accu-Pro 9096) and ion chamber (Radcal 10x6-6M Mammography Ion Chamber Sensor). The ion chamber was placed 2.8 mm from the chest wall in the center of the detector at height of approximately 4 cm. Each measurement was acquired in accumulated dose mode, meaning the dose from all projection views (oblique and perpendicular beams) were accumulated in the

same measurement. For a tube potential of 31.4 kV, the dose rate of the system was found to be 6.74 mR/mAs (Even beams only). Variation of the dose between each measurement was found to be less than 1%.

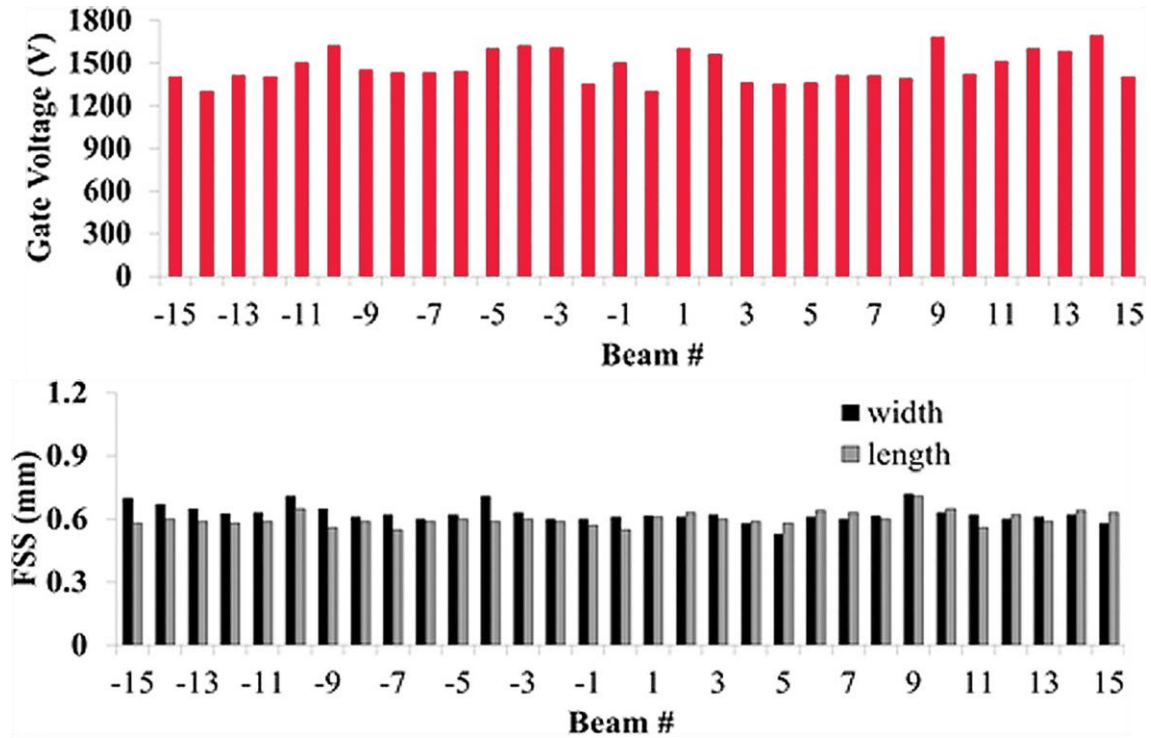


Figure 25: Above - Gate-cathode voltages for the CNT source array at a cathode current of 43mA. The average value was approximately 1.4 kV. **Below** - Measured nominal focal spot sizes. The average focal spot size was found to be 0.64x0.61 mm.

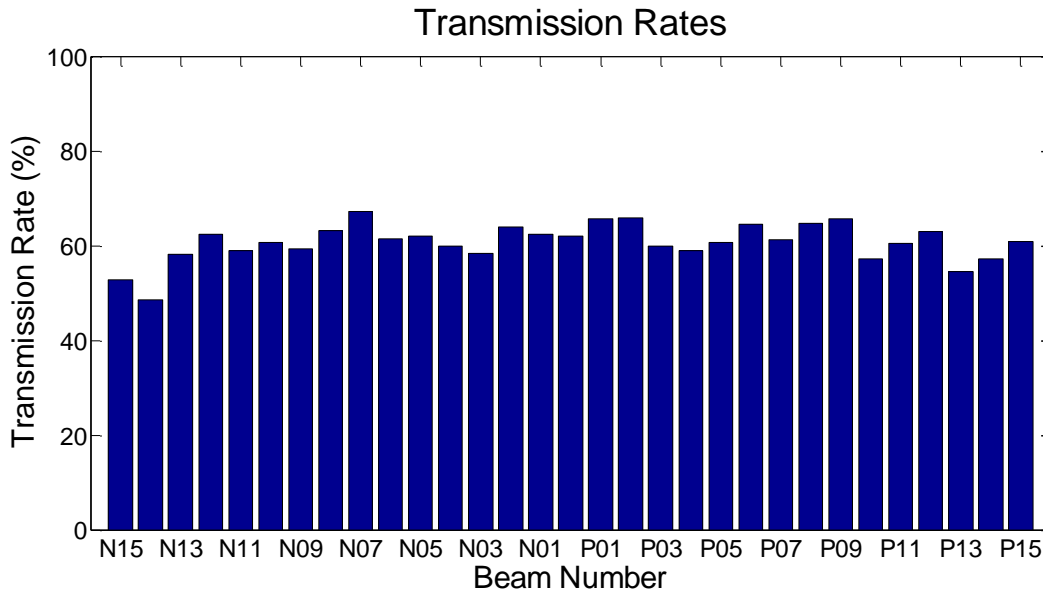


Figure 26: Plot of the transmission rates of each X-ray source in the prototype. The average transmission rate is 61%.

6.4.2 Selenia Dimensions Components

The X-ray detector on the Selenia Dimensions gantry has a pixel size of 70 μm in full resolution mode. DBT images are typically acquired in 2x2 binned mode yielding a pixel size of 140 μm . Having the source array integrated into the Selenia Dimensions DBT system allows for use of the not only the installed flat panel detector but also allows for use of the breast compression paddle and gantry rotation. These extra components are not necessarily useful in a lab setting, but they will be a vital part of the system when it is used on human patients.

6.4.3 Images

Image reconstruction is completed using a dynamic 3D reconstruction software package developed by Real Time Tomography, LLC (Villanova, PA). This software uses a proprietary back projection filtering method.¹⁰² Typical reconstructions are completed using a 30% reduction in reconstruction pixel size from detector pixel size (140 μm to 100 μm) and a distance between reconstruction slices of 0.5 mm.

An American College of Radiology (ACR) mammography accreditation phantom (CIRS Model 015) is used in the clinic to assess the image quality of a system. The ACR phantom

contains aluminum oxide (Al_2O_3) specks ranging from 0.54 mm to 0.16 mm in diameter, masses ranging from 2 mm to 0.25 mm in thickness, and nylon fibers that range from 1.56 mm to 0.4 mm in diameter. **Figure 27** (Left) shows a schematic of the structures contained in the ACR phantom. **Figure 28** shows projection images of the ACR phantom taken on the s-DBT system using 30 kVp and 100 mAs total exposure. In the images you can see the "shifting" effect of the structures as the viewing angle changes. **Figure 29** shows a reconstruction slice of the dataset. When using fidelity display all fibers and masses are visible in this dataset and four groups of specs.

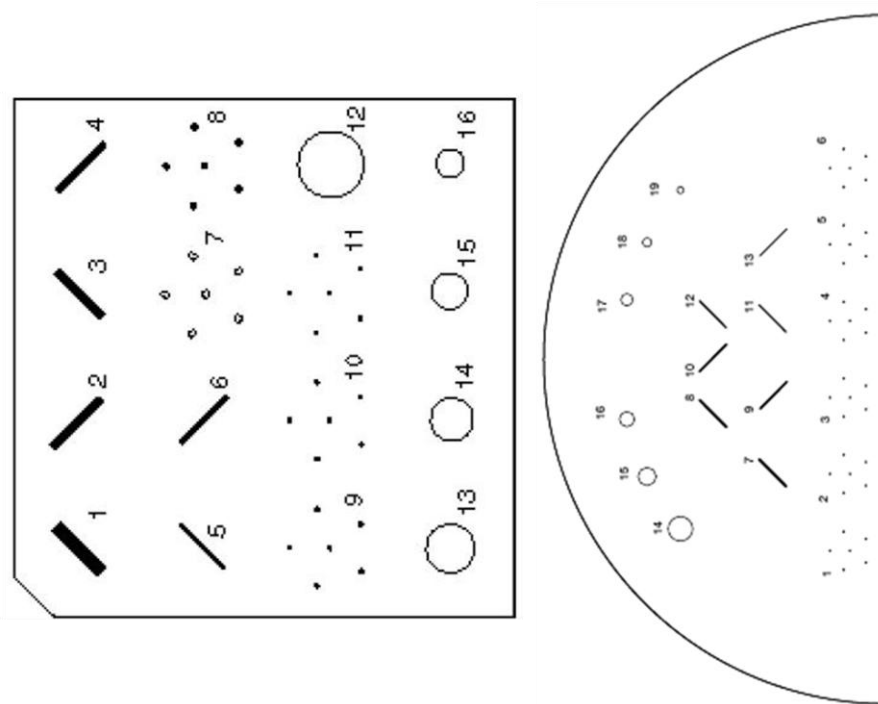


Figure 27: Left - Schematic of the structures contained in the ACR mammography accreditation phantom. **Right** - Schematic of the target slab in the BR3D tomosynthesis phantom.

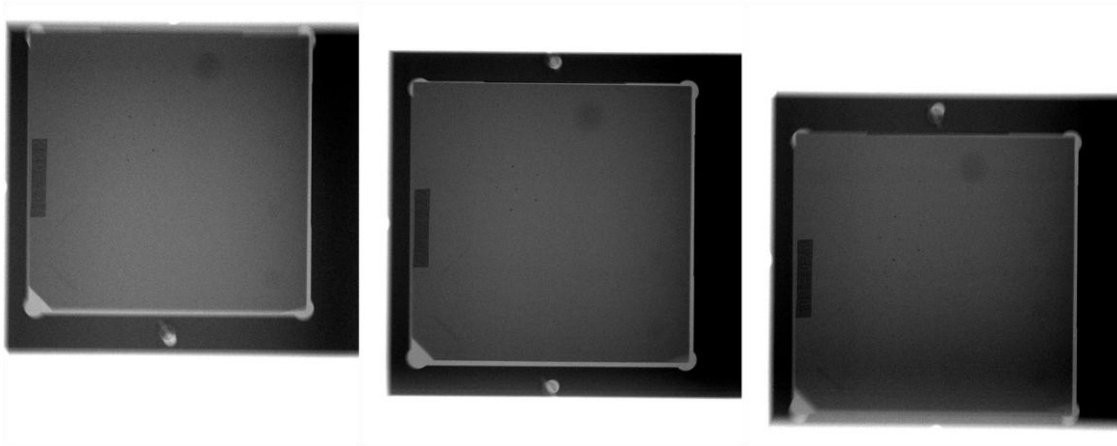


Figure 28: Projection images from beam N14 (**Left**), 000 (**Middle**), and P14 (**Right**) of the ACR phantom from the s-DBT prototype. Images were taken at 30 kVp and 100 mAs total exposure.

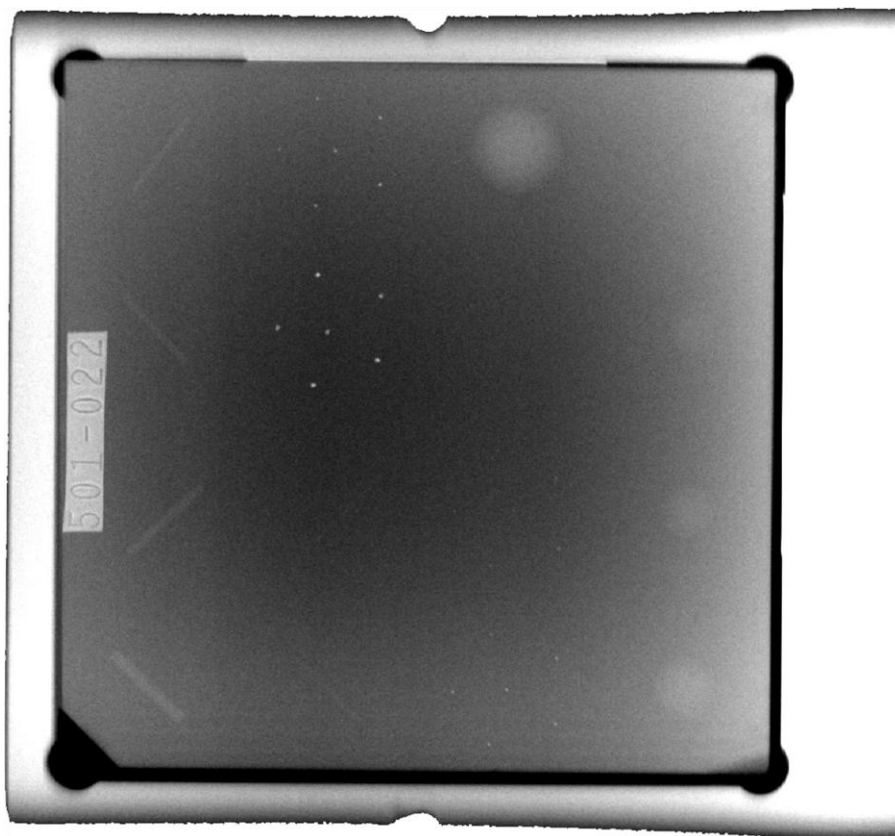


Figure 29: Reconstruction slice of the ACR phantom dataset. When using fidelity display all fibers and masses are visible in this dataset and four groups of specs.

The ACR phantom does not demonstrate the removal of tissue overlap in DBT reconstructions since it has a uniform background. The BR3D phantom (CIRS Model 020) contains similar structures as the ACR phantom but has multiple breast tissue mimicking

background slabs which makes it a more ideal phantom for DBT reconstruction demonstrations. One slab (target slab) contains various sized fibers (10 mm in length and 0.15 to 0.60 mm in diameter), spheroidal masses (1.80 to 6.32 mm in diameter, and microcalcifications (0.13 to 0.40 mm in diameter). **Figure 27** (Right) shows a schematic of the target slab of the BR3D phantom. **Figure 30** shows projection images of the ACR phantom taken on the s-DBT system using 30 kVp and 100 mAs total exposure. Ignoring the dose difference, the projection images are similar to an FFDM image and therefore have a large amount of tissue overlap which decreases lesion visibility. **Figure 31** shows a reconstruction slice of the dataset. A majority of the tissue overlap that is present in the projection images has been removed in the reconstruction image.

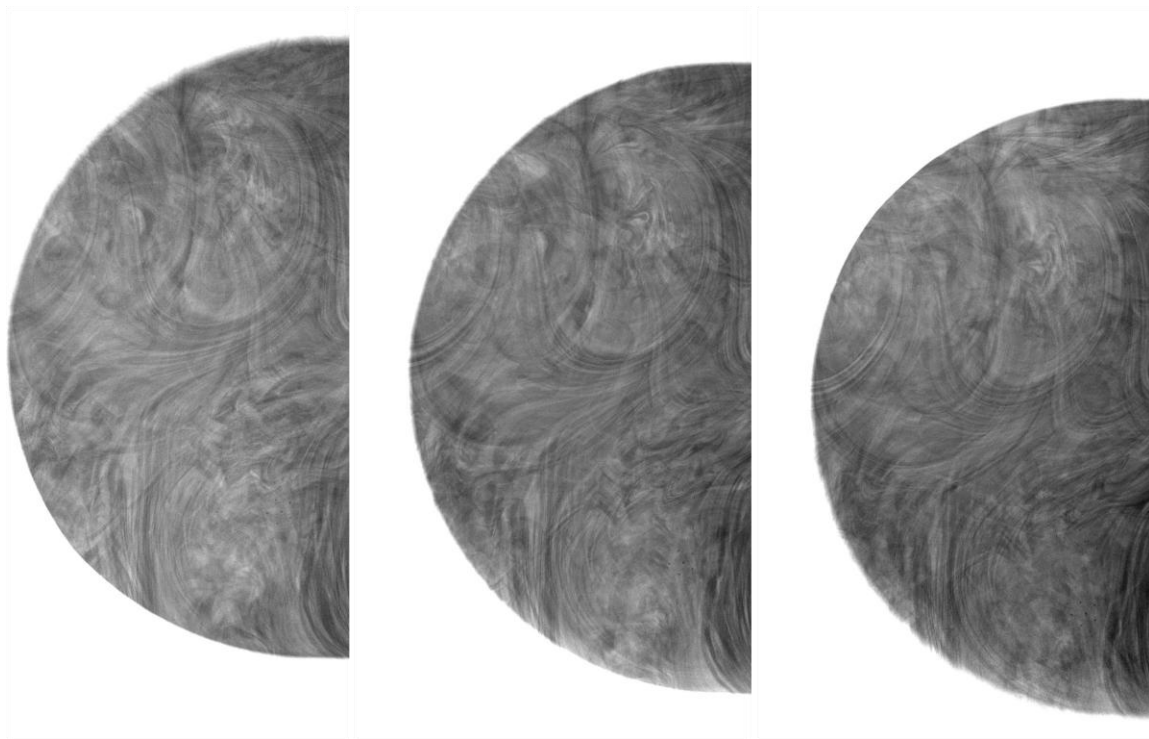


Figure 30: Projection images from beam N14 (**Left**), 000 (**Middle**), and P14 (**Right**) of the BR3D phantom from the s-DBT prototype. There is a large amount of tissue overlap present in the images which will be removed in the reconstruction slices.

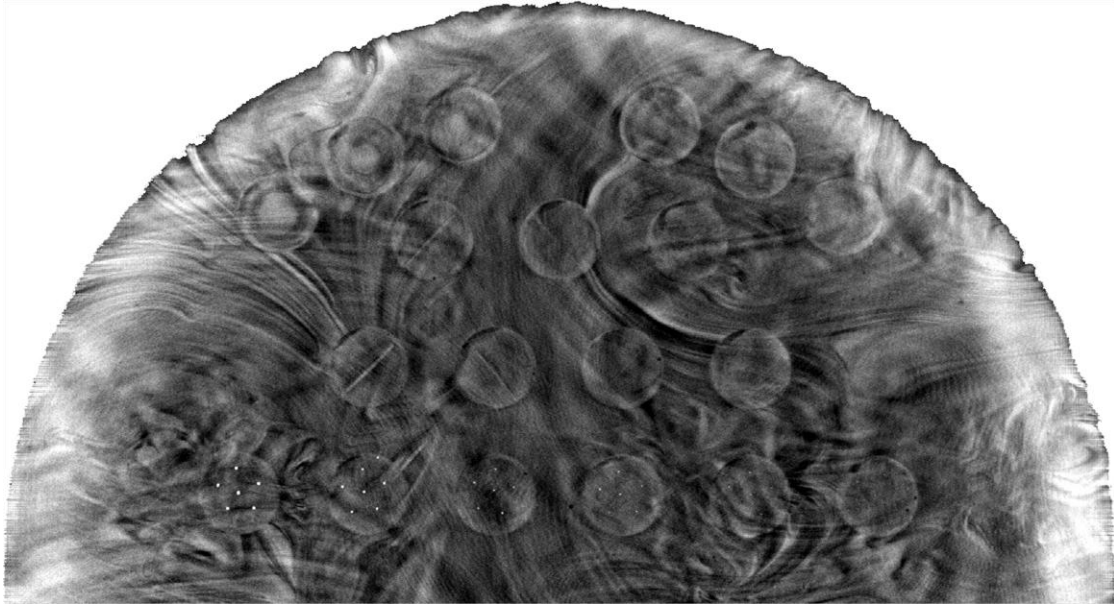


Figure 31: Reconstruction slice of the ACR phantom dataset. Compared to the projection images **Figure 30** most of the underlying and overlying tissue has been removed in the reconstruction.

6.5 Conclusion

Two prototype s-DBT systems have been constructed. The current prototype system is capable of producing a full set of projection images with no motion blur in a short acquisition time. The increased spatial resolution of s-DBT over rotating gantry DBT systems could help improve the visibility of MCs and thus help in the diagnosis of breast cancer.

REFERENCES

- 1 S.M. Moss, H. Cuckle, A. Evans, L. Johns, M. Waller, L. Bobrow, "Effect of mammographic screening from age 40 years on breast cancer mortality at 10 years' follow-up: a randomised controlled trial," *Lancet* **368**, 2053-2060 (2006).
- 2 L. Nystrom, I. Andersson, N. Bjurstam, J. Frisell, B. Nordenskjold, L.E. Rutqvist, "Long-term effects of mammography screening: updated overview of the Swedish randomised trials," *Lancet* **359**, 909-918 (2002).
- 3 J.G. Elmore, M.B. Barton, V.M. Moceris, S. Polk, P.J. Arena, S.W. Fletcher, "Ten-year risk of false positive screening mammograms and clinical breast examinations," *New England Journal of Medicine* **338**, 1089-1096 (1998).
- 4 T. Wu, R.H. Moore, E.A. Rafferty, D.B. Kopans, "A comparison of reconstruction algorithms for breast tomosynthesis," *Med Phys* **31**, 2636 (2004).
- 5 T.D. James, III, J.G. Devon, "Digital x-ray tomosynthesis: current state of the art and clinical potential," *Physics in Medicine and Biology* **48**, R65 (2003).
- 6 A.P. Smith, L. Niklason, B. Ren, T. Wu, C. Ruth, Z. Jing, "Lesion visibility in low dose tomosynthesis," in *Digital Mammography* (Springer, 2006), pp. 160-166.
- 7 S.P. Poplack, T.D. Tosteson, C.A. Kogel, H.M. Nagy, "Digital breast tomosynthesis: initial experience in 98 women with abnormal digital screening mammography," *AJR. American journal of roentgenology* **189**, 616-623 (2007).
- 8 I. Andersson, D.M. Ikeda, S. Zackrisson, M. Ruschin, T. Svahn, P. Timberg, A. Tingberg, "Breast tomosynthesis and digital mammography: a comparison of breast cancer visibility and BIRADS classification in a population of cancers with subtle mammographic findings," *European radiology* **18**, 2817-2825 (2008).
- 9 M. Bissonnette, M. Hansroul, E. Masson, S. Savard, S. Cadieux, P. Warmoes, D. Gravel, J. Agopyan, B. Polischuk, W. Haerer, "Digital breast tomosynthesis using an amorphous selenium flat panel detector," *Proc. SPIE* **5745**, (2005).
- 10 B. Ren, C. Ruth, T. Wu, Y. Zhang, A. Smith, L. Niklason, C. Williams, E. Ingal, B. Polischuk, Z. Jing, "A new generation FFDM/tomosynthesis fusion system with selenium detector," *Proc. SPIE* **7622**, (2010).
- 11 X. Gong, S.J. Glick, B. Liu, A.A. Vedula, S. Thacker, "A computer simulation study comparing lesion detection accuracy with digital mammography, breast tomosynthesis, and cone-beam CT breast imaging," *Med Phys* **33**, 1041-1052 (2006).
- 12 X. Qian, A. Tucker, E. Gidcumb, J. Shan, G. Yang, X. Calderon-Colon, S. Sultana, J. Lu, O. Zhou, D. Spronk, F. Sprenger, Y. Zhang, D. Kennedy, T. Farbizio, Z. Jing, "High resolution stationary digital breast tomosynthesis using distributed carbon nanotube x-ray source array," *Med Phys* **39**, 2090 (2012).
- 13 E. Shaheen, N. Marshall, H. Bosmans, "Investigation of the effect of tube motion in breast tomosynthesis: continuous or step and shoot?," *Proc. SPIE* **7961**, (2011).

- 14 J. Zhou, B. Zhao, W. Zhao, "A computer simulation platform for the optimization of a breast tomosynthesis system," *Med Phys* **34**, 1098-1109 (2007).
- 15 R.J. Acciavatti, A.D. Maidment, "Optimization of continuous tube motion and step-and-shoot motion in digital breast tomosynthesis systems with patient motion," *Proc. SPIE* **8313**, (2012).
- 16 X. Qian, R. Rajaram, X. Calderon-Colon, G. Yang, T. Phan, D.S. Lalush, J. Lu, O. Zhou, "Design and characterization of a spatially distributed multibeam field emission x-ray source for stationary digital breast tomosynthesis," *Med Phys* **36**, 4389-4399 (2009).
- 17 C. Kamphuis, F.J. Beekman, "Accelerated iterative transmission CT reconstruction using an ordered subsets convex algorithm," *Medical Imaging, IEEE Transactions on* **17**, 1101-1105 (1998).
- 18 J. Kuo, P.A. Ringer, S.G. Fallows, P.R. Bakic, A.D. Maidment, S. Ng, "Dynamic reconstruction and rendering of 3D tomosynthesis images," *Proc. SPIE* **7961**, (2011).

CHAPTER 7: OPTIMIZATION OF AN S-DBT SYSTEM

7.1 Overview

Purpose: In principle, an s-DBT system has better image quality when compared to continuous motion DBT systems due to zero motion blur of the source. We have developed an s-DBT system by using a linear CNT x-ray source array. The purpose of the current study was to quantitatively evaluate the performance of the s-DBT system; and investigate the dependence of imaging quality on the system configuration parameters.

Methods: Physical phantoms were used to assess the image quality of each configuration including in-plane resolution as measured by the modulation transfer function (MTF), in-plane contrast as measured by the signal difference to noise ratio (SdNR), and depth resolution as measured by the z-axis artifact spread function (ASF). Five parameters were varied to create five groups of configurations: (1) total angular span; (2) total number of projection images; (3) distribution of exposure (mAs) across the projection images; (4) entrance dose; (5) detector pixel size.

Results: It was found that the z-axis depth resolution increased with the total angular span but was insensitive to the number of projection images, mAs distribution, entrance dose and detector pixel size. The SdNR was not affected by the angular span or the number of projection images. A decrease in SdNR was observed when the mAs was not evenly distributed across the projection images. As expected, the SdNR increased with entrance dose and when larger pixel sizes were used. For a given detector pixel size the in-plane resolution was found to be insensitive to the total angular span, number of projection images, mAs distribution, and entrance dose. A 25% increase in the MTF was observed when the detector

was operating in full resolution mode (70 μm pixel size) compared to 2x2 binned mode (140 μm pixel size).

Conclusions: The results suggest that the optimal imaging configuration for an s-DBT system is a large angular span, an intermittent number of projection views, and a uniform mAs distribution over all views. With the detector operating at full resolution, a stationary DBT system can achieve an in-plane resolution of 5.1 cycles per mm, which is significantly better than continuous motion DBT systems.

7.2 Motivation for System Optimization

Many variables must be taken into account when configuring a DBT system for optimal image quality. Factors such as the x-ray source, detector, reconstruction algorithm, image processing method, and imaging configuration must be tested and selected in order to realize the full potential of a system. A large number of previous studies have reported on the performance of rotating source DBT systems with respect to imaging configurations.^{14, 15, 103-107} Shaheen et al.¹⁴ conclude that a step-and-shoot system has higher contrast for imaging of MC clusters when compared to a continuous motion system. A number of studies have reported that an increase in the angular coverage of the projection images results in an improvement of z-axis resolution.^{15, 103-106, 108} Chawla et al.¹⁰³ report that increasing the dose level results in increased image quality. It has been reported that there is an optimal number of projection images for a fixed angular span, increasing the number of projection images above this number can reduce image quality.^{103, 105-107, 109}

The goal of the current study is to investigate how the reconstructed image quality is affected by imaging parameters in an s-DBT system. The parameters investigated include the total angular span, number of projection views, entrance dose, mAs distribution across the projection images, and detector pixel size. Analysis was done on reconstructed images of physical phantoms using quantitative measures including SdNR, z-axis ASF and the MTF.

7.3 Methods

Using the s-DBT system, two phantoms were imaged using different configurations with different sets of imaging parameters. The resultant projection images were then reconstructed into a pseudo-3D volume and analysis was completed on the reconstructed slices.

Reconstructed images are created using a back projection filtering method developed by Real Time Tomography, LLC (Villanova, PA).¹⁰² The value of the MTF was calculated from the reconstruction of a 50 μm wire phantom. The SdNR and ASF were calculated from the reconstructed images of a mammography accreditation phantom. An overall quality factor (QF) was determined from the three calculated values.

7.3.1 Configuration Parameters

The quality of tomosynthesis reconstruction images can depend on many factors such as the total angular span of the projection images, the number of projection images, the entrance dose, distribution of the mAs, the detector resolution and sensitivity, and the reconstruction algorithm. Here we concentrated on the variation of geometry parameters, entrance dose, and detector resolution.

Five groups of comparison studies were completed: (1) Comparison of 14° versus 28° angular span for a fixed total entrance dose uniformly distributed over 15 projection views; (2) Comparison of 15 versus 29 projection views for a fixed total entrance dose uniformly distributed over an angular span of 28°; (3) For a fixed entrance dose, angular span of 28°, and 29 projection views we compare uniform versus non-uniform distributions of the mAs; (4) For a fixed angular span of 28° and 29 projection views, we varied the total entrance dose from 385 mR to 791 mR; (5) Comparison of image quality for a detector operating in full resolution mode versus 2x2 binning mode. A summary of all configurations studied are listed in **Table 7**.

Table 7: List of configurations and parameters that were analyzed. Five parameters were changed in order to create different configurations; number of projection views, total angular span, entrance dose, distribution of the mAs, and detector resolution. Some configurations are described by multiple groups and therefore appear multiple times in the table. Differences in entrance dose for equal mAs values can be attributed to different source to object distances for different x-ray sources. MMOC stands for more mAs on central projections. LMOC stands for less mAs on central projections.

Group	Number of Projections	Total Angular Span	Angular Spacing	Entrance Dose (mR)	Detector Resolution (μm)	Distribution of the mAs
1	15	14°	1°	727	140	Uniform
1	15	28°	2°	682	140	Uniform
2	15	28°	2°	682	140	Uniform
2	29	28°	1°	656	140	Uniform
3	29	28°	1°	656	140	Uniform
3	29	28°	1°	665	140	LMOC
3	29	28°	1°	675	140	MMOC
4	29	28°	1°	385	140	Uniform
4	29	28°	1°	523	140	Uniform
4	29	28°	1°	656	140	Uniform
4	29	28°	1°	791	140	Uniform
5	15	28°	2°	682	70	Uniform
5	15	28°	2°	682	140	Uniform

7.3.2 Entrance Dose

The entrance dose was measured for each configuration using a dosimeter (Radcal Accu-Pro 9096) and ion chamber (Radcal 10x6-6M Mammography Ion Chamber Sensor). The ion chamber was placed 2.8 mm from the chest wall in the center of the detector at the same height as the top of the phantoms (approximately 4 cm). A constant tube voltage of 31.4 kV was used for all configurations. The entrance dose for each configuration was measured three times. Each measurement was acquired in accumulated dose mode, meaning the dose from all projection views (oblique and perpendicular beams) were accumulated in the same measurement. The average of the three measurements was used as the entrance dose for the configuration. Variation of the dose between the measurements was found to be less than 1%.

7.3.3 Phantom Imaging

Two phantoms were imaged for each configuration. A 50 μm tungsten wire phantom was used to determine the MTF of each configuration. The phantom was placed in the center of the detector near the focal line of the x-ray source. The wire was fixed to a metal frame and positioned parallel to the detector. A slight angle (approximately 3 degrees) from perpendicular to the chest wall was applied to the wire to allow for oversampling of the line spread function (LSF). The same radiographic magnification factor of 1.12 (object-detector distance of 47.5 mm) was used for every configuration. An American College of Radiology (ACR) mammography accreditation phantom (CIRS Model 015) was imaged to assess the SdNR of masses and z-axis ASF sensitivity of MCs. The ACR phantom contains aluminum oxide (Al_2O_3) specks ranging from 0.54 mm to 0.16 mm in diameter, masses ranging from 2 mm to 0.25 mm in thickness, and nylon fibers that range from 1.56 mm to 0.4 mm in diameter. **Figure 32** shows a schematic of the structures contained in the ACR phantom (**Left**) and a reconstructed volume slice of the ACR phantom using the s-DBT system (**Right**).

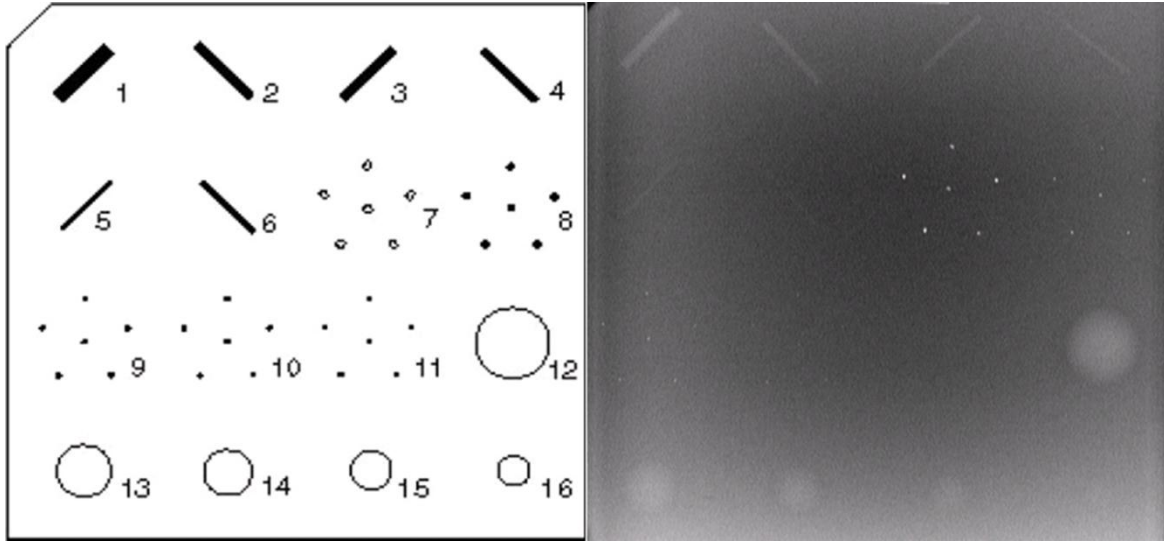


Figure 32: **Left:** Schematic of simulated masses MCs and fibers located in the ACR phantom. Analysis was conducted on the masses and MCs. **Right:** ACR phantom reconstructed slice acquired using the s-DBT system.

7.3.4 Image Processing and Reconstruction

For every projection image a corresponding blank image was acquired. A blank image is an image where there is no object in the field of view of the detector. A different blank image was acquired for each mAs value. For each detector readout time, fifteen dark images were acquired and averaged. All projection images were processed using **Equation 16**, which corrects for detector and beam non-uniformity as well as gain offsets.

Equation 16:

$$\text{Image} = \frac{\text{Projection} - \text{Dark}}{\text{Blank} - \text{Dark}}$$

Image reconstruction was completed using a dynamic 3D reconstruction software package developed by Real Time Tomography, LLC (Villanova, PA). This software uses a back projection filtering method.¹⁰² The reconstructed images had a pixel size of 100 μm and a distance between slices of 0.5 mm, which is smaller than the 1 mm distance used in a typical breast tomosynthesis examination. The smaller slice distance was used in order to get better sampling of the z-axis ASF.

7.3.5 Modulation Transfer Function Calculation

The size of the smallest object that a DBT system can detect is dependent on the in-plane resolution. The value of the MTF is a good indication of the in-plane resolution. Using the 50 µm tungsten wire phantom the system MTF was calculated using a slant angle oversampling method.^{110, 111} Using the reconstructed slice at the focal plane of the wire, multiple LSFs were sampled. The LSFs were then formed into a single oversampled LSF using the calculated angle of the wire. The resultant oversampled LSF was then fitted into a Gaussian function in order to remove noise. The Fourier Transform of the fitted Gaussian function is the MTF. The resolution frequency at 10% MTF peak value was used as the quantitative measure of the in-plane image resolution.

7.3.6 Signal Difference to Noise Ratio Calculation

The ability of a DBT system to detect masses in the breast is primarily determined by in-plane contrast. Signal difference to noise ratio is a measure of the contrast with respect to the noise level. The SdNR was calculated on the largest mass, 2 mm in thickness, which is embedded in the ACR phantom. The largest mass was selected to ensure the object of interest was present in every reconstructed dataset. The foreground was selected to be the central region of the mass (approximately 2500 pixels in size) and the background was selected to be a ring-like region surrounding the mass (approximately 2700 pixels in size).

To determine the noise in the foreground and background, a moving average filter was applied across the original image and the resultant filtered image was subtracted from the original unfiltered image. This step removes systematic variation of the background image that is not due to noise. The standard deviation was taken of the two regions in the subtracted image. The SdNR was calculated as:

Equation 17:

$$\text{SdNR} = \frac{|\mu_{\text{signal}} - \mu_{\text{bkg}}|}{\sqrt{0.5 * (\sigma_{\text{signal}}^2 + \sigma_{\text{bkg}}^2)}}$$

where “ μ_{signal} ” and “ μ_{bkg} ” are the average pixel intensity of the foreground and background respectively and “ σ_{signal} ” and “ σ_{bkg} ” are the corresponding standard deviations.¹⁴

7.3.7 Artifact Spread Function Analysis

Due to the limited angle that tomosynthesis projections are taken, reconstructed slices at a particular focal plane can have “shadow” artifacts from objects that are at another depth. The ability of a particular DBT system to resolve objects in the z-axis (perpendicular to the detector) is a measure of the depth resolution. This is quantified by the z-axis artifact spread function.¹⁴ In this study, the ASF was calculated for the largest aluminum oxide specks (0.54 mm in diameter) in the ACR phantom. The largest specks were selected to ensure the object of interest was present in every reconstructed dataset. These specks are used to simulate MCs. There is a cluster of six 0.54 mm diameter specks in the phantom. ASF analysis was completed on all six specks in the cluster. Due to the small size of the MC it is difficult to determine the average pixel intensity value of the speck. We calculated the ASF by taking the maximum pixel value found in a small region of interest (ROI), where the speck of interest is located, through every reconstructed slice of the reconstruction space.¹⁴ The reconstructed slices are separated by 0.5 mm along the z-axis. As the distance from a slice to the object of interest's focal plane increases, the intensity of the ASF decreases. We use the full width at half maximum (FWHM) of the ASF as a quantitative measure of the z-axis spatial resolution. The ASF at plane “z” is defined as:

Equation 18:

$$\text{ASF}(z) = \frac{|\max(\text{signal}(z)) - \mu_{\text{bkg}}(z)|}{\mu_{\text{bkg}}(z)}$$

where “ $\max(\text{signal}(z))$ ” is the maximum pixel value of the ROI for the slice located at “z”, and “ $\mu_{\text{bkg}}(z)$ ” is the average value of the background pixels of the ROI for the slice.¹⁴ Once the ASF was calculated the data was fitted to a Gaussian function plus a smooth background before the FWHM was determined.

7.3.8 Overall Image Quality Factor

All three physical measurements: MTF, SdNR, and ASF are important in assessing the image quality of a reconstructed image set. The detection of MCs (high contrast objects) is primarily determined by the spatial resolution measured by the ASF and MTF, while the ability to detect masses (low contrast objects) is primarily determined by the SdNR. Sechopoulos and Gheti¹⁰⁶ used an overall image QF that took into account the effect of contrast to noise ratio and ASF on image quality. Here we define the relative overall image QF as:

Equation 19:

$$QF = \frac{1}{3} \left(\frac{SdNR}{SdNR_0} + \frac{ASF_0}{ASF} + \frac{MTF}{MTF_0} \right)$$

where “SdNR” is the value determined from the signal difference to noise ratio calculation, and “ASF” is the FWHM of the artifact spread function, and “MTF” is the spatial resolution at 10% MTF peak value. MTF_0 , $SdNR_0$, and ASF_0 refer to the corresponding values for the reference configuration of 28 degrees, 15 projection views, 682 mR, and 140 μ m detector pixel.

7.4 Results

The SdNR and the FWHM of the ASF were calculated for each configuration from the reconstructed images of the ACR phantom. The value of the MTF at 10% was determined from the reconstructed images of the tungsten wire phantom. The values of the SdNR and MTF are averages of five measurements taken from the same datasets. Errors were not reported for the FWHM of the ASF and the QF due to insufficient statistical measurements. All the results acquired are summarized in **Table 8**.

Table 8: Calculated results for SdNR, FWHM of the ASF, and MTF. Data is separated into the five groups of configurations that were outlined in **Section 7.3.1**. The configuration with 29 projection views, a 28 degree angular span, and an even dose distribution resulted in the highest “QF” value for an exposure of 100 mAs. MMOC stands for more mAs on central projections. LMOC stands for less mAs on central projections.

Group	Number of Proj.	Total Span	Entrance Dose (mR)	Detector Res. (μm)	mAs Dist.	SdNR	FWHM of ASF	MTF at 10%	QF
1	15	14°	727	140	Uniform	5.72±0.21	7.80	4.14±0.01	0.85
1	15	28°	682	140	Uniform	5.44±0.20	4.08	4.20±0.03	1.00
2	15	28°	682	140	Uniform	5.44±0.20	4.08	4.20±0.03	1.00
2	29	28°	656	140	Uniform	5.81±0.16	4.10	4.25±0.02	1.02
3	29	28°	656	140	Uniform	5.81±0.16	4.10	4.25±0.02	1.02
3	29	28°	665	140	LMOC	4.97±0.20	4.03	4.23±0.01	0.98
3	29	28°	675	140	MMOC	5.04±0.16	4.05	4.25±0.01	0.98
4	29	28°	385	140	Uniform	4.32±0.14	4.14	4.30±0.01	0.93
4	29	28°	523	140	Uniform	4.87±0.12	3.93	4.28±0.02	0.98
4	29	28°	656	140	Uniform	5.81±0.16	4.10	4.25±0.02	1.02
4	29	28°	791	140	Uniform	6.06±0.24	4.04	4.23±0.02	1.04
5	15	28°	682	70	Uniform	2.97±0.08	4.30	5.15±0.05	0.91
5	15	28°	682	140	Uniform	5.44±0.20	4.08	4.20±0.03	1.00

7.4.1 Modulation Transfer Function

The spatial resolution at 10% MTF was used as a quantitative measure of the in-plane resolution. **Figure 33** shows an example of an oversampled LSF with Gaussian fitted data (**Left**) and the corresponding MTF (**Right**).

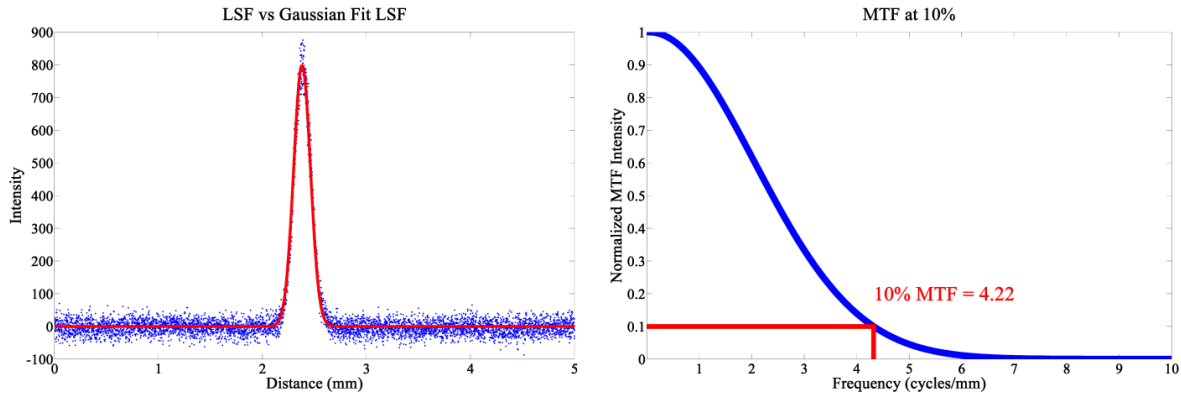


Figure 33: **Left:** Plot of an oversampled LSF and the corresponding Gaussian fitted LSF which was used for MTF calculations. **Right:** MTF of the LSF with the value at 10% highlighted. The MTF was found to be around 4.2 cycles per mm for a detector with a 140 μm pixel size (2x2 binning mode). Since there is no x-ray source motion in an s-DBT system the MTF is found to be primarily dependent on the detector pixel size, and independent of other system parameters (see **Figure 38**).

As can be seen in **Table 8**, there was no statistical difference in the value of the MTF at 10% for the first four groups of configurations. This is because the in plane resolution is predominately determined by the x-ray focal spot size and the detector pixel size. Since there is no focal spot blur in s-DBT for different configurations the MTF does not fluctuate.

7.4.2 Signal Difference to Noise Ratio

A magnified image of the 2 mm thick mass from the ACR phantom, which was used in the calculation of the SdNR, is shown in **Figure 34 (Left)**. Looking at **Table 8** it can be seen that the SdNR did not greatly fluctuate when the angular span was increased (Group 1). This was expected since the only differences in photon counts was the slightly larger source to object distance for the wider angular span. When the number of projection images was increased the SdNR did not change (Group 2). Group 3 had different mAs distributions with the same entrance dose. A lower SdNR was found in the configurations that had non-uniform distributions. This can be attributed to the lower photon counts on some of the projection images of the non-uniform mAs distributions. As expected, when the entrance dose was increased (Group 4) there was a corresponding increase in SdNR. **Figure 35** shows a plot of the SdNR versus entrance dose. It can be concluded that in an s-DBT system the SdNR is primarily dependent on the entrance dose of the projections, not on other parameters.

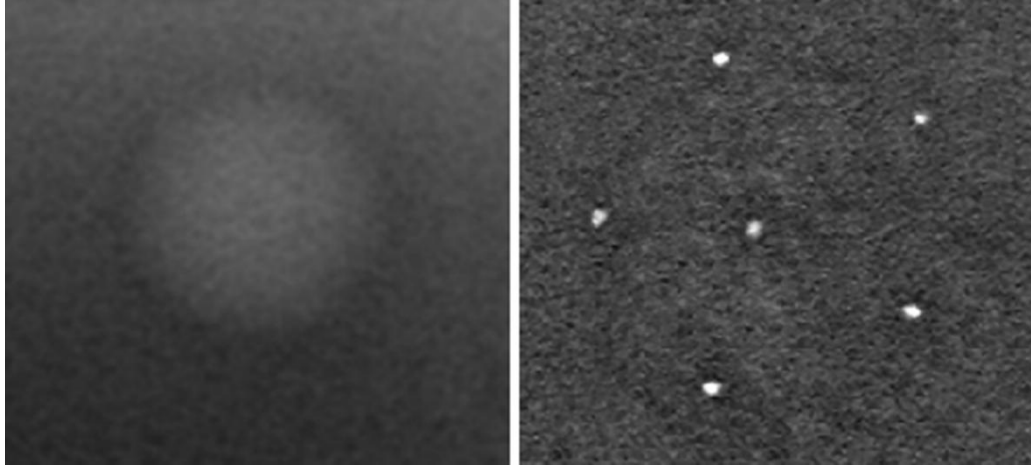


Figure 34: **Left:** Magnified view of 2 mm mass found in the ACR phantom. The SdNR of the mass and the surrounding background was calculated for each configuration. **Right:** Magnified view of the 0.54 mm speck cluster found in the ACR phantom. ASF analysis was completed on all specks in the cluster for each configuration.

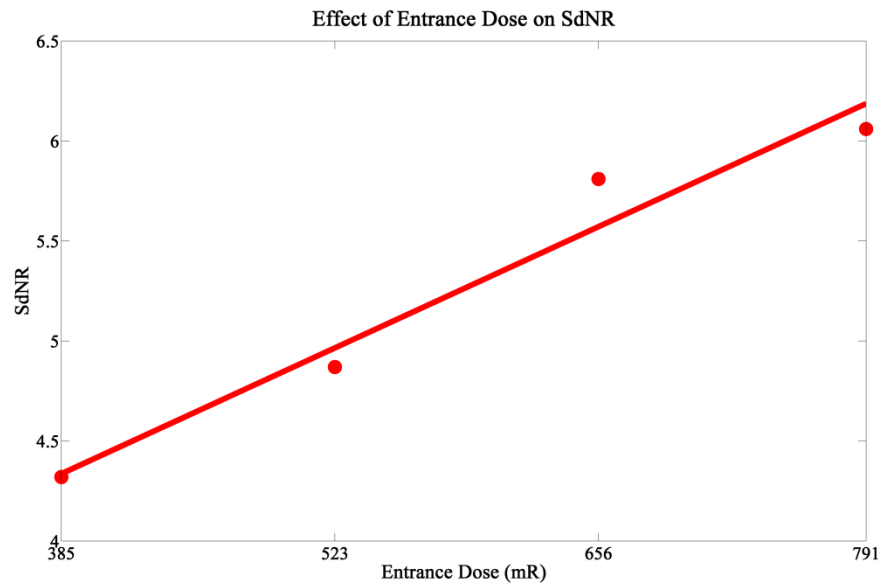


Figure 35: The plot of the SdNR versus total entrance dose shows a linear increase of the SdNR with entrance dose within the dose range examined. A linear fit was applied to the dataset and plotted.

7.4.3 Artifact Spread Function Along the Z-Axis

A magnified image of the cluster of six 0.54 mm specks found in the ACR phantom, which was used in the calculation of the artifact spread function along the z-axis, is shown in **Figure 34 (Right)**. All six specks were used for quantitative analysis of the ASF for all configurations. As can be seen in **Table 8** and **Figure 36**, there is a dramatic change in ASF width going from a 14 degree to a 28 degree angular span while keeping the number of

projection views the same (Group 1). In order to further analyze the effect of angular span on the ASF, another group of images were used with an angular span ranging from 10 to 28 degrees. In this group the entrance dose per projection was kept constant but the number of projection views and total entrance dose decreased with the decrease in angular span. **Figure 37** shows the ASF widths for this group. From this figure it can be seen that the width of the ASF decreases with increasing angular span of the projection images. The decrease can be attributed to the increased information which is collected in the projection space when the angular span is increased. Similar results have been found in previous studies.^{103, 106} For a fixed angular span, the ASF is found to be insensitive to the number of projection views, entrance dose, and mAs distribution (Group 2 - Group 4).

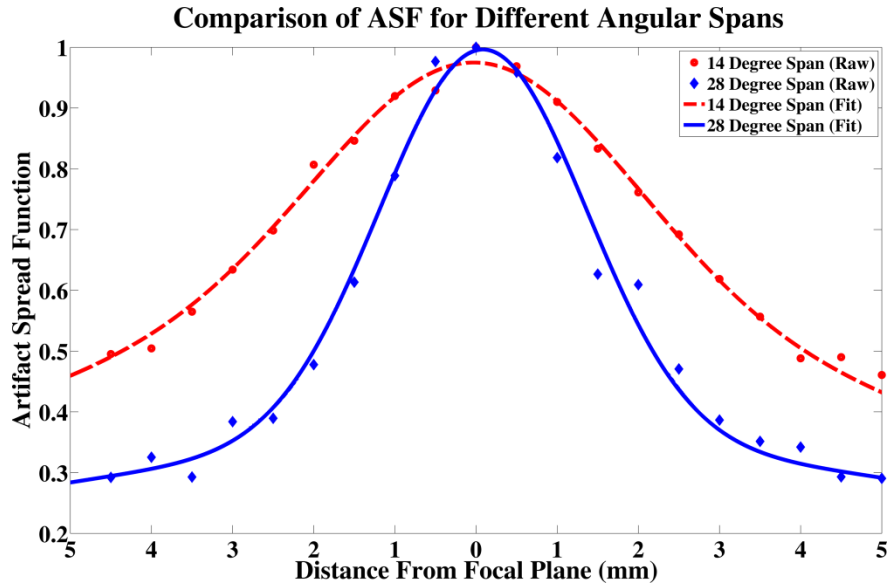


Figure 36: Plot of the ASF of an angular span of 14 degrees versus an angular span of 28 degrees with the same number of projection images and total entrance dose. Both the raw data and the fitted data are shown. The 14 degree span resulted in a much broader ASF due to the lack of information in the projection space.

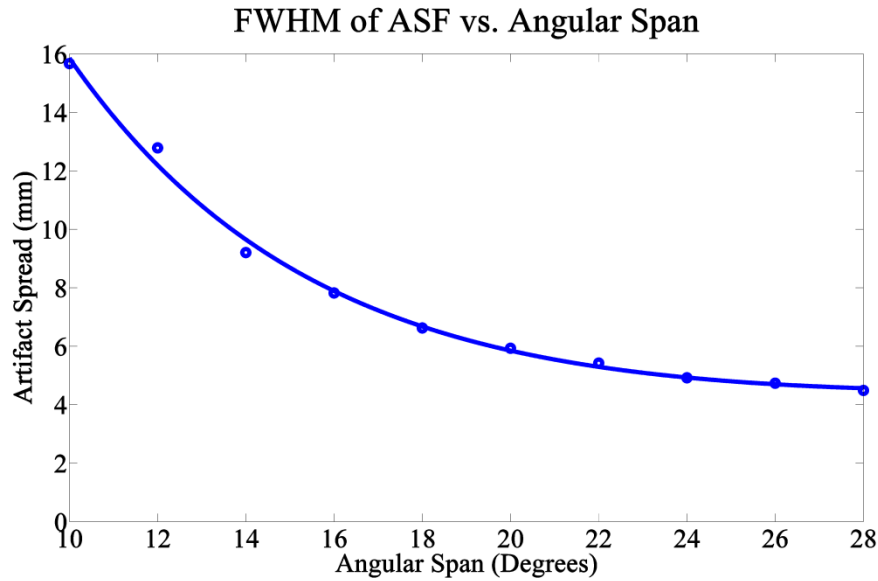


Figure 37: Results comparing the FWHM of the ASF and the total angular span of the projection images. A smooth fit was also applied to the data and plotted. A very noticeable trend can be seen which shows that an increased angular span results in a better artifact spread function.

7.4.4 Detector Pixel Size Comparison

Decreasing the pixel size from 140 μm to 70 μm resulted in a 25% increase in the value of the MTF at 10%. **Figure 38** is a plot of the MTFs for the two pixel sizes. The slight increase in the width of the ASF for the configuration with a 70 μm pixel size when compared to the 140

μm pixel size case is within the uncertainty of the calculation. Since the distance between slices is 0.5 mm, the error in calculation will be at least 1 mm.

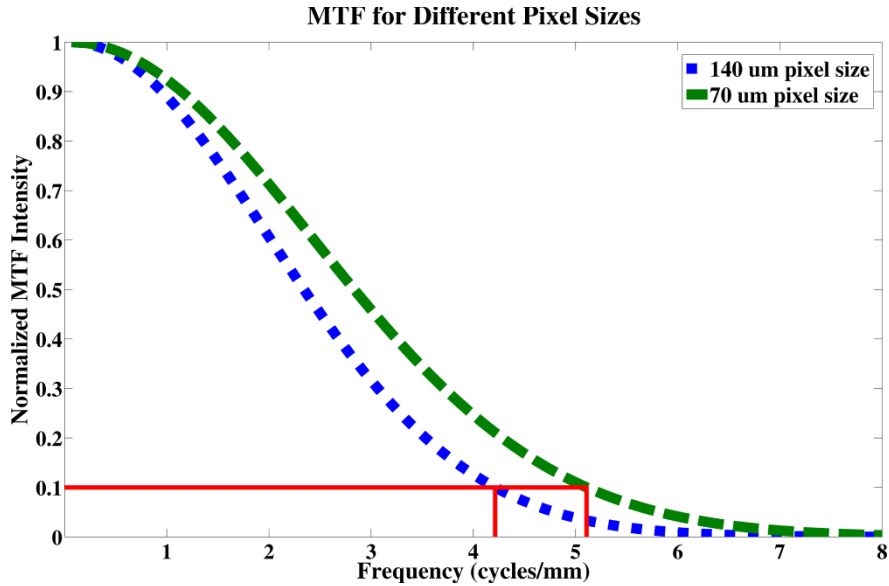


Figure 38: Plot of the MTFs for the 70 μm pixel size and the 140 μm pixel size. The value of the MTF at 10% was found to be approximately 25% better for the 70 μm pixel size (5.1 cycles per mm) when compared to the 140 μm case (4.1 cycles per mm).

The two configurations in group 5 had the same total entrance dose but different detector pixel sizes. A decrease in SdNR was observed for the smaller pixel size configuration. Smaller pixels result in more pixels per area. Thus, the photon count per pixel is decreased resulting in the decrease of SdNR.

7.4.5 Overall Image Quality Factor

The SdNR, MTF, and ASF are all important for assessing the image quality of a configuration. A composite image QF is used to assess the overall performance of a configuration to detect both MCs and masses. The different parameters tested have varying effects on the reconstructed image quality. An increase in entrance dose corresponds to an increase in SdNR. An increase in angular span creates a better artifact spread along the z-axis. A decrease in pixel size creates a better MTF and a worse SdNR. Of all configurations we investigated with 100 mAs exposure, it was found that the highest image QF was from the configuration with 29 projection images distributed uniformly over a 28 degree span and with

binned detector pixels. However, the same configuration with 15 projections had a very similar QF. Using 29 projections instead of 15 projections will increase the total acquisition time by 2.52 seconds (due to additional readout time needed for more projection images). This increase in acquisition time could lead to a significant increase in patient motion during the acquisition, which will degrade the image quality.¹⁶ In clinical practice the image quality may be optimal for the configuration with 15 projection views instead of 29.

7.5 Discussion

The goal of this research was to determine (i) the effect of configuration parameters on image quality, and (ii) the configuration parameters which result in the overall best image quality using the s-DBT system. The in-plane resolution, measured by the MTF, was found to primarily depend on the focal spot size of the x-ray source and the detector pixel size. It is insensitive to the number of projection views, projection view angular span, total entrance dose, and mAs distribution. The system in-plane resolution of our s-DBT system is 4.2 cycles per mm for a detector with 140 μ m pixels, and is 5.15 cycles per mm for one with 70 μ m pixels. Because there is no x-ray source motion the system MTF in s-DBT is independent of acquisition time, total angular span, and the number of projection views. In contrast, rotating source DBT systems can have significant MTF degradation due to motion blur of the focal spot.¹³ Different configurations in DBT systems result in differing MTFs. For example, larger angular spans will require faster x-ray source motion if the total acquisition time and the number of projection images are held constant, resulting in lower MTF values.

An s-DBT system offers the flexibility of non-uniform distribution of the mAs among different projection views. It was found that a uniform distribution resulted in a higher QF than the non-uniform distributions that were tested. We conclude that there is no clear advantage of using non-uniform mAs distribution among different projection views.

As was expected, a higher entrance dose resulted in better image quality. However, the entrance dose used on a patient should be determined based on the thickness and composition of the breast being imaged. In DBT systems the entrance dose is determined by the automatic exposure control (AEC) unit. Based on a low dose scout view the AEC determines both the kVp and total mAs. In general, thin and fatty breasts require less dose in order to get similar image quality as thick and dense breasts. If the total dose is too low it may not be advantageous to distribute it over too many projection views.

The number of projection images did not have a large effect on the overall image quality in our phantom study. However, in clinical practice this may not be the case due to differing acquisition times. The image acquisition time can be calculated from **Equation 20**.

Equation 20:

$$t_{acq} = N * (t_{exp} + t_{readout})$$

Where " t_{acq} " is the total acquisition time, " N " is the number of projection images, " t_{exp} " is the exposure time per projection, and " $t_{readout}$ " is the detector readout time per projection. Assuming that the total mAs stays the same for the 15 projection case as for the 29 projection case, the number of projection images will double and the exposure time per projection will half. Since the readout time of the detector is the same, the total acquisition time will increase by 14 times " $t_{readout}$ ". Using the detector on the current Selenia Dimensions model (" $t_{readout}$ " of 180 ms in 2x2 binned mode) the acquisition time for the 29 projections increases by 2.52 seconds. This is not desirable because the increase in acquisition time will lead to more patient motion, degrading the image quality.

Going from an angular span of 14 degrees to 28 degrees the FWHM of the ASF decreased approximately 50%. The increased z-axis resolution could be very beneficial when imaging patients by reducing tissue obstruction of the object of interest. Increased angular span becomes a problem for rotating source DBT systems due to the increased focal spot blur and/or acquisition time.

Changing from 2x2 binning to full resolution, in an s-DBT system, results in a 25% increase in the value of the MTF. This increase in spatial resolution comes at the cost of SdNR. The increased resolution could be beneficial when trying to image MCs, but may not be desirable for detecting masses due to the loss in SdNR. It may be useful to present two sets of tomosynthesis reconstruction data, one optimized for MC detection using the full detector resolution projection data, and another for detecting masses using post acquisition binned projection data.

7.6 Conclusions

The optimal configuration of the CNT based stationary digital breast tomosynthesis system has been investigated. A configuration with a large angular span, an intermittent number of projection views, and an even mAs distribution resulted in the best overall image quality. Decreasing the pixel size from 140 μm to 70 μm resulted in an s-DBT system resolution of 5.15 cycles per mm, 60% better than continuous motion DBT systems (3 cycles per mm).¹³

REFERENCES

- 1 A.S. Chawla, J.Y. Lo, J.A. Baker, E. Samei, "Optimized image acquisition for breast tomosynthesis in projection and reconstruction space," *Med Phys* **36**, 4859-4869 (2009).
- 2 Y.-H. Hu, B. Zhao, W. Zhao, "Image artifacts in digital breast tomosynthesis: Investigation of the effects of system geometry and reconstruction parameters using a linear system approach," *Med Phys* **35**, 5242-5252 (2008).
- 3 I. Reiser, R.M. Nishikawa, "Task-based assessment of breast tomosynthesis: Effect of acquisition parameters and quantum noise," *Med Phys* **37**, 1591-1600 (2010).
- 4 I. Sechopoulos, C. Ghetti, "Optimization of the acquisition geometry in digital tomosynthesis of the breast," *Med Phys* **36**, 1199-1207 (2009).
- 5 E. Shaheen, N. Marshall, H. Bosmans, "Investigation of the effect of tube motion in breast tomosynthesis: continuous or step and shoot?," *Proc. SPIE* **7961**, (2011).
- 6 W. Zhao, B. Zhao, P.R. Fisher, P. Warmoes, T. Mertelmeier, J. Orman, "Optimization of detector operation and imaging geometry for breast tomosynthesis," *Proc. SPIE* **6510**, (2007).
- 7 J. Zhou, B. Zhao, W. Zhao, "A computer simulation platform for the optimization of a breast tomosynthesis system," *Med Phys* **34**, 1098-1109 (2007).
- 8 T. Deller, K.N. Jabri, J.M. Sabol, X. Ni, G. Avinash, R. Saunders, R. Uppaluri, "Effect of acquisition parameters on image quality in digital tomosynthesis," *Proc. SPIE* **6510**, (2007).
- 9 B. Ren, T. Wu, A. Smith, C. Ruth, L. Niklason, Z. Jing, J. Stein, "The dependence of tomosynthesis imaging performance on the number of scan projections," in *Digital Mammography* (Springer, 2006), pp. 517-524.
- 10 J. Kuo, P.A. Ringer, S.G. Fallows, P.R. Bakic, A.D. Maidment, S. Ng, "Dynamic reconstruction and rendering of 3D tomosynthesis images," *Proc. SPIE* **7961**, (2011).
- 11 A.L.C. Kwan, J.M. Boone, K. Yang, S.-Y. Huang, "Evaluation of the spatial resolution characteristics of a cone-beam breast CT scanner," *Med Phys* **34**, 275-281 (2007).
- 12 H. Fujita, D.-Y. Tsai, T. Itoh, J. Morishita, K. Ueda, A. Ohtsuka, "A simple method for determining the modulation transfer function in digital radiography," *Medical Imaging, IEEE Transactions on* **11**, 34-39 (1992).
- 13 R.J. Acciavatti, A.D. Maidment, "Optimization of continuous tube motion and step-and-shoot motion in digital breast tomosynthesis systems with patient motion," *Proc. SPIE* **8313**, (2012).
- 14 X. Qian, A. Tucker, E. Gidcumb, J. Shan, G. Yang, X. Calderon-Colon, S. Sultana, J. Lu, O. Zhou, D. Spronk, F. Sprenger, Y. Zhang, D. Kennedy, T. Farbizio, Z. Jing, "High resolution stationary digital breast tomosynthesis using distributed carbon nanotube x-ray source array," *Med Phys* **39**, 2090 (2012).

CHAPTER 8: BREAST SPECIMEN IMAGING WITH S-DBT

8.1 Overview

Objectives: The objective of this study was to compare the stationary digital breast tomosynthesis system (s-DBT) to a conventional mammography system in a study of breast specimens. Radiologist evaluation of image quality was assessed in a reader study. This study represents the first human tissue imaging with the novel carbon nanotube-based s-DBT device.

Materials and Methods: Thirty-nine patients, with known breast lesions (BIRADS 4 or 5) by conventional mammography and scheduled for needle localization biopsy were recruited under an institutional review board-approved protocol. Specimen images were obtained using a 2D mammography system with a 1.8x magnification factor and an s-DBT system without high magnification factor. A reader study was performed with four fellowship-trained breast radiologists over two separate sessions. Malignancy scores were recorded for both masses and microcalcifications (MCs). Reader preference between the two modalities for MCs, masses, and surgical margins was recorded.

Results: The s-DBT system was found to be comparable with magnified 2D mammography for malignancy diagnosis. Readers preferred magnified 2D mammography for MC visualization (p -value < 0.05). However, readers trended toward a preference for s-DBT with respect to masses and surgical margin assessment.

Conclusions: Here we report on the first human data acquired using a stationary digital breast tomosynthesis system. The novel s-DBT system was found to be comparable to magnified 2D mammography imaging for malignancy diagnosis. Given the trend of preference for s-DBT over 2D mammography for both mass visibility and margin assessment, s-DBT could be a viable alternative to magnified 2D mammography for imaging breast specimens.

8.2 Motivation for Specimen Imaging

For this study, we sought to compare the CNT-based s-DBT system to a FFDM system in a study of breast specimens. Radiologists' evaluation of image quality was assessed through a reader study. This study represents the first human tissue imaging with the novel CNT-based device. We hypothesized that in using the s-DBT system, we will generate clinically useful tomographic images of breast specimens that are of comparable quality to conventional high magnification 2D specimen radiographs.

8.3 Methods

8.3.1 Patient Recruitment

Thirty-nine patients, with known breast lesions (BIRADS 4 or 5) from conventional mammography and scheduled for needle localization biopsy were recruited under an institutional review board-approved protocol. Informed consent was obtained for each patient prior to the needle localization. After excision from the patient, the specimen was placed in a standard quasi-radiolucent specimen container, and compressed using the container's own compression mechanism with enough pressure to prevent the tissue from sliding in the container using a perforated grid. **Figure 39 (Left)** shows a 2D radiograph of an empty specimen container. An average specimen thickness of 16 mm after compression was observed. They were then imaged using a GE Senographe FFDM system (General Electric, Fairfield, CT USA) using 26 kVp, 1.8x radiographic magnification, and dose proportional to the specimen's size. After standard of care clinical imaging, all specimens were transported to our research facility and re-imaged using an s-DBT system. The specimens were then transported to the Department of Pathology in the hospital for standard clinical pathology evaluation. All

specimens were returned to Department of Pathology within one hour after excision (cold ischemia time).

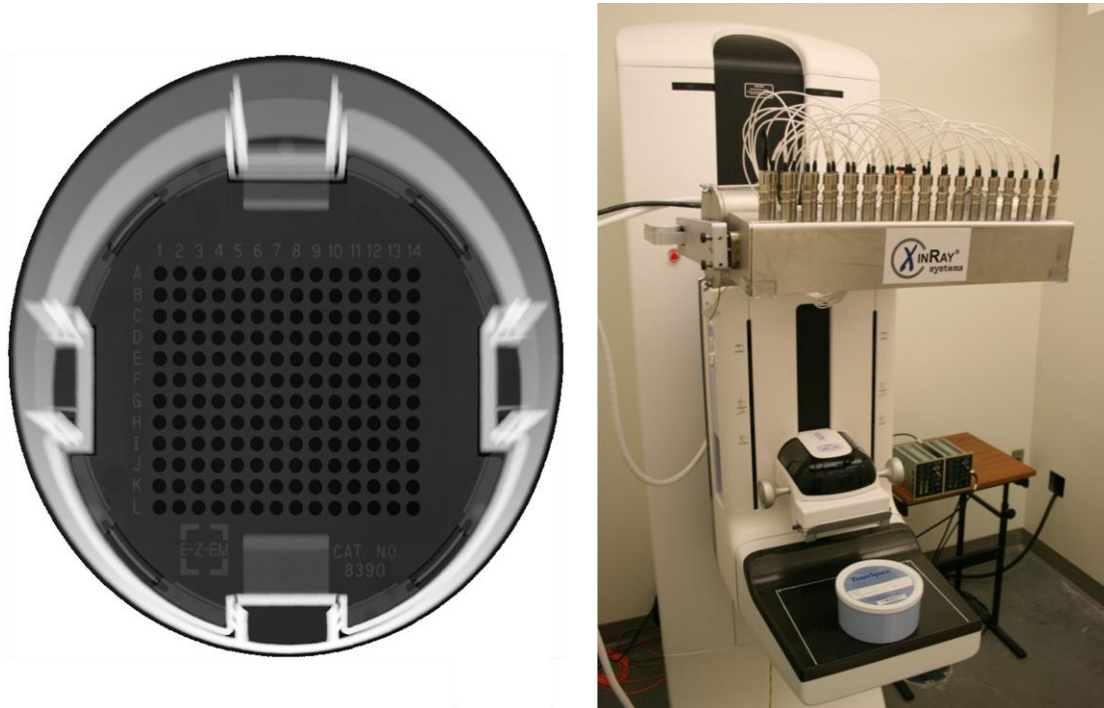


Figure 39: Left - Segmented 2D radiograph of container used to hold specimens. Right - Image of an s-DBT system with specimen container on the detector housing.

8.3.2 Imaging on the s-DBT System

Specimens were imaged on the s-DBT system using 15 projection images distributed over 28 degrees, 1.08x radiographic magnification, 26 kVp, 100 mAs, and a detector pixel size of 70 μm . **Figure 39 (Right)** shows the s-DBT system with a specimen container on the detector housing. Projection images were reconstructed into a 3D volume using a back-projection filtering method developed by Real Time Tomography, LLC (Villanova, PA USA).¹⁰² Images were reconstructed using a 0.5 mm distance between slices and a pixel size equivalent to that of a 1.8x magnified image (the magnification used for the 2D radiograph).

8.3.3 Reader Study Design

A reader study was performed with four breast fellowship-trained radiologists over two separate sessions; all images were viewed in each session. During the initial session, half of

the specimens were viewed using 2D mammography first, and half using s-DBT first. For the second session, the readers were shown the images in reverse order. Four weeks wash-out time was given between the two reader sessions. The readers gave a malignancy score between 1 and 5 (1 - benign, 3 - 50% chance of malignancy, 5 - highly malignant) for both masses and MCs in the specimen, and a confidence score for their malignancy diagnosis (0 - 100%). The numeric malignancy score was not based on BIRADS. Margin assessments were only completed for the modality shown first; negative if the lesion was fully contained in the margins or positive if the margins extend to the edge of the specimen. After malignancy and confidence scores were recorded, the second modality was shown to the reader to determine the readers preference between s-DBT and mammography. Reader preference was recorded between -3 and +3 in increments of one (-3 - 2D preferred, 0 - equally preferred, +3 - s-DBT preferred). Reader preference was recorded for three different categories for each specimen, as applicable; (1) shape/morphology of masses, (2) MC assessment, and (3) margin assessment. Statistical analysis was completed by a qualified biostatistician.

8.4 Results

Four radiologists evaluated 42 specimens from 39 patients. Readers 1, 2, 3, and 4 had 11, 16, 19, and 1 years of practicing radiology respectively. The sensitivity and specificity of each modality was calculated for each reader. **Table 9** shows the calculated values using 3 as the threshold for a positive response (interpreted as malignant). Two of the four readers recorded a higher sensitivity using s-DBT than 2D mammography. Two readers gave higher specificity values for 2D mammography, one gave a higher specificity value for s-DBT, and one reader (Reader 3) did not diagnose any specimens as benign.

Table 9: Calculated sensitivity and specificity values by modality and reader. Values were calculated from malignancy scores. Malignancy scores from 3 to 5 were considered positive for disease.

2D = 2D digital mammography modality

s-DBT = stationary digital breast tomosynthesis modality

Reader	Sensitivity		Specificity	
	2D	s-DBT	2D	s-DBT
1	24/24 (1.00)	23/25 (0.92)	4/14 (0.29)	2/13 (0.15)
2	21/25 (0.84)	19/25 (0.76)	5/14 (0.36)	7/14 (0.50)
3	24/25 (0.96)	25/25 (1.00)	0/13 (0.00)	0/13 (0.00)
4	23/25 (0.92)	25/25 (1.00)	4/14 (0.29)	2/14 (0.14)

Reader preference for the shape/morphology of masses is shown in **Table 10**. A reader preference of 0.07 ± 1.34 was recorded, where a positive value represents a preference for s-DBT. The difference in the reader preference between the two modalities for masses was insignificant.

Table 10: Average reader preference for the shape/morphology of masses, MC assessment, and margin assessment. Positive values represent a preference for stationary digital breast tomosynthesis compared to 2D mammography.

Reader	Masses			Microcalcifications			Margins		
	Mean	STD	p-value	Mean	STD	p-value	Mean	STD	p-value
1	-1.02	1.40	<.05	-1.80	1.01	<.05	-0.44	1.35	<.05
2	0.18	1.20	0.4094	-0.54	0.70	<.05	0.19	1.14	0.2984
3	0.75	1.35	<.05	-0.20	0.98	0.259	0.70	1.35	<.05
4	0.08	0.86	0.5800	-0.62	0.52	<.05	0.21	0.72	0.0743
Overall	0.07	1.34	--	-0.70	0.95	--	0.16	1.22	--

Table 10 also shows the reader preference for MC assessment. Overall, an average preference of -0.70 ± 0.95 was recorded, where a negative value represents a preference for 2D mammography. **Figure 40** shows reconstruction slices and the corresponding 2D image of a

specimen with a suspicious cluster of MCs. With the high spatial resolution of s-DBT the MCs are visible in the reconstruction.

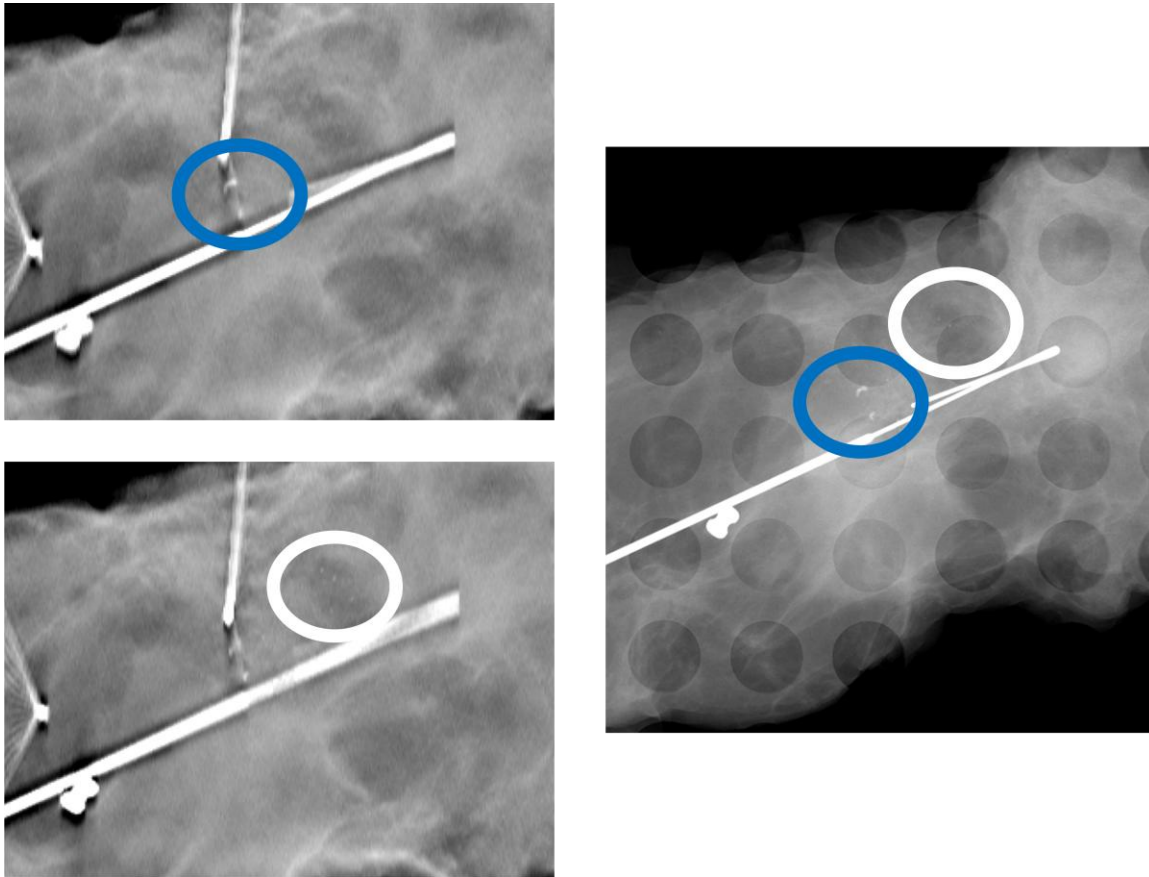


Figure 40: Left Above - Reconstructed slice of a specimen using an s-DBT system. **Left Below** - Reconstruction slice located 1.5 mm below the previous slice. **Right** - 2D mammography image of the same specimen. The high spatial resolution of the s-DBT system allows for imaging of small microcalcifications. The added z-axis information allows for better visualization of MC clusters. The blue oval envelopes a cluster of large MCs and the white oval envelopes a cluster of small MCs.

Table 10 also shows the reader preference with respect to surgical margin assessment. The average preference for margins was 0.16 with a standard deviation of 1.22, where a positive value represents a preference for s-DBT. **Figure 41** shows an s-DBT reconstruction slice and a 2D mammography image of a specimen with a suspicious lesion with spiculated margins. Clear margin delineation is present in the s-DBT reconstruction; however, tissue overlap in the 2D image reduces margin visibility. This particular lesion was later diagnosed as malignant.

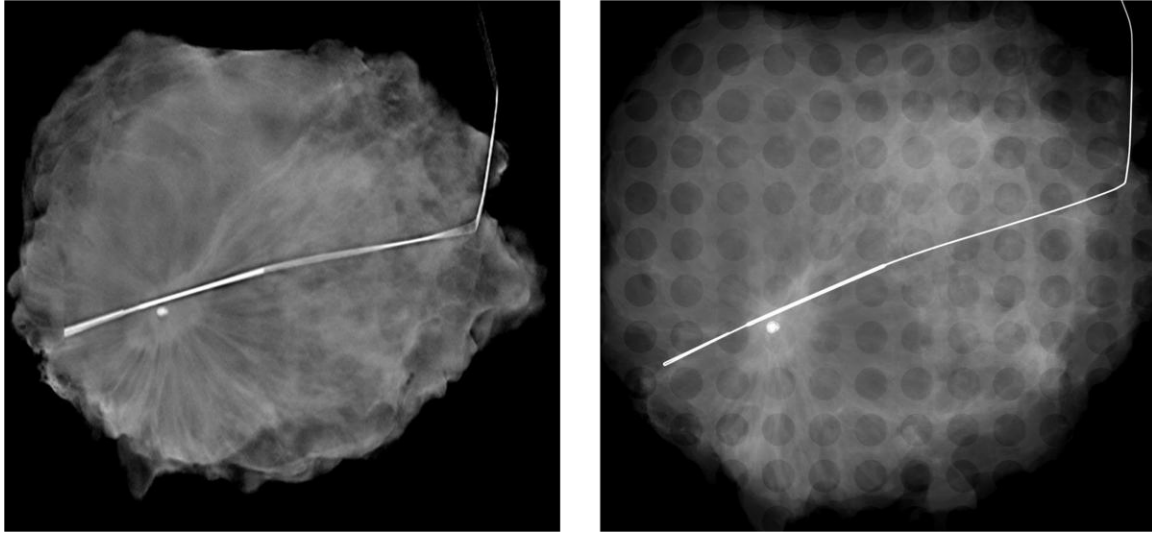


Figure 41: Left - Reconstructed slice of a specimen using an s-DBT system. The spiculated margins and architectural distortion are more apparent along all edges compared to the 2D mammography image of the same specimen (**Right**).

A secondary analysis was completed on the reader preference results by a biostatistician. It was tested whether the mean reader preference was larger than zero using a linear mixed model with a random intercept effect and Wald test. It was assumed the correlation in reader preference for each specimen between any two readers was the same. The results trended toward a preference for the s-DBT system in terms of the shape and morphology of masses and margins. It was found that readers preferred FFDM over s-DBT for MC visibility (p-value < 0.05). The results of the secondary analysis can be found in **Table 11**.

Table 11: Results of the secondary analysis performed on the preference portion of the reader study. It was tested whether the mean preference was larger than zero using a linear mixed model with a random intercept effect and Wald test.

Item of Interest	Grand Mean Estimate	Standard Error	Two-sided p-value
Shape/morphology	0.0598	0.1416	0.6751
Microcalcifications	-0.6718	0.1030	<0.05
Margins	0.1586	0.1422	0.2718

8.5 Discussion

Overall malignancy diagnosis of the two modalities was comparable. The prevalence of malignancy in our specimens was 25 out of 39, due to the fact that recruited patients had a

status of BIRADS 4 or higher. Thus, we would anticipate a bias toward malignant diagnosis within our specimens given the initial malignant diagnosis.

Readers trended toward a preference for s-DBT with respect to masses and surgical margins compared to magnified 2D mammography. However, magnified 2D mammography was preferred when viewing MCs. A large amount of reader fatigue was noted between the first and second session. Specifically looking at reader 1 for surgical margin assessment, it can be seen that their average preference decreased from 0.18 to -1.16, a decrease of 1.34, between the first and second reading session. This is in contrast to all other readers which saw an average increase of 0.51.

Specimen radiography is essentially optimized for 2D mammography, placing s-DBT at a disadvantage for a number of key reasons. Large radiographic magnification factors are used that cannot be replicated on any DBT system, and the specimen container produces artifacts in s-DBT reconstructions. A typical mammography system utilizes both a large and small focal spot. The small focal spot is designated for magnification views, this reduces the effect of focal spot enlargement on image spatial resolution. Typical DBT systems (including the s-DBT system) only use a large focal spot due to power constraints on the anode. Thus for this study, a magnification factor of 1.8 was used for 2D mammography compared to 1.08 for the s-DBT images.

The specimens were held in a conventional specimen container consisting of a rectilinear grid with circular holes. The grid coordinates provide a mechanism for the communication of findings between the radiologist and the pathologist. However, in tomosynthesis, the regularly spaced grids impose additional artifacts within the imaging planes of the specimen, causing image degradation. Simply removing the grid would reduce this image artifact. This was not done in this study in order to preserve the clinical workflow. If s-DBT is used in the future for specimen radiography, it would be beneficial to design a specimen container which reduced artifacts in the reconstruction images. One example could be a cone-

shaped design, the specimen could be held stationary by the walls of the cone and the grid could be placed at a distance above the tissue, thereby reducing the reconstruction artifact.

Another disadvantage of s-DBT in this study was the use of biopsy needles to mark lesions (later used for localization by the pathologist). Some specimens were marked with biopsy needles after the 2D mammogram was acquired in the hospital. In some specimens a large number of needles were present in the s-DBT reconstruction and not present in the 2D mammography image. **Figure 42** shows a reconstruction slice and the corresponding 2D image of a specimen which contained a substantial amount of needles. In the figure, large needle artifacts can be seen in the s-DBT reconstruction which can reduce lesion visibility. In future studies, post processing segmentation and interpolation could be used to reduce the artifacts.

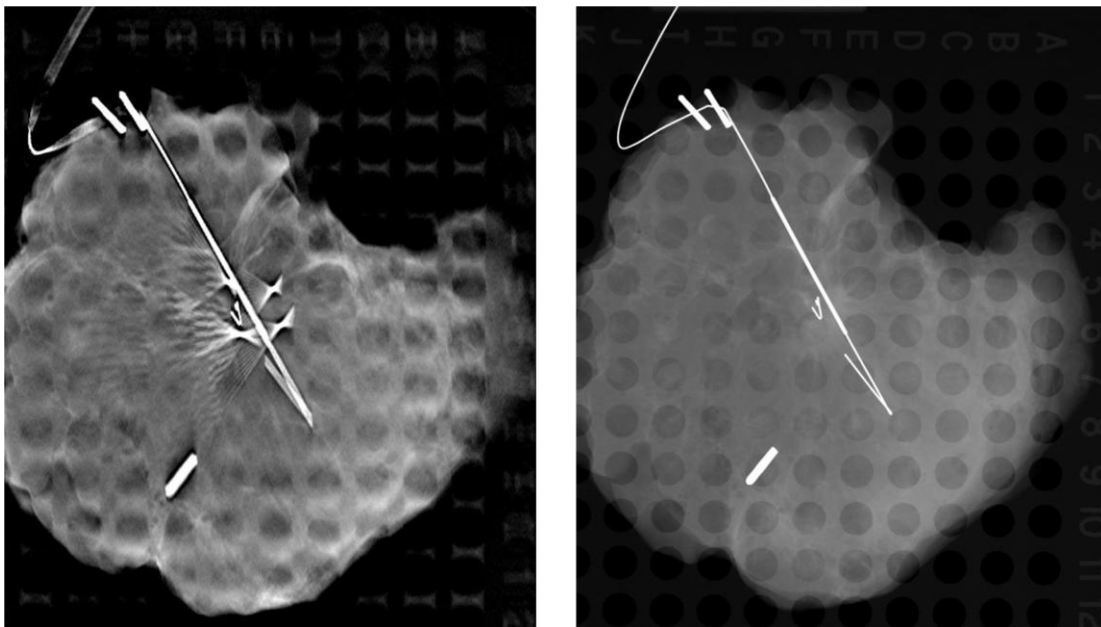


Figure 42: Left - Reconstructed slice of a specimen using an s-DBT system. Right - 2D mammography image of the same specimen. Biopsy needles are present in the s-DBT reconstructions and not in the 2D mammography image.

8.6 Conclusion

In summary, we reported the first human data acquired using a stationary digital breast tomosynthesis system. Lumpectomy specimen images were acquired using a 2D mammography system and an s-DBT system. Stationary digital breast tomosynthesis was

found to be comparable with 2D mammography for malignancy diagnosis but readers were significantly more confident in MC visibility when using 2D mammography (p-value < 0.05). Readers, with respect to masses and surgical margins, trended toward a preference for s-DBT. These results were not significant. Given the trend of preference for s-DBT over 2D mammography for both mass visibility and margin assessment, s-DBT could be a viable alternative to 2D mammography for imaging breast specimens.

REFERENCES

- 1 J. Kuo, P.A. Ringer, S.G. Fallows, P.R. Bakic, A.D. Maidment, S. Ng, "Dynamic reconstruction and rendering of 3D tomosynthesis images," Proc. SPIE **7961**, (2011).

CHAPTER 9: HIGH RESOLUTION MICROCALCIFICATION IMAGING WITH S-DBT

9.1 Overview

Objectives: The objective of this study was to compare the visibility of MCs using s-DBT reconstruction images versus reconstruction images from a continuous motion DBT system. Specimen images were analyzed for x, y, and z MC resolution. A 3D MTF simulation was used to further compare the increased resolution of s-DBT over continuous motion DBT.

Materials and Methods: Lumpectomy images were acquired using the s-DBT system and a continuous motion DBT system. Further analysis was conducted on images where MCs were present. The size of the MC was determined based on a localized threshold value and an artifact spread function (ASF) was calculated. Three-dimensional MTFs were simulated based off various input parameters for each system.

Results: The s-DBT system was found to superior to the continuous motion DBT system for every MC analyzed. The wider angular coverage of the s-DBT system produced narrower ASFs. The average difference in the FWHM of the ASF was 2.00 ± 0.67 mm. A narrower ASF results in a more accurate representation of the MC. The smaller effective focal spot of the s-DBT system, as demonstrated by the 3D simulated MTF, produced more realistic visualizations of the analyzed MCs. For some MCs, the percent decrease in area from DBT to s-DBT was as high as 43%.

Conclusions: It was found that the s-DBT system gave higher resolution imaging of MCs for every MC analyzed. The stationary design allows for full DBT acquisitions with no motion blur and for large angular spans without an increase in total acquisition time. The high resolution of s-DBT could allow for the removal of the 2D acquisition requirement for DBT screening examinations.

9.2 Motivation

Current digital breast tomosynthesis (DBT) systems utilize a single X-ray source which is rotated over an angular span. Systems which follow a continuous acquisition protocol acquire all images while the tube is in motion. This motion causes blurring of the focal spot in one direction, leading to non-isotropic spatial resolution. If the tube travels a sufficient distance during a single acquisition the spatial resolution in the tube travel direction will be poor. Since high resolution is needed in Mammography for visualization of microcalcifications (MCs), continuous motion DBT systems use combo mode when screening patients, which acquires both a DBT acquisition and a high resolution 2D projection image. Combo mode doubles the radiation dose to the patient, which is a large concern in mammography especially when Mammography screening begins at an early age.¹¹²⁻¹¹⁴ Many recent studies have shown that the use of DBT along with a 2D projection image significantly increases sensitivity and decreases the number of false positives in a screening population compared to the 2D projection alone.^{99, 115-118} For cases with MCs, there is no significant difference between combo mode and a single 2D projection image.⁴⁶ Due to the poor spatial resolution of continuous motion DBT systems, the radiation risk to benefit ratio concerning MCs using combo mode is much higher than 2D mammography alone. In order to lower ratio back to 2D mammography levels a DBT system with high spatial resolution is needed.

Utilizing an array of carbon nanotube (CNT) based X-ray sources, we have developed a stationary digital breast tomosynthesis (s-DBT) system.^{13, 20, 119} The s-DBT system is capable of collecting a full set of tomosynthesis projection images with zero motion. The system has been shown to have significantly higher spatial resolution than continuous motion DBT systems when imaging phantoms.^{13, 119} Translating the system into the clinic for human use requires a

significant amount of data and preparation to demonstrate the usefulness of the system.

Imaging lumpectomy specimens allows for human tissue imaging and demonstrates the usefulness without the added dangers of radiation exposure to patients.

In the current study, lumpectomy specimens were imaged using our s-DBT system and a continuous motion DBT system. Calculations were also made on MCs within the images to determine the effect of the increased spatial resolution. A simulated 3D modulation transfer function (MTF) was created to further show the differences in the spatial resolution of the two systems. Using the results of the MC size comparison, it will be determined if the higher spatial resolution of the s-DBT system translates into increased image quality in the clinic.

9.3 Methods

Lumpectomy images were acquired using the s-DBT system and a continuous motion DBT system. Further analysis was conducted on images where MCs were present. The size of the MC was determined based off a localized threshold value and an artifact spread function (ASF) was calculated. Three-dimensional MTFs were simulated based off various input parameters for each system.

9.3.1 Stationary digital breast tomosynthesis system

The s-DBT system consists of a linearly distributed CNT based X-ray source array¹⁷⁻²⁰ which has been retrofitted onto a Hologic Selenia Dimensions DBT system.¹¹ The linear array, manufactured by XinRay Systems, Inc. (Research Triangle Park, NC), contains 31 X-ray generating focal spots distributed over a 30 degree angular span when a 70 cm source to imager distance (SID) is used. **Figure 43** contains an image of the s-DBT system. The system is based on CNT X-ray sources, which use field emission to pull electrons from the cathode instead of thermionic expansion which is used in typical X-ray sources. These sources allow for electronic control of X-ray exposures with near instantaneous firings from a cold state. These sources, coupled with a fast flat panel detector create high resolution images with fast

acquisition times (current acquisition times on the system are limited by the detector readout time). The system is equipped with electrostatic focusing of the electron beam. When engaged, the focusing electrodes are capable of increasing or decreasing the focal size of the system. The nominal focal spot size that can be achieved with the focusing engaged is 0.6 mm. For the specimen images in the study the electrodes were grounded, which produces a focal spot size of 0.9 mm. Grounded focusing was used for ease of implementation.

As previously determined, the optimal configuration of the s-DBT system was used for imaging of the breast specimens. Fifteen projection images covering an angular span of 28 degrees were used. The detector was operated using full resolution, with a pixel size of 70 μm . This configuration yields a measured spatial resolution of greater than 5 cycles/mm.¹¹⁹



Figure 43: Left - An image of the s-DBT system with a specimen container on the detector housing.
Right - An image of a Selenia Dimensions.

9.3.2 Continuous motion digital breast tomosynthesis system

A Selenia Dimensions, manufactured by Hologic Inc. (Bedford, MA), was used to image each breast specimen.¹¹ The Selenia Dimensions uses a single thermionic X-ray source with is in continuous motion during X-ray exposure. The system acquires fifteen projection images evenly spaced over an angular span of 15 degrees. The detector is operated in binned mode yielding a pixel size of 140 μm . This system has been shown to have a spatial resolution of approximately 3 cycles/mm.¹³ An image of the Selenia Dimensions can be found in **Figure 43**.

9.3.3 Imaging protocol

All patients were recruited under an University of North Carolina at Chapel Hill Institutional Review Board approved protocol. Twenty-three patients with known breast lesions, BI-RADS 4 or 5, and scheduled for a lumpectomy procedure were recruited. Specimens were picked up from the operating room and then transferred to the Department of Radiology for imaging on a conventional 2D mammography system. Hospital procedure dictates that all breast specimens be imaged using a magnified 2D image for margin delineation. After imaging on the 2D system, specimens were transferred to our lab for imaging on both the s-DBT system and the Selenia Dimensions. Images were acquired using 26 kVp and 100 mAs for both systems. Specimens were then transferred to the Department of Pathology in the hospital for malignancy determination.

9.3.4 Image processing and reconstruction

All images collected on the s-DBT system were corrected for non-uniformity of the beam and detector as well as gain offset using the following equation:

Equation 21:

$$\text{Image} = \frac{\text{Projection} - \text{Dark}}{\text{Blank} - \text{Dark}}$$

where "Image" is the final processed image, "Projection" is the raw projection image, "Dark" is an average of 15 images were the detector was fired with no X-ray exposure, and

"Blank" is an X-ray exposure with nothing in the field of view of the detector. Images collected on the Selenia Dimensions were processed using the default operation of the system.

Reconstruction of the images was completed using a dynamic reconstruction software package developed by Real Time Tomography (Villanova, PA). The reconstruction uses a proprietary back projection filtering method.¹⁰² All datasets were reconstructed using a 1.8x magnification (equivalent to the radiographic magnification used for specimen imaging), resulting in a nominal reconstruction pixel size of 37 μ m at the detector. The distance between reconstruction slices was 0.5 mm. **Figure 44** shows a reconstruction slice of a specimen from the s-DBT system.

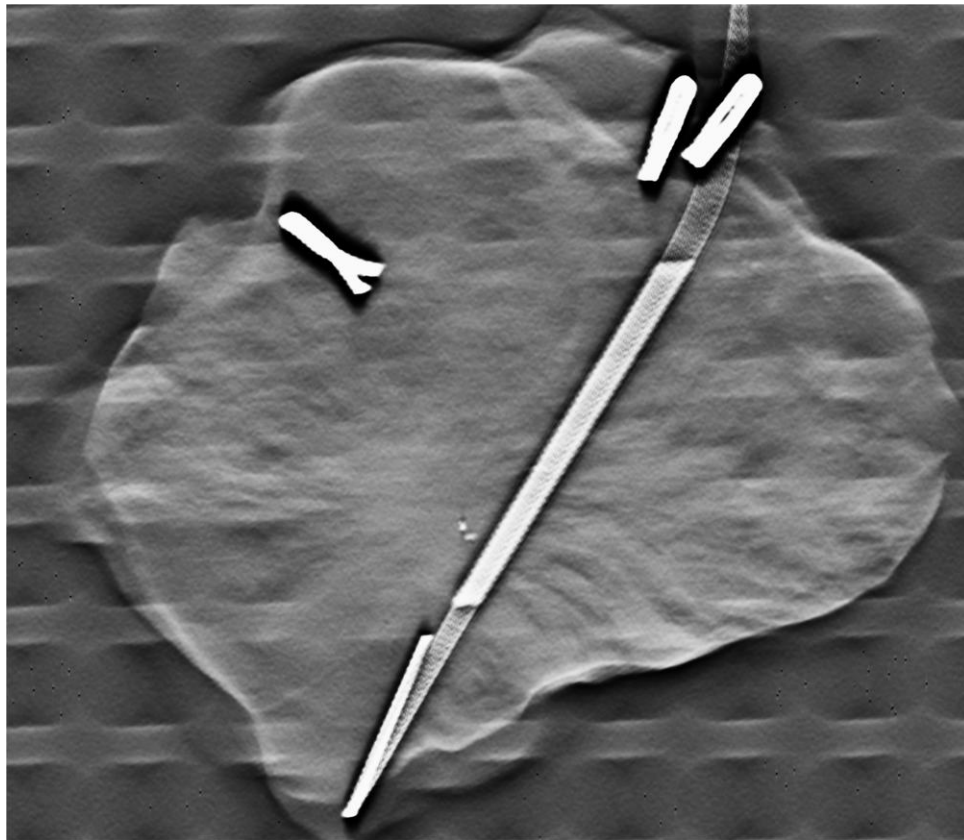


Figure 44: Reconstruction slice of a breast specimen using the s-DBT system.

9.3.5 Microcalcification analysis

Specimen images with MCs were analyzed to further demonstrate the increased resolution of the s-DBT system over the continuous motion DBT system. Twelve individual MCs

were selected for analysis. MCs were only selected if they were visible in both imaging modalities and were not in close proximity to other structures (MCs, localization wires, etc.). To fully localize a lesion information from every direction (x, y, and z) is needed. Each MC was analyzed for in-plane resolution (x and y directions) and for the artifact (z direction) spread function (ASF).

Analysis of in-plane resolution consisted of a localized thresholding method, which used a 50% of the maximum pixel intensity of a small region of interest (ROI) as a cutoff. Pixels with intensity larger than the cutoff were considered as part of the MC. Multiplying the number of pixels in the MC by the reconstruction pixel size yielded an area estimate of the size of the MC.

The ASF was calculated by taking the maximum pixel value found in the ROI through every reconstruction slice of the reconstruction space. As the distance from a slice to the object of interest's focal plane increases, the intensity of the ASF decreases. The full width at half maximum (FWHM) of the ASF was used as a quantitative measure of the z-axis spatial resolution. The ASF at plane “z” is defined as:

Equation 22:

$$ASF(z) = \frac{|\max(\text{signal}(z)) - \mu_{\text{bkg}}(z)|}{\mu_{\text{bkg}}(z)}$$

where “ $\max(\text{signal}(z))$ ” is the maximum pixel value of the ROI for the slice located at “z”, and “ $\mu_{\text{bkg}}(z)$ ” is the average value of the background pixels of the ROI for the slice.¹⁴

9.3.6 Simulated 3D modulation transfer function

The MTF is a measurement used to quantify the spatial resolution of a system. A larger MTF is indicative of a system having higher spatial resolution. In this study, the MTF was simulated for both systems in the x and y directions and using a detector pixel size of 140 and 70 μm at a focus height of 40 mm. The 2D simulated MTFs of the Selenia Dimensions were created using a technique described by Marshall et al, where given; the source to imager distance (SID), radiographic magnification factor, tube travel distance per projection, actual focal

spot size, and detector pixels size an estimate of the projection MTF can be made.¹²⁰ The tube travel distance per projection was calculated using the SID, angular span, total acquisition time, mAs per projection, and tube current. First, the X-ray pulse width was calculated using 100 mAs, 15 projection images, and 200 mA tube current (as stated in the Selenia Dimensions Service Manual). The tube travel distance per projection was calculated by multiplying the total travel distance, calculated from the SID and the angular span, by the pulse width to total acquisition time ratio. The focal spot size of the Selenia Dimensions is 0.46 mm in the tube travel direction and 0.53 mm in the direction perpendicular to motion (as stated in the Selenia Dimensions Service Manual). Multiplying the Fourier transform of the focal spot, tube motion, and detector pixel results in the MTF of the projection image. When creating the s-DBT MTF, the same procedure was followed except zero tube motion was used and the focal spot was modeled as a Gaussian function and not a square function as in thermionic X-ray sources.¹³ The electrostatic focusing of the s-DBT system were grounded in this study resulting in a 0.9 mm focal spot size. The nominal focal spot size the system is 0.6 mm when the electrostatic focusing electrodes are engaged. Both focal spot sizes were simulated.

The resolution of a system In order to create a 3D simulation of the MTF for each system a weighting function, as described by Konstantinidis et al, was used. The equation for the 3D MTF at phase angle " α " is as follows:

Equation 23:

$$MTF_{3D}(\alpha) = MTF_y * \sin^2 \alpha + MTF_x * \cos^2 \alpha$$

where " MTF_{3D} " is the 3D MTF, " MTF_x " is the MTF in the x direction, and " MTF_y " is the MTF in the y direction. A phase angle of zero degrees is represents the spatial resolution along the acquisition direction of the system while an angle of 90 degrees is perpendicular to the acquisition direction. Visualizing the MTF in this method will show how isotropic the spatial resolution of a system is. The 3D MTF images were created using the simulated 2D MTF curves for both systems and detector pixel sizes.

9.4 Results

9.4.1 Microcalcification analysis

A total of 12 MCs were selected for analysis. **Table 12** shows the results of the MC area calculations for all 12 MCs. Since the actual MC size is unknown, a comparison with actual MC size is impossible. However, if it is assumed that a smaller area calculation is equivalent to a sharper image, then for every MC analyzed s-DBT had sharper MC localization than continuous motion DBT. For some MCs, the percent decrease in area from DBT to s-DBT was as high as 43%.

Table 12: The results of the MC area calculation and ASF for all 12 individual MCs that were analyzed. FWHM stands for the full width at half maximum of the ASF.

MC Number	s-DBT Area (mm ²)	DBT Area (mm ²)	Decrease in Area (%)	FWHM s-DBT (mm)	FWHM DBT (mm)	FWHM Diff (mm)
1	3.60	4.09	11.98	3.5	5.0	1.5
2	2.33	3.66	36.34	2.5	4.5	2.0
3	2.79	3.05	8.52	2.0	4.0	2.0
4	1.69	2.79	39.43	1.5	5.0	3.5
5	1.74	3.08	43.51	1.5	4.0	2.5
6	2.96	3.59	17.55	2.5	4.0	1.5
7	1.70	2.74	37.96	1.5	3.5	2.0
8	2.21	3.69	40.11	1.5	4.0	2.5
9	2.10	3.69	43.09	2.5	4.0	1.5
10	2.43	3.21	24.30	3.5	4.5	1.0
11	2.50	3.10	19.35	3.5	5.0	1.5
12	2.82	3.76	25.00	2.5	5.0	2.5

Table 12 shows the results of the ASF calculations. For every MC, s-DBT had a narrower ASF than the continuous motion DBT system. The average difference in the FWHM of the ASF was 2.00 ± 0.67 mm. **Figure 45** shows a comparison of the ASFs of the two systems for MC number 2.

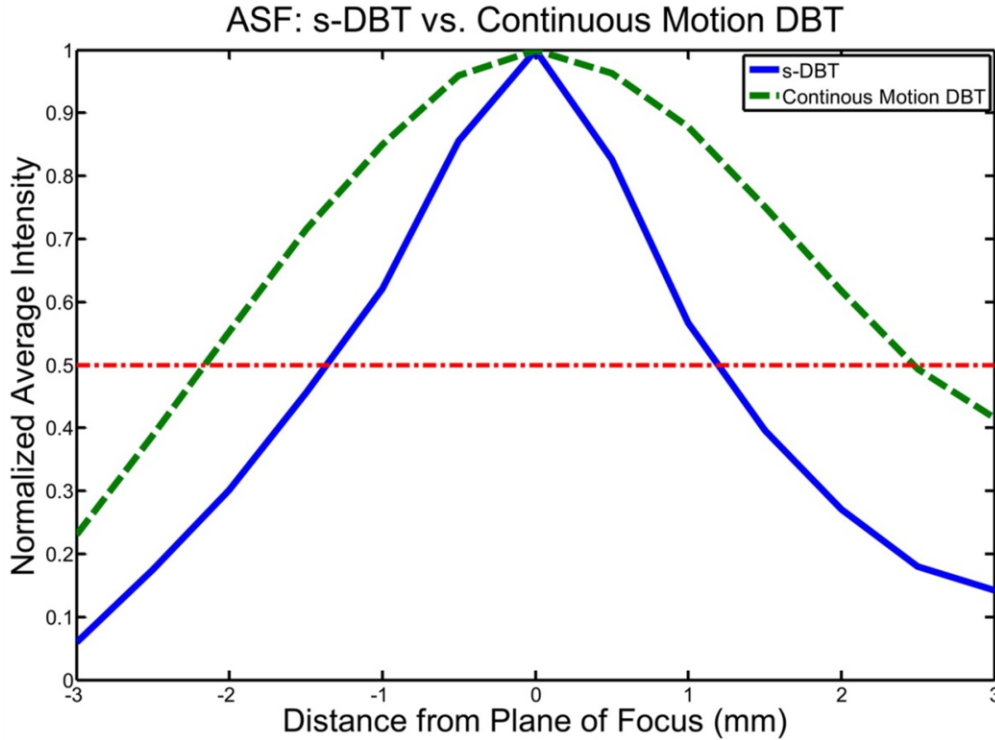


Figure 45: Plot of the ASF for the s-DBT system (solid line) and the Selenia Dimensions system (dashed line) from MC number 2. A line representing the 50% cutoff is shown.

9.4.2 Simulated 3D modulation transfer function

Simulated MTF curves for the s-DBT system can be found in **Figure 46**. The figure shows the effect of the detector pixel size and focal spot size on the MTF curve. For this study a 70 μm pixel size and 0.9 mm focal spot size was used for the s-DBT system. Since the isotropic focal spot of the s-DBT system will produce the same MTF curve in both directions only one curve is present for each combination of pixel size and focal spot size. MTF curves for the Selenia Dimensions system in both the x and y direction can be found in **Figure 46**. The figure shows the MTF curve for the system using a binned and full resolution detector. Acquisitions in the Selenia Dimensions system can only be acquired using binned detector pixels. In the figure it can be seen that the non-isotropic effective focal spot from the Selenia Dimensions creates large differences in the MTF curves. When using the smaller pixel size, the MTF at 10% is 84% larger in the y direction than the x direction (6.7 to 12.3 cycles/mm).

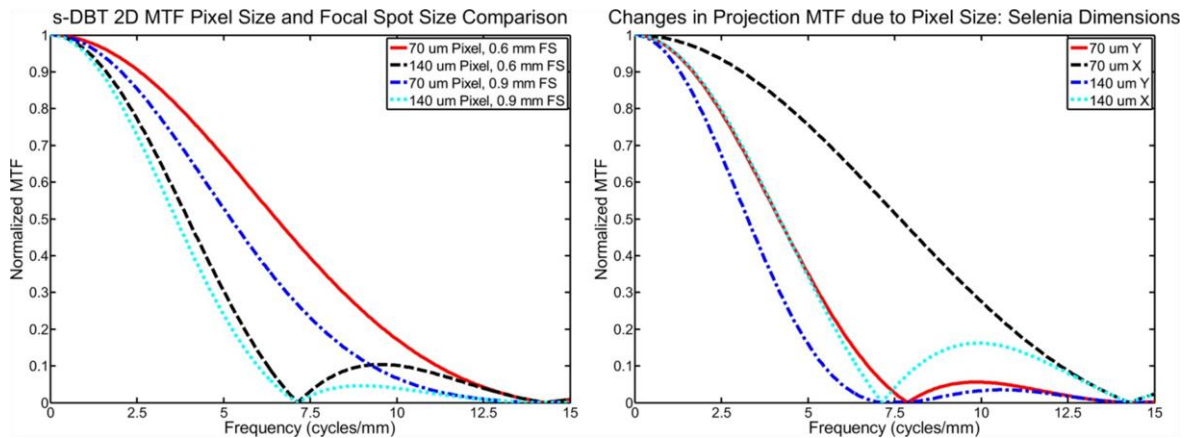


Figure 46: Left - Simulated MTF curves comparing the effect of pixel size and focal spot size in the s-DBT system. Simulations for both a binned and full resolution detector are shown. **Right** - The same curves but for the Selenia Dimensions system.

The simulated 3D MTF for both systems (and both focal spot sizes in the case of s-DBT) and pixel sizes can be found in **Figure 47**. The s-DBT system produces symmetric spatial frequency in every direction on the detector. The Selenia Dimensions produces different spatial frequencies for every non-orthogonal direction. This non-uniformity effect is greatly exaggerated in the 70 μ m detector pixel size case.

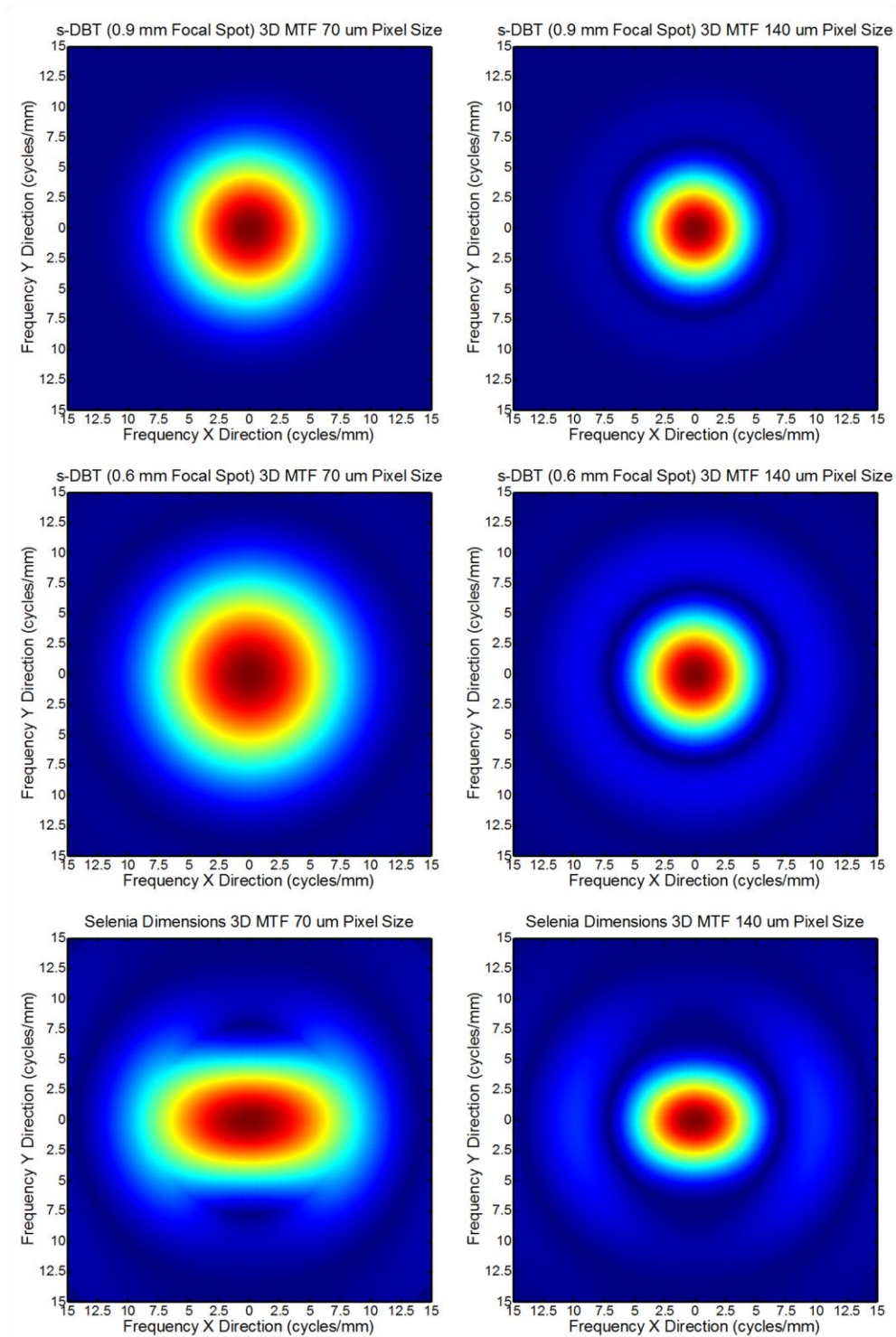


Figure 47: Above - Simulated 3D MTF for the s-DBT system with a 0.9 mm isotropic focal spot size using a 70 μ m (**Left**) and 140 μ m (**Right**) detector pixel size. **Middle** - 3D MTF for the s-DBT system with a 0.6 mm isotropic focal spot size using a 70 μ m (**Left**) and 140 μ m (**Right**) detector pixel size. **Below** - Simulated 3D MTF for the Selenium Dimensions system using a 70 μ m (**Left**) and 140 μ m (**Right**) detector pixel size.

9.5 Discussion

When comparing the measured MC area from the two systems, s-DBT always produced smaller values. Smaller area calculations in-plane translates into sharper images in the x and y direction. As expected, the higher spatial resolution of the s-DBT resulted in increased in-plane MC visibility. The s-DBT system produced better ASFs for every MC that was analyzed compared to the Selenia Dimensions. The s-DBT system is capable of producing larger angular spans without an increase in acquisition time or a loss in spatial resolution.¹¹⁹ The larger angular span of the s-DBT system reduces the out of plane artifacts produced from Fourier domain under sampling in tomosynthesis imaging.

The simulated 3D MTF images show that while the s-DBT system produces uniform spatial resolution, the Selenia Dimensions produces non-uniform spatial resolution. Furthermore, using the full resolution detector in the Selenia Dimensions would create an 84% difference in the spatial resolution from the y direction to the x direction. In the y direction, the spatial resolution is limited by the effective focal spot size and not the detector pixel size, therefore decreasing the pixel size from 140 to 70 μm would do little to increase the spatial resolution in that direction.

When viewing MCs in s-DBT system compared to the Selenia Dimensions the increased spatial resolution brought about by the stationary sources is clearly apparent. **Figure 48** shows a comparison of MC visibility in the s-DBT system and the Selenia Dimension system for MCs number 7 through 12. The increased spatial resolution can be easily seen for every MC. Aliasing from the large pixel size and effective focal spot size can be seen in the Selenia Dimensions images.

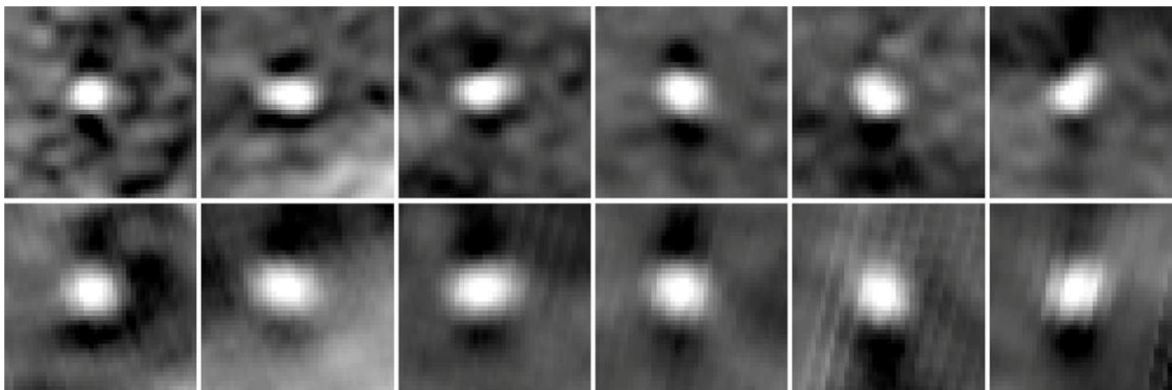


Figure 48: Comparison of MC sharpness for MCs number 7 through 12 between the s-DBT system (**Above**) and the Selenia Dimension system (**Below**). Aliasing from the large pixel size and effective focal spot size can be seen in the Selenia Dimensions images. Specimens were not imaged in the same orientation and can therefore have artifacts in different directions.

9.6 Conclusions

The stationary digital breast tomosynthesis system was compared to a continuous motion DBT system. It was found that the s-DBT system gave higher resolution imaging of MCs for every MC analyzed. The stationary design allows for full DBT acquisitions with no motion blur and for large angular spans without an increase in total acquisition time. The high resolution of s-DBT could allow for the removal of the 2D acquisition requirement for DBT screening examinations.

REFERENCES

- 1 D. Brenner, S. Sawant, M. Hande, R. Miller, C. Elliston, Z. Fu, G. Randers-Pehrson, S. Marino, "Routine screening mammography: how important is the radiation-risk side of the benefit-risk equation?," *International journal of radiation biology* **78**, 1065-1067 (2002).
- 2 A.B. de González, G. Reeves, "Mammographic screening before age 50 years in the UK: comparison of the radiation risks with the mortality benefits," *British journal of cancer* **93**, 590-596 (2005).
- 3 F.A. Mettler, A.C. Upton, C.A. Kelsey, R.N. Ashby, R.D. Rosenberg, M.N. Linver, "Benefits versus risks from mammography: A critical reassessment," *Cancer* **77**, 903-909 (1996).
- 4 D. Bernardi, S. Ciatto, M. Pellegrini, V. Anesi, S. Burlon, E. Cauli, M. Depaoli, L. Larentis, V. Malesani, L. Targa, "Application of breast tomosynthesis in screening: incremental effect on mammography acquisition and reading time," *British Journal of Radiology* **85**, e1174-e1178 (2012).
- 5 G. Gennaro, R.E. Hendrick, P. Ruppel, R. Chersevani, C. di Maggio, M. La Grassa, L. Pescarini, I. Polico, A. Proietti, E. Baldan, E. Bezzon, F. Pomerri, P.C. Muzzio, "Performance comparison of single-view digital breast tomosynthesis plus single-view digital mammography with two-view digital mammography," *European radiology* **23**, 664-672 (2013).
- 6 L. Philpotts, M. Raghu, M. Durand, R. Hooley, R. Vashi, L. Horvath, J. Geisel, R. Butler, "Initial experience with digital breast tomosynthesis in screening mammography," *Proceedings of the 2012 Annual Meeting of the American Roentgen Ray Society*, Vancouver, BC, Canada **29**, (2012).
- 7 P. Skaane, A.I. Bandos, R. Gullien, E.B. Eben, U. Ekseth, U. Haakenaasen, M. Izadi, I.N. Jebsen, G. Jahr, M. Krager, "Comparison of digital mammography alone and digital mammography plus tomosynthesis in a population-based screening program," *Radiology* **267**, 47-56 (2013).
- 8 P. Skaane, A.I. Bandos, R. Gullien, E.B. Eben, U. Ekseth, U. Haakenaasen, M. Izadi, I.N. Jebsen, G. Jahr, M. Krager, "Prospective trial comparing full-field digital mammography (FFDM) versus combined FFDM and tomosynthesis in a population-based screening programme using independent double reading with arbitration," *European radiology*, 1-11 (2013).
- 9 M. Michell, A. Iqbal, R. Wasan, D. Evans, C. Peacock, C. Lawinski, A. Douiri, R. Wilson, P. Whelehan, "A comparison of the accuracy of film-screen mammography, full-field digital mammography, and digital breast tomosynthesis," *Clinical radiology* **67**, 976-981 (2012).
- 10 X. Qian, A. Tucker, E. Gidcumb, J. Shan, G. Yang, X. Calderon-Colon, S. Sultana, J. Lu, O. Zhou, D. Spronk, F. Sprenger, Y. Zhang, D. Kennedy, T. Farbizio, Z. Jing, "High resolution stationary digital breast tomosynthesis using distributed carbon nanotube x-ray source array," *Med Phys* **39**, 2090 (2012).

- 11 F. Sprenger, X. Calderon-Colon, E. Gidcumb, J. Lu, X. Qian, D. Spronk, A. Tucker, G. Yang, O. Zhou, "Stationary digital breast tomosynthesis with distributed field emission x-ray tube," Proc. SPIE **7961**, (2011).
- 12 A.W. Tucker, J. Lu, O. Zhou, "Dependency of image quality on system configuration parameters in a stationary digital breast tomosynthesis system," Med Phys **40**, 031917-031910 (2013).
- 13 X. Qian, R. Rajaram, X. Calderon-Colon, G. Yang, T. Phan, D.S. Lalush, J. Lu, O. Zhou, "Design and characterization of a spatially distributed multibeam field emission x-ray source for stationary digital breast tomosynthesis," Med Phys **36**, 4389-4399 (2009).
- 14 G. Yang, R. Rajaram, G. Cao, S. Sultana, Z. Liu, D. Lalush, J. Lu, O. Zhou, "Stationary digital breast tomosynthesis system with a multi-beam field emission x-ray source array," Proc. SPIE **6913**, (2008).
- 15 O.Z. Zhou, G. Yang, J. Lu, D. Lalush, "Stationary x-ray digital breast tomosynthesis systems and related methods," US Patent No. US7751528 B2 (Jul 6, 2010 2010).
- 16 B. Ren, C. Ruth, T. Wu, Y. Zhang, A. Smith, L. Niklason, C. Williams, E. Ingal, B. Polischuk, Z. Jing, "A new generation FFDm/tomosynthesis fusion system with selenium detector," Proc. SPIE **7622**, (2010).
- 17 J. Kuo, P.A. Ringer, S.G. Fallows, P.R. Bakic, A.D. Maidment, S. Ng, "Dynamic reconstruction and rendering of 3D tomosynthesis images," Proc. SPIE **7961**, (2011).
- 18 E. Shaheen, N. Marshall, H. Bosmans, "Investigation of the effect of tube motion in breast tomosynthesis: continuous or step and shoot?," Proc. SPIE **7961**, (2011).
- 19 N. Marshall, H. Bosmans, "Measurements of system sharpness for two digital breast tomosynthesis systems," Physics in medicine and biology **57**, 7629 (2012).

CHAPTER 10: FEASIBILITY OF S-DBT AS A SCREENING TOOL FOR PATIENTS WITH AUGMENTATION MAMMOPLASTY

10.1 Overview

Purpose: Current practices for mammography screening of patients with augmentation mammoplasty results in increased radiation dose, examination time, and discomfort compared to patients without implants. The purpose of this research is to investigate the feasibility of using s-DBT as a screening tool for patients who have undergone augmentation mammoplasty.

Methods: Six implant models were created using Natrelle brand implants from Allergan, Inc. (Irvine, CA) and slabs from a BR3D phantom (CIRS Model 020). The BR3D phantom consists of a target slab which contains specs (0.130 to 0.400 mm in diameter) arranged in clusters, fibers (10 mm in length and 0.15 to 0.60 mm in diameter), and spheroidal masses (1.80 to 6.32 mm in diameter). Each model was imaged three times on both the s-DBT system and a Hologic Selenia Dimensions (Bedford, MA) in 2D mammography mode. The same entrance dose was used between the two modalities. After collection of the images, two readers viewed the datasets and counted the number of visible lesions.

Results: For reader 1, the number of masses, fibers, and spec clusters visible in the s-DBT reconstructions was significantly more in 5, 6, and 2 of the 6 configurations respectively. For reader 2, the number of masses, fibers, and spec clusters visible in the s-DBT reconstructions was significantly more in 4, 6, and 3 of the 6 configurations respectively.

Conclusions: The preliminary results suggest that s-DBT could be used as an alternative to 2D mammography for imaging patients with augmentation mammoplasty. However, additional readers are needed to have a definitive result for the study.

10.2 Motivation for Implant Imaging

In recent years, there has been a large increase in the number of women electing to undergo augmentation mammoplasty. From 2000 to 2011 the number of women undergoing augmentation annually in the USA increased from 212,500 to 307,180.¹²¹ As more women undergo augmentation, there becomes a greater need to effectively screen and diagnose these women for breast cancer. Current screening mammography practices use a four view method for screening patients with breast implants. Two Craniocaudal (CC) views and two Mediolateral Oblique (MLO) views are taken for each breast. For the two CC and MLO views one contains the implant in the Field of View (FOV) of the detector and one contains only breast tissue with the implant pushed out of the FOV of the detector. The latter of the two techniques, as first described by Eklund et al.,¹²² displaces the implant posteriorly against the chest wall while pulling the breast tissue over and anteriorly to the implant. This technique results in a twofold increase in the radiation exposure given to the patient. Eklund et al.¹²² also reported that in 15-20% of the women little information is gained from using the technique. In this group of women, significant encapsulation of the implant by the surrounding breast tissue had occurred. In severe cases the encapsulation led to an increase in pain when the "pushback" technique was attempted. A later report by Silverstein et al.,¹²³ using the aforementioned "pushback" technique, states that the technique resulted in increased visibility of the breast tissue surrounding implants. Encapsulation of the implants again limited the use of the "pushback" technique in some women. Another study, performed by Colville et al.,¹²⁴ reported that using the Eklund¹²² method results in up to a three times increase in the length of time required to complete a screening mammogram when compared to a typical two view mammogram. On average, a screening mammogram can be completed in 5 minutes while a mammogram performed on a patient with implants requires at least 15 minutes. This large increase in time reduces patient throughput significantly in busy screening locations.

The ability of 2D mammography to be an effective screening tool for patients with implants is hindered by the overlapping of the implant with the tissue above and below in the images. Digital Breast Tomosynthesis (DBT) is an effective tool for screening patients due to its ability to visualize tissue in a particular plane with little to no overlap of tissue from other planes.⁶⁻⁹ However, motion of the X-ray source during image acquisition degrades image resolution and quality in rotating gantry DBT systems.^{11, 125} This effect is amplified for tomosynthesis imaging of patients with augmentation due to longer X-ray exposure times. We have developed a stationary Digital Breast Tomosynthesis (s-DBT) system using a linear Carbon Nanotube (CNT) X-ray source array, which allows for acquisition of full tomosynthesis datasets without X-ray source motion.^{13, 119} Zero source motion allows for a substantial increase in spatial resolution when compared to continuous motion DBT systems.¹³ The purpose of this research is to investigate the feasibility of using s-DBT as a screening tool for patients who have undergone augmentation mammoplasty. We are exploring the feasibility of reducing the four views used currently to two s-DBT views, one CC view and one MLO view, for each breast or possibly just a single s-DBT MLO view. This would reduce the amount of radiation to the patient, time of exam, and patient discomfort.

10.3 Methods

Six implant models were created using Natrelle brand implants from Allergan, Inc. (Irvine, CA) and slabs from a BR3D phantom (CIRS Model 020). The BR3D phantom consists of a target slab which contains specs (0.130 to 0.400 mm in diameter) arranged in clusters, fibers (10 mm in length and 0.15 to 0.60 mm in diameter), and spheroidal masses (1.80 to 6.32 mm in diameter). Each model was imaged three times on both the s-DBT system and a Hologic Selenia Dimensions (Bedford, MA) in 2D mammography mode. The same entrance dose was used between the two modalities. After collection of the images, two readers viewed the datasets and counted the number of visible lesions.

10.3.1 Augmentation Mammoplasty Models

In order to simulate breast tissue and lesions a BR3D breast tomosynthesis phantom (CIRS Model 020) was used. The phantom consists of 6 slabs of heterogeneous breast equivalent material. One slab (target slab) contains specs (0.130 to 0.400 mm in diameter) arranged in clusters, fibers (10 mm in length and 0.15 to 0.60 mm in diameter), and spheroidal masses (1.80 to 6.32 mm in diameter). Implants were modeled using Natrelle brand implants from Allergan, Inc. (Irvine, CA). Two saline implants (Style 68: Size 200 and 400cc) and one gel silicone implant (Style 20: Size 200cc) were used.

Both the BR3D phantom slabs and the three implants were used to create six different models of patients with augmentation mammoplasty. Each model either utilized two or four BR3D phantom slabs, one of which was the target slab. **Table 13** shows each combination of implant and number of BR3D slabs used in the study. The BR3D slabs were put both above and below each of the implants. **Figure 49** shows a model with two slabs and the 200cc saline implant under compression on the s-DBT system.



Figure 49: Augmentation mammoplasty model under compression. Two BR3D phantom slabs and the 200cc saline implant were used in the above model.

10.3.2 Imaging Configuration

All six augmentation mammoplasty models were imaged on a Hologic Selenia Dimensions DBT system using 2D planar imaging and on the s-DBT system using tomosynthesis imaging. Each model was imaged three different times on each system for added statistics. The entrance dose used on each model was determined from the exposure index output of the Selenia Dimensions 2D images. An anode voltage and exposure (kV/mAs) combination for an exposure index between -35 and -25 was determined for each model (0.050 mm thick Rh filter was used for all 2D images). An entrance dose at 4 cm was determined using a dosimeter (Radcal Accu-Pro 9096) and ion chamber (Radcal 10x6-6M Mammography Ion Chamber Sensor) for each kV/mAs combination. Using the same dosimeter and ion chamber the exposure values were calculated for the s-DBT system using the same anode voltage for each entrance dose value. Exposure values (mAs) do not correspond directly between the two systems due to differences in filtration. **Table 13** shows the kV/mAs combinations used for each model.

Table 13: Imaging configurations for each augmentation mammoplasty model used. Each configuration corresponds to an exposure index between -35 and -25 on the Selenia Dimensions in 2D imaging mode.

Implant Type/Size (cc)	Number of BR3D slabs	Object Thickness (cm)	Anode Potential (kVp)	Selenia Dimensions Exposure (mAs)	s-DBT Total Exposure (mAs)	Entrance Dose at 4 cm (mR)
Saline/200	2	4.7	28	120	105	513
Saline/200	4	6.7	32	160	128	944
Saline/400	2	5.2	30	120	98	611
Saline/400	4	7.2	33	160	128	1010
Silicone/200	2	4.7	35	120	90	855
Silicone/200	4	6.7	35	180	135	1283

The imaging configuration used on the s-DBT system was 23 projection images with evenly distributed mAs over a 28 degree span. The first four and last four projection images had an angular spacing of 2 degrees and the central 15 projections had an angular spacing of 1 degree. The higher projection density on the central 15 projections was used in order to reduce artifacts from the edge of the implants. A lower projection density was used on the outside 8

projections in order to decrease the z-axis artifact spread and maintain the same entrance dose as the 2D planar images.

10.3.3 Image Processing and Reconstruction

All images were corrected for beam non-uniformity and gain offset. Pseudo-3D reconstruction volumes were constructed using a dynamic 3D reconstruction software package developed by Real Time Tomography, LLC (Villanova, PA) (RTT). The software package uses a back projection filtering method.¹⁰² All 3D reconstructions had a pixel size of 100 μm at the detector and a distance between slices of 0.5 mm.

Post processing filtering of the 2D images was completed using the standard proprietary filter set on the Selenia Dimensions. Post processing filtering of the s-DBT reconstructions was completed with proprietary filters developed by RTT.

10.3.4 Image Analysis

All datasets were reviewed by trained radiologists (minimum of 1 year of residency in a radiology field). The radiologist was asked to record the smallest visible structure of each lesion type (specs, fibers, and masses) for both the planar and s-DBT datasets. The radiologist scored the images based on the smallest structure visualized. A score of 1 was given if only the largest structure was visible and a score of 0 was given if no structures were visible. In all, there were 6 masses, 7 fibers, and 6 spec clusters. In order for a spec cluster to be considered visible at least one spec in the cluster must have been visible. **Figure 50** demonstrates an s-DBT reconstructed slice and a 2D planar image of the model with the 400cc saline implant and two BR3D slabs. **Figure 51**, **Figure 52**, **Figure 53**, and **Figure 54** are zoomed in comparison images of regions I, II, III, and IV from the two systems respectively.

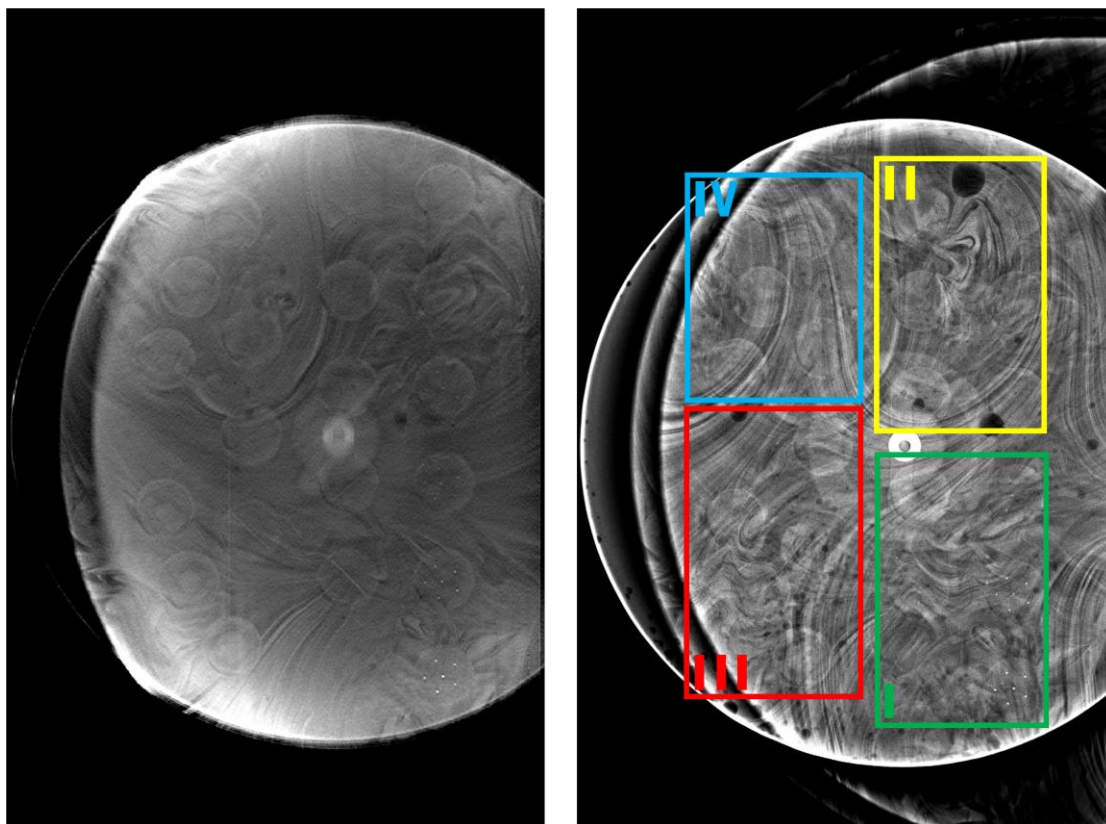


Figure 50: **Left** - s-DBT reconstructed slice through the lesions of the model with the 400cc saline implant and two BR3D slabs. **Right** - 2D planar image of the same model. A large amount of tissue overlap can be seen in the 2D planar image.

* Square regions of interest denote enlarged regions in Figures 4 through 7.

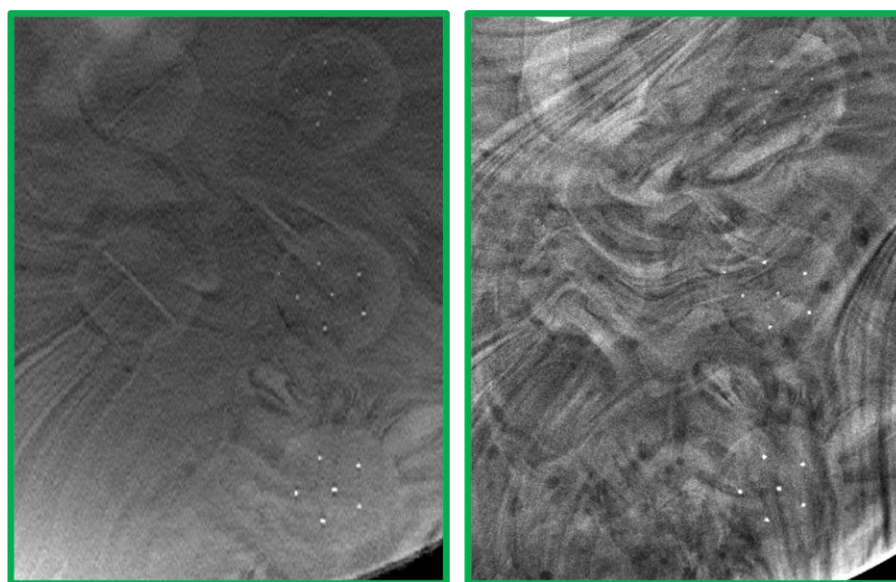


Figure 51: Region I **Left** - s-DBT reconstruction slice **Right** - 2D planar image

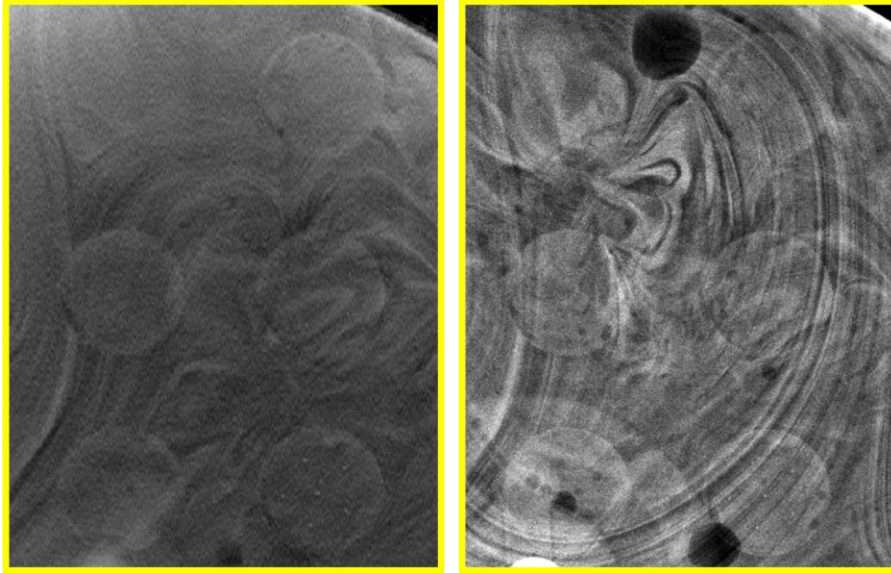


Figure 52: Region II **Left** - s-DBT reconstruction slice **Right** - 2D planar image

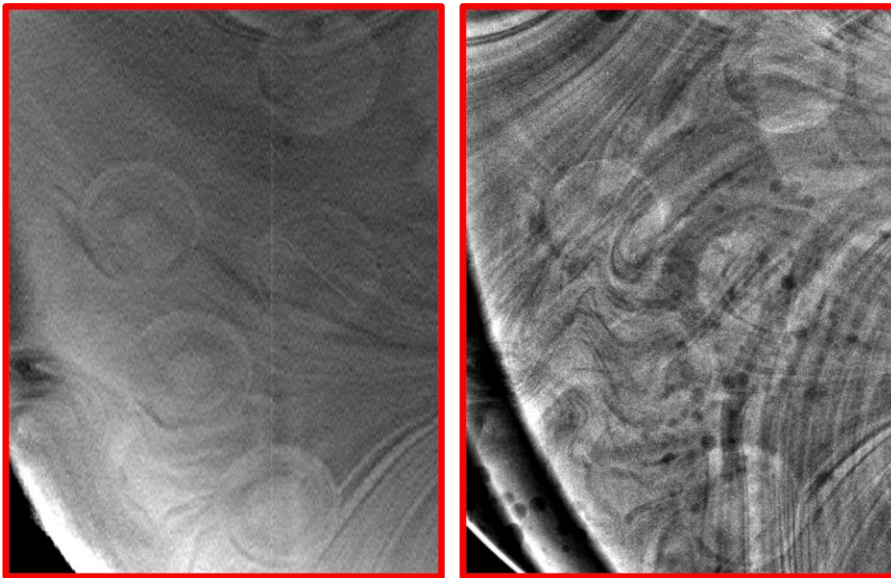


Figure 53: Region III **Left** - s-DBT reconstruction slice **Right** - 2D planar image

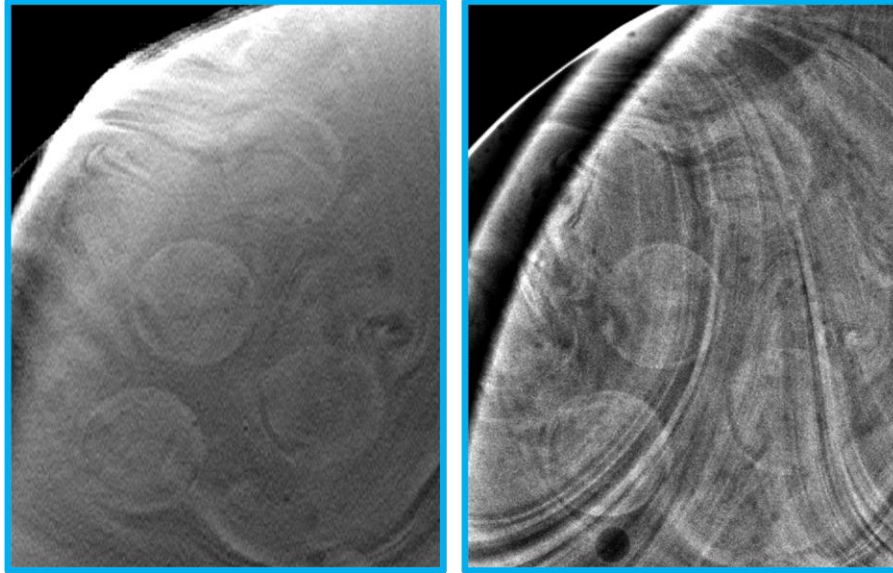


Figure 54: Region IV **Left** - s-DBT reconstruction slice **Right** - 2D planar image

10.4 Results

Two readers viewed all 36 datasets. The results of the reader study can be found in **Table 14**. The values in the table come from the average of the three instances of each implant configuration. Overall averages could not be used since each implant configuration could have significantly different numbers of lesions. Different data from different readers was not averaged due to the small number of readers.

Table 14: Average number of lesions counted by reader one and two for both imaging modalities. The configuration number is related to the implant model and will be used in later plots for ease of implementation.

Reader	Config #	Type /Size (cc)	# Slabs	Masses (6 total)		Fibers (7 total)		Spec Clusters (6 total)	
				s-DBT	2D	s-DBT	2D	s-DBT	2D
1	1	Saline /200	2	3.00± 0.00	2.00± 1.00	4.67± 0.58	1.33± 0.58	4.67± 0.58	5.33± 0.58
1	2	Saline /200	4	3.67± 0.58	0.00± 0.00	3.67± 1.15	0.00± 0.00	4.67± 0.58	5.00± 0.00
1	3	Saline /400	2	3.00± 0.00	2.00± 0.00	4.67± 0.58	0.67± 0.58	5.00± 0.00	5.33± 0.58
1	4	Saline /400	4	4.00± 1.00	0.00± 0.00	3.00± 1.00	0.00± 0.00	4.33± 0.58	4.00± 1.00
1	5	Silicone /200	2	3.00± 0.00	0.67± 1.15	3.67± 0.58	0.67± 1.15	4.67± 0.58	3.33± 0.58
1	6	Silicone /200	4	3.33± 0.58	0.00± 0.00	2.33± 0.58	0.00± 0.00	4.00± 0.00	2.67± 0.58
2	1	Saline /200	2	3.67± 0.58	2.33± 0.58	5.00± 0.00	2.00± 0.00	4.33± 0.58	4.00± 0.00
2	2	Saline /200	4	3.33± 0.58	1.67± 0.58	4.00± 0.00	0.00± 0.00	4.33± 0.58	3.00± 0.00
2	3	Saline /400	2	3.33± 0.58	2.67± 1.15	4.33± 0.58	0.67± 0.58	5.00± 0.00	5.00± 0.00
2	4	Saline /400	4	3.67± 0.58	1.00± 1.00	4.67± 1.53	0.33± 0.58	4.00± 0.00	3.00± 1.00
2	5	Silicone /200	2	3.00± 0.00	2.00± 1.00	4.00± 1.00	1.33± 0.58	4.00± 1.00	2.33± 0.58
2	6	Silicone /200	4	3.67± 0.58	0.00± 0.00	3.00± 0.00	0.00± 0.00	4.00± 0.00	2.00± 0.00

10.4.1 Masses

There was a total of 6 masses embedded in the BR3D phantom. For reader 1, the number of masses visible in the s-DBT reconstructions was significantly more in 5 of the 6 configurations. There were 3 configurations that reader 1 was unable to find any masses in the 2D mammography datasets. For reader 2, the number of masses visible in the s-DBT reconstructions was significantly more in 4 of the 6 configurations. There was 1 configuration that reader 2 was unable to find any masses in the 2D mammography dataset. **Figure 55** shows a bar chart displaying the average number of masses counted by both readers.

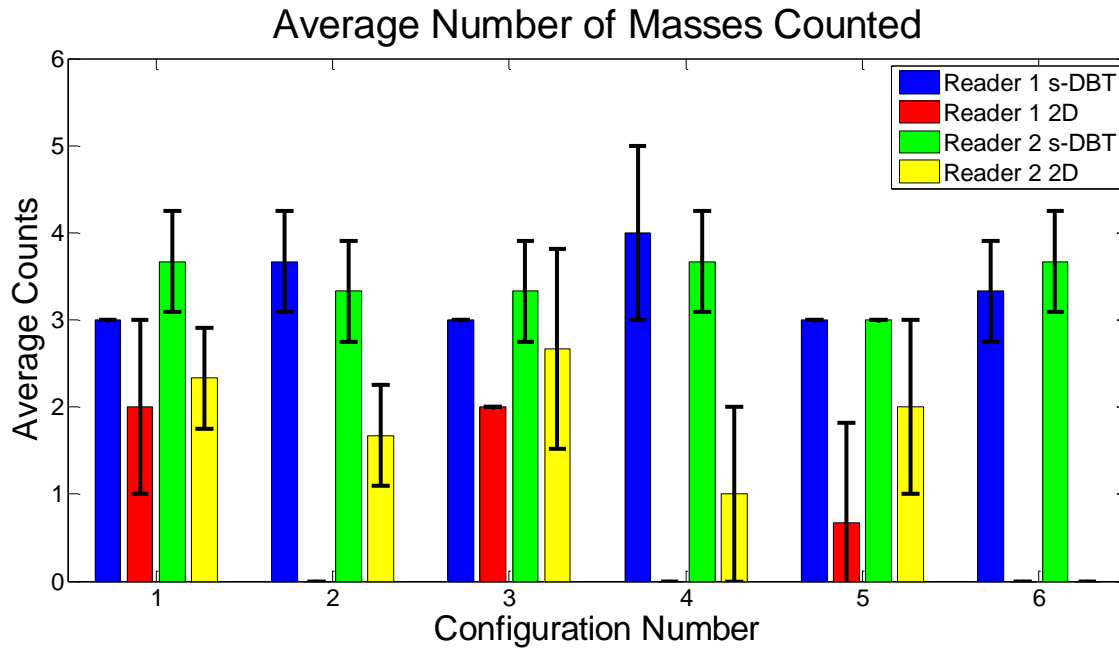


Figure 55: Bar chart showing the average number of masses counted for the 6 implant configuration for both reader one and two. The error bars represent one standard deviation. Missing bars indicate failure to find any lesions.

10.4.2 Fibers

There was a total of 7 fibers embedded in the BR3D phantom. For both readers, the number of fibers visible in the s-DBT reconstructions was significantly more in all 6 configurations. There were 3 configurations that reader 1 was unable to find any fibers in the 2D mammography datasets. There were 2 configurations that reader 2 was unable to find any fibers in the 2D mammography datasets. **Figure 56** shows a bar chart displaying the average number of fibers counted by both readers.

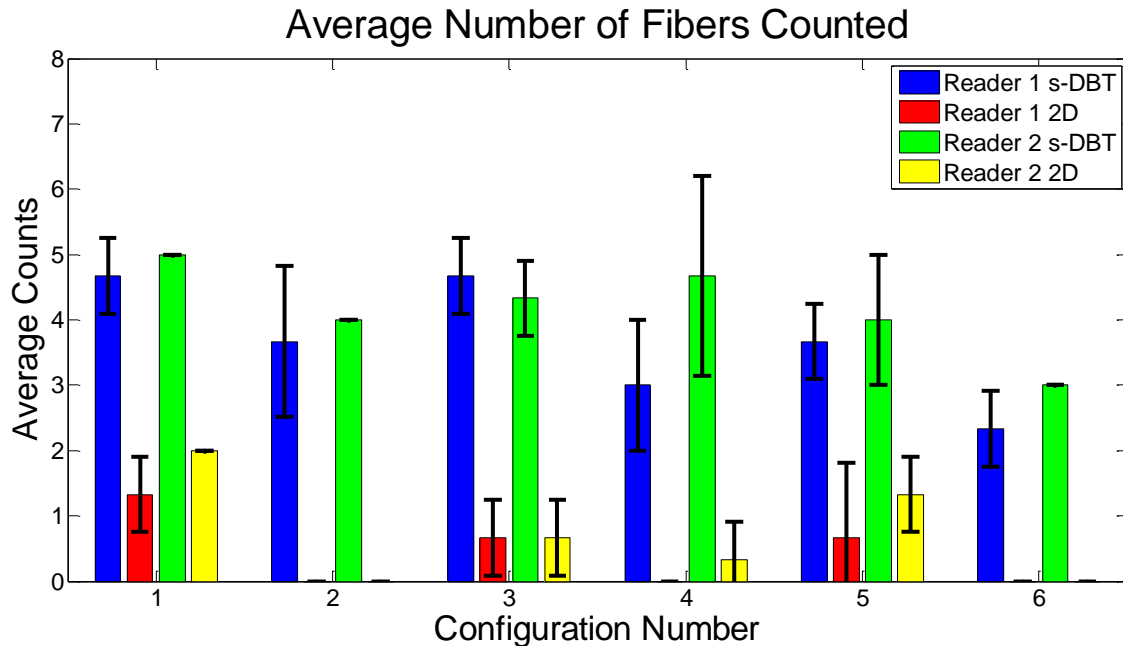


Figure 56: Bar chart showing the average number of fibers counted for the 6 implant configuration for both reader one and two. The error bars represent one standard deviation. Missing bars indicate failure to find any lesions.

10.4.3 Spec Clusters

There was a total of 6 spec clusters embedded in the BR3D phantom. For reader 1, the number of spec clusters visible in the s-DBT reconstructions was significantly more in 2 of the 6 configurations. There were 3 configurations that reader 1 found more spec clusters in the 2D mammography datasets, however this was not significant. For reader 2, the number of spec clusters visible in the s-DBT reconstructions was significantly more in 3 of the 6 configurations.

Figure 57 shows a bar chart displaying the average number of spec clusters counted by both readers.

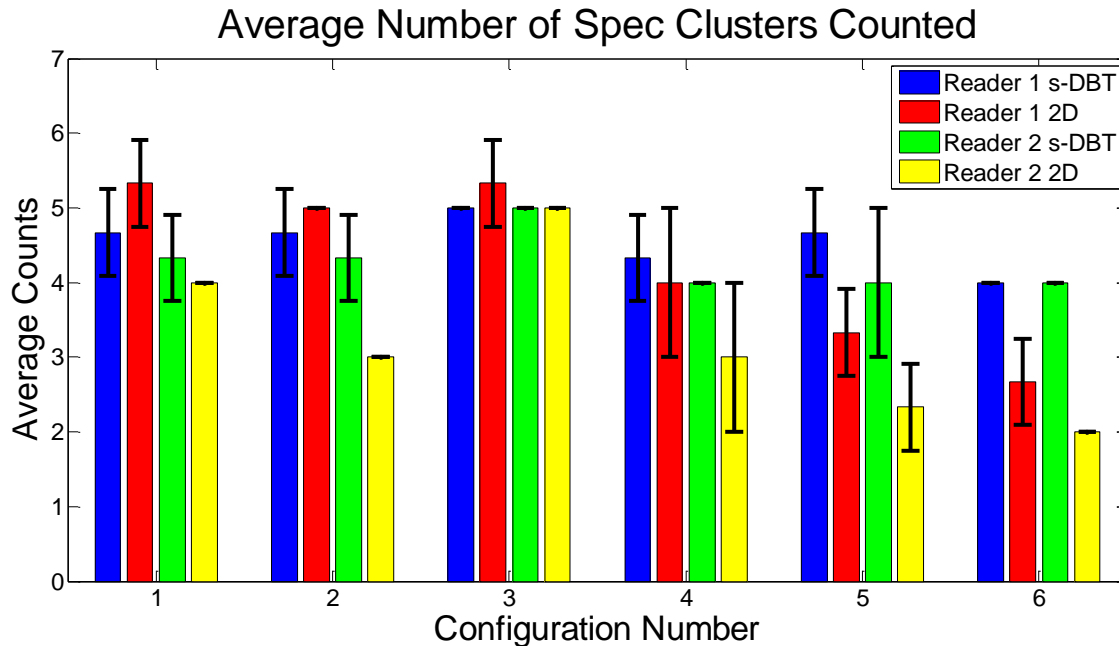


Figure 57: Bar chart showing the average number of spec clusters counted for the 6 implant configuration for both reader one and two. The error bars represent one standard deviation.

10.5 Discussion

Planar images of patients with augmentation mammoplasty contain large amounts of tissue overlap which obscures fibers and masses. The ability of s-DBT to remove tissue overlap in the z-direction resulted in significantly superior visibility of fibers and masses in the reconstructed images. Rotating gantry DBT systems lose spatial resolution from the rotating X-ray source. This reduces microcalcification visibility. An s-DBT system has no motion blurring so is still capable of resolving small microcalcifications. For this reason s-DBT was comparable or superior than 2D mammography in imaging of microcalcifications.

Thinking of the implant as a filter in the datasets means that the datasets are low-dose. The improved image quality of s-DBT over 2D mammography in these low-dose images shows promise for a low-dose tomosynthesis alternative. Current DBT screening examinations utilize both a DBT acquisition and a 2D mammography acquisition. This method is needed due to the poor spatial resolution of rotating gantry DBT systems. The adjunct 2D mammography image essentially doubles the radiation dose to the patient. If the s-DBT system could be used in

mammography screening without a 2D mammography image there could be a possibility of a lower dose than just a 2D mammography image. Further research needs to be conducted to determine the loss in image quality that would occur from a dose reduction.

10.6 Conclusions

This study shows promising results for improved lesion visibility, increased patient throughput, and reduced discomfort and radiation dose to screening mammography patients with augmentation mammoplasty. Additional readers are needed in order to have a definitive conclusion to this study. However, the overwhelming positive results from the first two readers shows great promise that the study will conclude that s-DBT is a feasible alternative to 2D mammography for imaging patients with augmentation mammoplasty. Although the entrance dose to the implants was matched between the two modalities, the two modalities differ in energy spectrums and therefore differ in absorbed dose. Further research into the effect of the differing absorbed doses is needed.

REFERENCES

- 1 A.S.o.P. Surgeons, "Cosmetic Procedure Trends 2012," (2013).
- 2 G. Eklund, R. Busby, S. Miller, J. Job, "Improved imaging of the augmented breast," *American Journal of Roentgenology* **151**, 469-473 (1988).
- 3 M.J. Silverstein, N. Handel, P. Gamagami, E. Waisman, E.D. Gierson, "Mammographic measurements before and after augmentation mammoplasty," *Plastic and reconstructive surgery* **86**, 1126-1130 (1990).
- 4 R.J.I. Colville, C.A. Mallen, L. McLean, N.R. McLean, "What is the impact of breast augmentation on the Breast Screening Programme?," *European Journal of Surgical Oncology (EJSO)* **29**, 434-436 (2003).
- 5 J.T. Dobbins III, D.J. Godfrey, "Digital X-ray tomosynthesis: current state of the art and clinical potential," *Physics in medicine and biology* **48**, R65 (2003).
- 6 A.P. Smith, L. Niklason, B. Ren, T. Wu, C. Ruth, Z. Jing, "Lesion visibility in low dose tomosynthesis," in *Digital Mammography* (Springer, 2006), pp. 160-166.
- 7 S.P. Poplack, T.D. Tosteson, C.A. Kogel, H.M. Nagy, "Digital breast tomosynthesis: initial experience in 98 women with abnormal digital screening mammography," *AJR. American journal of roentgenology* **189**, 616-623 (2007).
- 8 I. Andersson, D.M. Ikeda, S. Zackrisson, M. Ruschin, T. Svahn, P. Timberg, A. Tingberg, "Breast tomosynthesis and digital mammography: a comparison of breast cancer visibility and BIRADS classification in a population of cancers with subtle mammographic findings," *European radiology* **18**, 2817-2825 (2008).
- 9 B. Ren, C. Ruth, J. Stein, A. Smith, I. Shaw, Z. Jing, "Design and performance of the prototype full field breast tomosynthesis system with selenium based flat panel detector," *Proc. SPIE* **5745**, (2005).
- 10 B. Ren, C. Ruth, T. Wu, Y. Zhang, A. Smith, L. Niklason, C. Williams, E. Ingall, B. Polischuk, Z. Jing, "A new generation FFDM/tomosynthesis fusion system with selenium detector," *Proc. SPIE* **7622**, (2010).
- 11 X. Qian, A. Tucker, E. Gidcumb, J. Shan, G. Yang, X. Calderon-Colon, S. Sultana, J. Lu, O. Zhou, D. Spronk, F. Sprenger, Y. Zhang, D. Kennedy, T. Farbizio, Z. Jing, "High resolution stationary digital breast tomosynthesis using distributed carbon nanotube X-ray source array," *Med Phys* **39**, 2090 (2012).
- 12 A.W. Tucker, J. Lu, O. Zhou, "Dependency of image quality on system configuration parameters in a stationary digital breast tomosynthesis system," *Med Phys* **40**, 031917-031910 (2013).
- 13 J. Kuo, P.A. Ringer, S.G. Fallows, P.R. Bakic, A.D. Maidment, S. Ng, "Dynamic reconstruction and rendering of 3D tomosynthesis images," *Proc. SPIE* **7961**, (2011).

CHAPTER 11: CLINICAL IMPLEMENTATION OF AN S-DBT SYSTEM

11.1 Overview

An s-DBT system was constructed for use in a clinical trial. Initial construction was completed in our lab on the campus of UNC-CH. The system was transferred and installed at the North Carolina Cancer Hospital at UNC Hospitals. Once construction was complete the system underwent a series of electrical and radiation safety tests to test if the system was safe for human use. All tests were passed. A protocol for a 100 patient clinical trial was submitted to the Universities IRB and accepted. The system was characterized for various parameters including; geometry, spatial resolution, current versus voltage curves, and radiation dose rates. Once the tube was characterized the resultant values were implemented into the imaging software. The first patient was imaged in December of 2013.

11.2 Motivation for Clinical Implementation

All previous studies conducted using an s-DBT system have involved either computer/physical phantoms or breast specimens. There has been no data collected on actual human patients. In order to further demonstrate the usefulness of s-DBT for breast cancer detection, data must be collected on human patients. A new system will be constructed and installed in the Department of Mammography in the North Carolina Cancer Hospital. After construction of the system, many system values will be characterized and optimized for use on patients. These values include: system geometry, radiation exposure rate based on kVp, spatial resolution, I-V curves. The values will be implemented into the operating software and a radiologist technician will be trained to use the system. Before patients can be recruited and imaged the system must undergo electrical and radiation safety tests. A protocol must also be submitted and approved by the UNC-CH IRB.

11.3 System Construction and Installation

A new Selenia Dimensions DBT system, developed by Hologic Inc. (Bedford, MA), was delivered in Mid year 2012. The base of the gantry was fastened to the floor to ensure it did not topple over during construction. The X-ray tube of the Selenia Dimensions was removed, in March of 2013, with the help of Hologic Engineers. The tube is currently in long term storage. Soon after tube removal, a new CNT source array was delivered to our facility from Xinray Systems, LLC (RTP, NC). The new source array is identical to the previous which is described in full in **Chapter 6**. The tube was mounted onto the gantry of the Selenia Dimensions where the original tube was located. **Figure 58** shows a pictorial time lapse of the Selenia Dimensions gantry during s-DBT system construction.

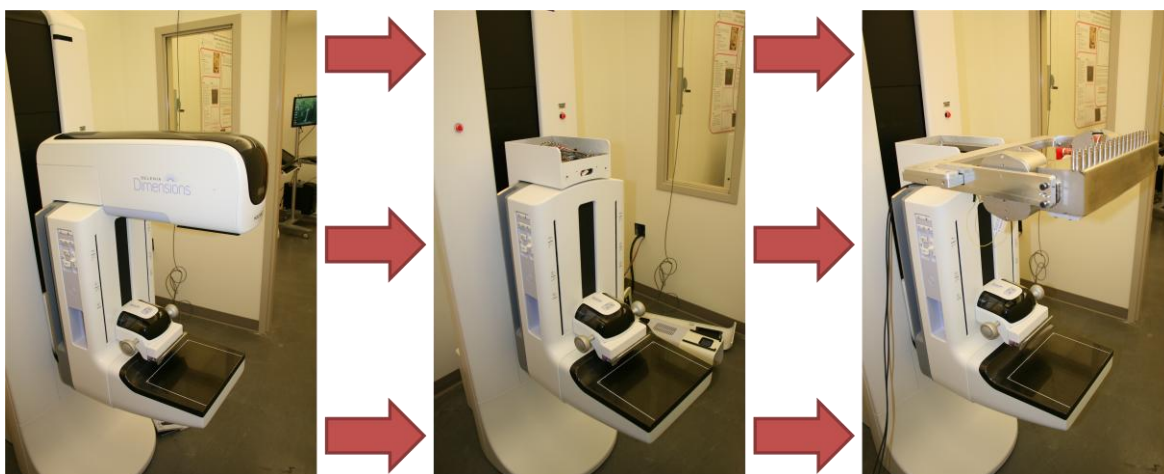


Figure 58: Pictorial time lapse of the Selenia Dimensions gantry (**Left**), after X-ray tube removal (**Center**), and after CNT source array integration (**Right**).

A variety of system components were needed in order for the system to be operational. This included an anode power supply, cathode power supply, and cathode switching system. **Table 15** lists the major power producing components of the system with their specifications. Other components were also integrated into the system including two ion pump controllers, a control computer, a function generator, and an electrical interface for the computer. All components except for the control computer are located in an electronics rack. **Figure 59** shows a picture of the electronics rack with all components labeled.

Table 15: List of major system components other than the X-ray tube in the s-DBT system.

Component	Manufacturer	Model	Voltage Rating (kV)	Current Rating (mA)	Power Rating (W)
Anode Power Supply	Spellman	SL50P2000/220 /1PHASE	50	40	2000
Cathode Power Supply	Heinzinger	PNC 3500-200 neg	-3.5	200	1050
Switching System	H&P Advanced Technologies	ECS	-3	43	129

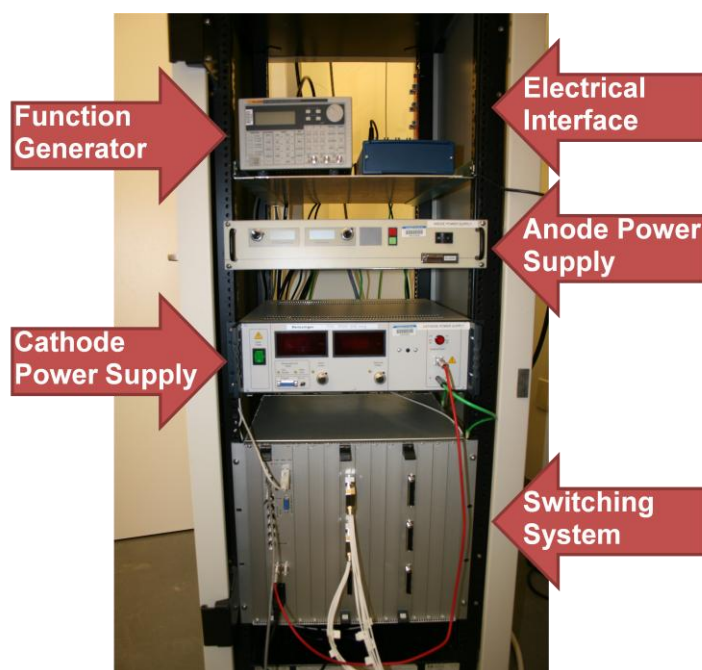


Figure 59: Picture of the electronics rack with all components labeled.

Once the system was constructed, and all components were checked for proper operation, the system was dismantled and transported to the Department of Mammography in the North Carolina Cancer Hospital. The system was put back together in the Cancer Hospital and the gantry was attached to the floor. **Figure 60** shows the fully assembled s-DBT system in the Cancer Hospital.



Figure 60: Picture of the fully assembled s-DBT system in the North Carolina Cancer Hospital at UNC Hospitals.

11.4 Patient and Operator Safety

The safety of the patient and operator were the highest concerns during system construction. Since the system is an investigational device, it does not fall under the FDA guidelines for mammographic devices outlined in the MQSA. However, it was imperative that the MQSA be adhered to as much as possible. For this reason, both electrical and radiation safety tests were conducted on the system before any patient imaging started. Also, the recruitment and imaging protocol for the study had to be approved by the UNC-CH IRB.

11.4.1 Electrical Safety

In order to use the s-DBT system on human patients the system needed to be electrically safe. The electrical grounding scheme and voltage generation isolation were the major items that needed to be addressed to pass an electrical safety test conducted by MET Laboratories Inc. (Baltimore, MD).

It is very important for the electrical grounding of the system to be designed so that any electrical short will not pass through the patient or (to a lesser extent) the switching electronics. High voltage passing through a human can be deadly. Any excessive voltage or current passing through the switching electronics could potentially damage the sensitive electronics inside. The design of the grounding scheme kept these two factors in mind. The shortest path to ground from all the electronics must first pass through the chassis of the anode power supply before going to earth ground. All coaxial cables from the switching system to the X-ray tube have the shielding disconnected on the switching system side of the cable. This prevents any arcs in the X-ray tube from passing directly to the switching system through the cables, which with the shielding intact would create multiple parallel paths to ground. Large diameter multi-core copper cables were used to ground the electronics to ensure short electrical paths to ground. Two cables connect the X-ray tube to the grounding bus in the electronics rack since a large physical distance is between the two components. All grounding cables are coated with a green insulator to distinguish the cables from other cables in the system. **Figure 61** shows a diagram of the grounding scheme used in the system.

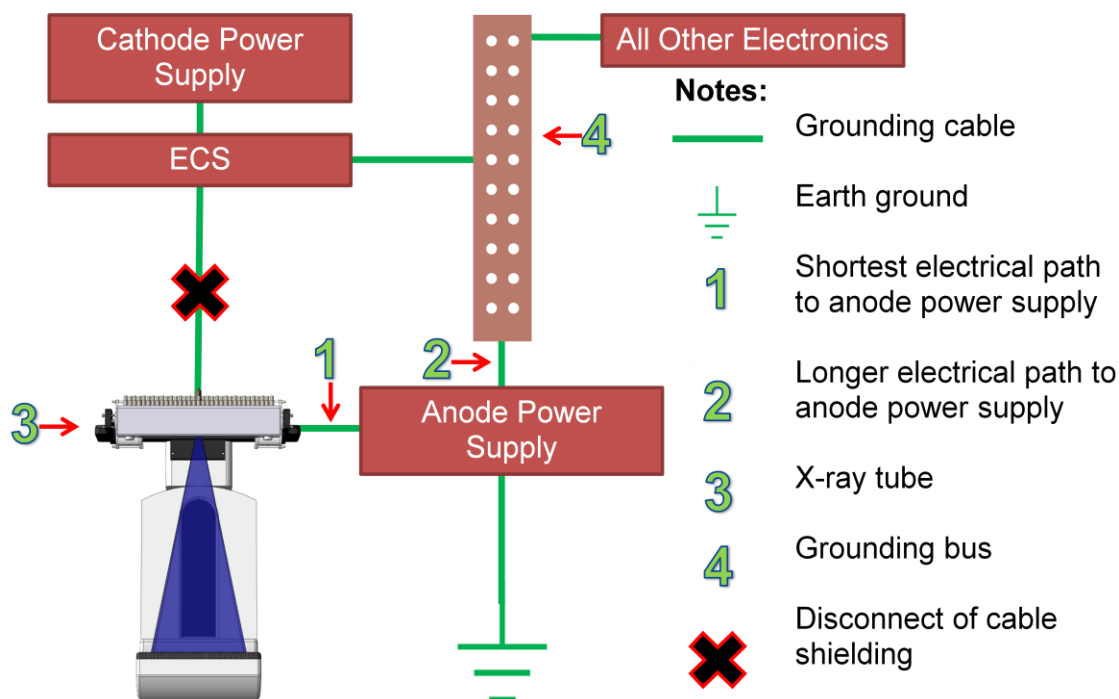


Figure 61: Diagram of the grounding scheme used in the s-DBT system.

In order to use power generating devices on humans they must first be certified for use on humans. None of the power generating devices in the system are certified. However, the system could still pass the electrical safety tests if upstream of the components is an isolation transformer and an in-line ground fault circuit interrupter (GFCI) for over current protection. The intent is to protect the primary of the system in fault conditions and eliminate the possibility of hazards transmitting to the outputs of the device. The peak current draw of each component was measured and recorded except for the anode power supply. The peak current draw of the anode power supply was supplied by the manufacturer of the component and a signed document was given certifying the measurement. **Table 16** shows the peak current draw and electrical ratings for each power generating component. The total apparent power of the three 120V (or 110V) input components equals 334 Va. A medical grade isolation transformer for these components was selected with a max apparent power rating of 1000 Va (Toroid ISB-100W). The transformer was mounted inside the electronics rack. Appropriately rated in-line GFCIs were used for each component. Two other items, the function generator and electrical

interface are also connected to the isolation transformer. Their Apparent Power draw is 14 and 18 Va respectively. They are connected to alleviate the need of foot traffic rated power cords from the components (another electrical safety requirement). A separate isolation transformer was used for the anode power supply. The apparent input power of the anode power supply is approximately 4 kVa. An isolation transformer was selected with a maximum apparent power output of 10 kVa (Sola Hevi-Duty HS14F10BS).. The transformer also steps up the 208 V input voltage to 220 V which is what is recommended for input to the Anode Power Supply. An in-line GFCI was added to the output of the transformer. MET Laboratories passed the system for human use on November 18, 2013.

Table 16: Peak current draw and electrical input ratings for power generating components of the system.

Component	Input Voltage (V AC)	Peak Current Draw (A)	Peak Apparent Power (Va)
Anode power supply	220	18	3960
Cathode power supply	110	2.31	254.1
MicroVac controller	120	0.04	4.8
Switching system	120	0.41	49.2

11.4.2 Radiation Safety

When the s-DBT system is in operation there will be two people present in the room, the patient and the operator. Radiation field survey levels must be below regulatory levels. With the help of the Department of Environmental Health and Safety (EHS), radiation levels were measured in five different locations in and around the room the system is located in. **Figure 62** is the layout of the room in the Cancer Hospital. The numbers in the figure show the five locations that radiation surveys were conducted. All measurements were completed using a full power acquisition on the X-ray tube (39 kVp, 96.75 mAs) with a two slab scatter phantom placed on the detector housing. Location 1 is located one meter in front of the X-ray tube, the dose measured at this distance was 0.58 mR. Location 2 is located where the operator stands during X-ray exposure, there was no measurable radiation dose at this location. Location 3 is located in the adjacent hall in front of the door with the door closed, the measured dose level

was less than the FDA limit. Location 4 and 5 are in the adjacent rooms to the s-DBT system, there was no measurable dose in either location. EHS passed the system for use on humans on October 30, 2013.

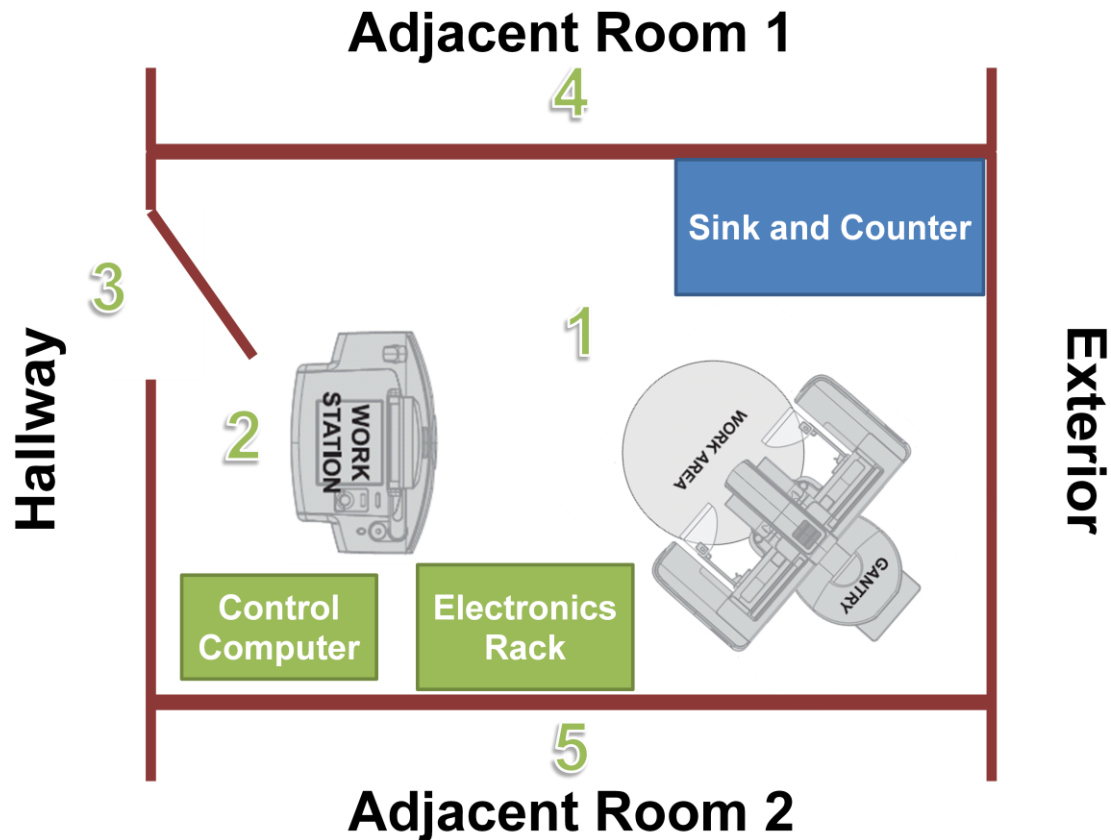


Figure 62: Room layout for the s-DBT system in the UNC-CH Cancer Hospital. The numbers represent locations for radiation field surveys.

11.4.3 Institutional Review Board Approval

A protocol was submitted to the UNC-CH IRB. The protocol outlined recruitment and imaging of 100 patients that had previously been screened at UNC Hospitals and have been called back for diagnostic images. The protocol was approved on January 4, 2013. The study was also registered with the FDA as required by law.

11.5 System Characterization

Before the system can be used on patients it must be characterized for various image quality standards. Geometry calibration and spatial resolution measurements were conducted

on the imaging configuration that will be used on patients. The current versus voltage curves and dose rate of the tube was also determined.

11.5.1 Geometry Calibration

Geometry calibration is needed to determine if the X-ray source is properly aligned to the designed location and for proper image reconstruction. Geometry is conducted using a specially designed phantom which contains strategically placed metal beads. Knowing the physical dimensions of the bead locations, from a X-ray projection image the location of the X-ray source that produced the image can be determined. Using the described method the location of all 15 X-ray sources used for patient imaging was determined. Three different coordinates (x,y,z) were measured for each source with the origin (0,0,0) representing the top left pixel of an image (back right of detector if looking at the front of the system. All measurements are in millimeters. **Figure 63** plots the beam locations with respect to the detector. Assuming the measurements have some error and the manufacturing errors are smaller than the measured errors, then it is beneficial to interpolate the X-ray source locations from the measured locations. It was found that the measured X-ray locations, within the expected error, agreed with the designed values.

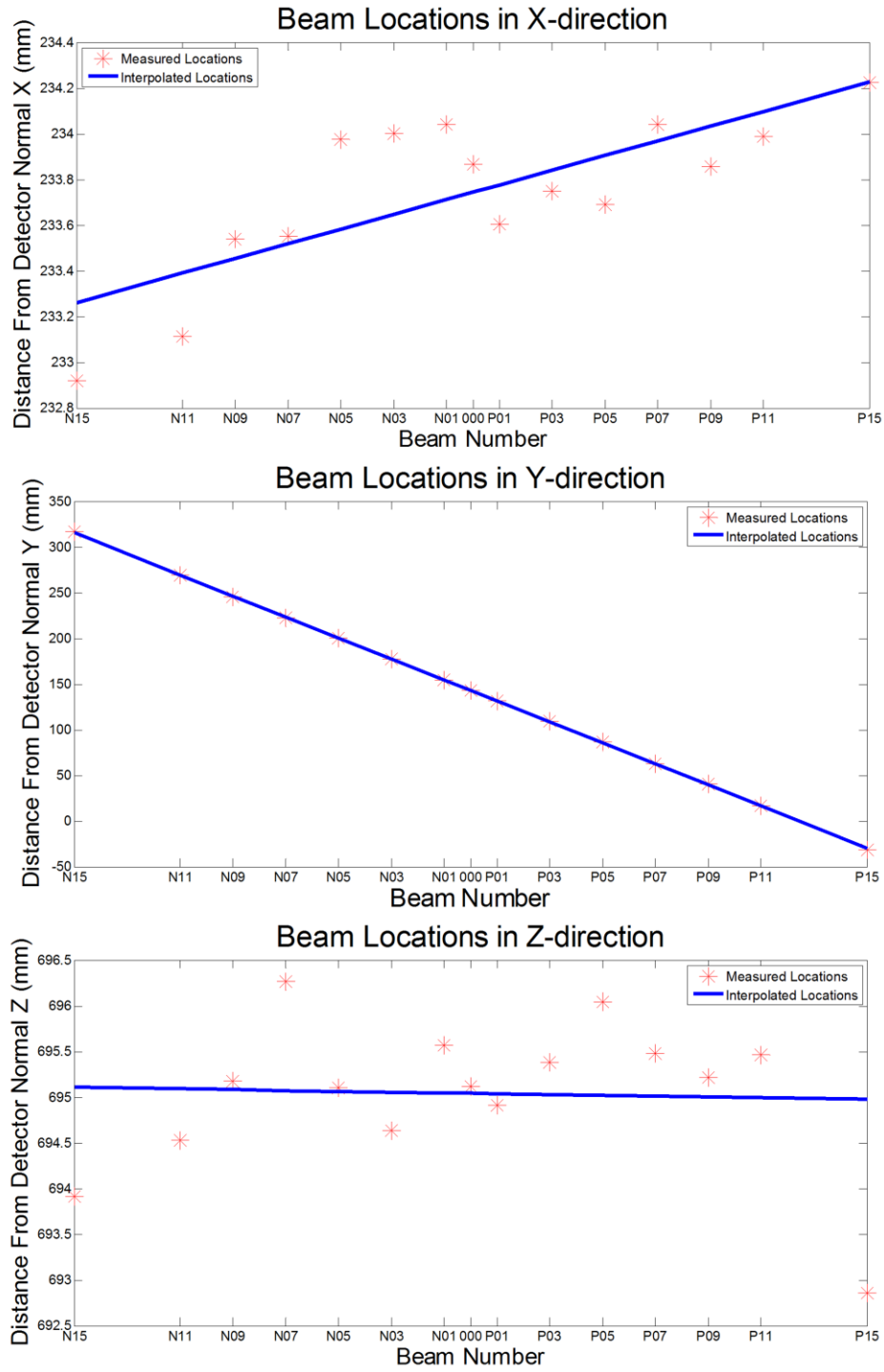


Figure 63: Plots of the x locations (**Above**), y locations (**Middle**), and z locations (**Below**) of the 15 sources used in the clinical trial for patient imaging. Each plot shows the measured beam locations indicated by the red stars and the interpolated locations indicated by the blue lines. All distances are in millimeters.

11.5.2 Spatial Resolution

As designated by the MQSA, the spatial resolution of a mammographic system must be measured by using a line pair phantom. Line pair phantoms consist of a series of angled highly attenuating lines that converge to a point. The highest number of line pairs that are visible from a radiographic image determines the spatial resolution of the system. Since the viewing angle of the focal spot from the detector has an effect on the spatial resolution of the system, the phantom must be placed in a way so that the same viewing angle is used on the entirety of the phantom. For the measurements on the s-DBT system, the phantom was placed so that the line pairs were parallel to the chest wall side of the detector, approximately 20 mm from the chest wall. The images were collected at full power for the clinical trial; 15 beams, 39 kVp, and 97 total mAs. Image reconstruction was completed using a back projection filtering method developed by Real Time Tomography (Villanove, PA USA).¹⁰² No post reconstruction filters were utilized. A reconstruction slice of the phantom with a zoomed in region of interest can be found in **Figure 64**. Looking at the figure it can be seen that the current s-DBT system produces approximately 4 line pairs/mm of spatial resolution, which agrees with previous results from the older s-DBT system.¹³ These images were taken using binned detector pixels, utilizing the full-resolution of the detector would allow for a system resolution of more than 5 line pairs/mm.¹¹⁹

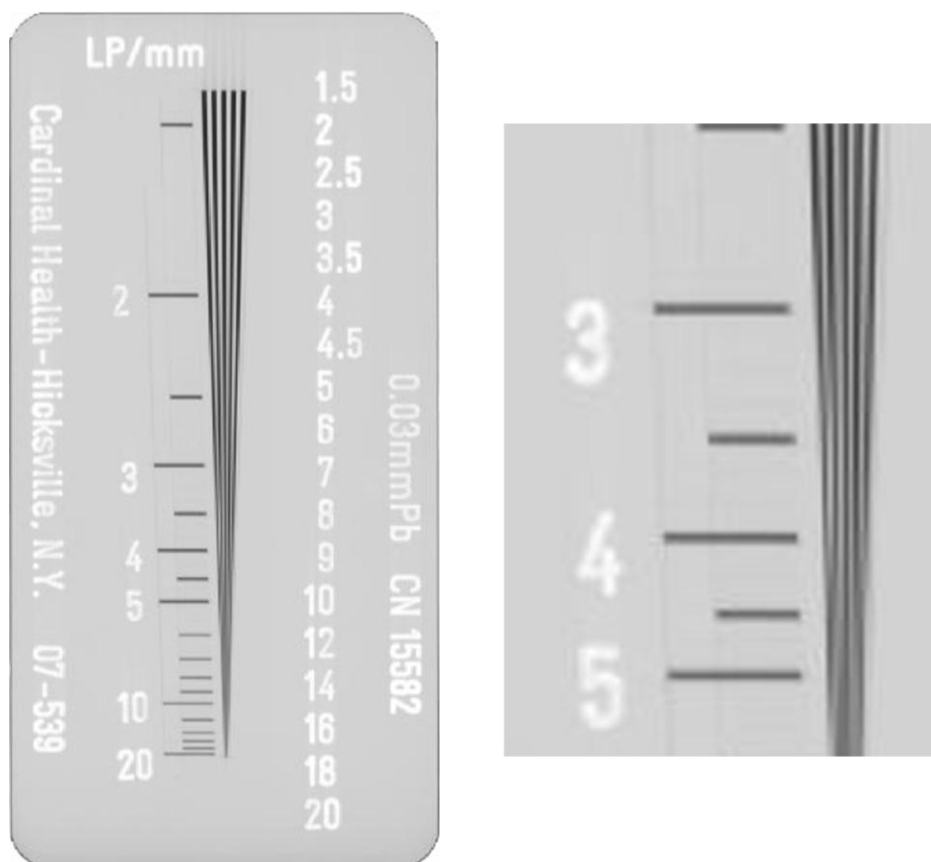


Figure 64: Reconstruction image of the line pair phantom (**Left**). Looking at the zoomed in region (**Right**) it can be seen that the s-DBT system using binned detector pixels produces approximately 4 line pairs/mm of resolution, which agrees with previous measurements on the other s-DBT system.¹³

11.5.3 Current Versus Voltage Curve

The current versus voltage (I-V) curve is a plot of the applied gate-cathode voltage versus the resultant cathode current. It is a good indicator of the performance of a CNT based X-ray source. Since the CNT X-ray sources are setup in a triode design, the gate-cathode voltage at a particular current must be accounted for when calculating the total anode-cathode potential. The I-V curves of the s-DBT system were measured using the output of the ECS, which sends TTL signals with relative peaks related to the applied voltage and resultant current. The ECS is current driven so the wanted current can be input to the system and the voltage will automatically be adjusted to reflect that current within a small error. Currents were selected for each beam ranging from 5 mA to 40 mA in increments of 5 mA. The lowest current achievable by the ECS is 2 mA and the highest used for the clinical trial is 43 mA, so both currents were

also used. Once the data was collected it was fit into an exponential function to reduce the amount of noise. **Figure 65** shows a plot of the I-V curves for the best (P03) and worst cathode (N07). Also in the figure are average curves for the three configurations used in the clinical trial. For a current of 43 mA, the difference in the best and worst cathodes applied voltages is 190 V, which is well within the operating limits of the ECS.

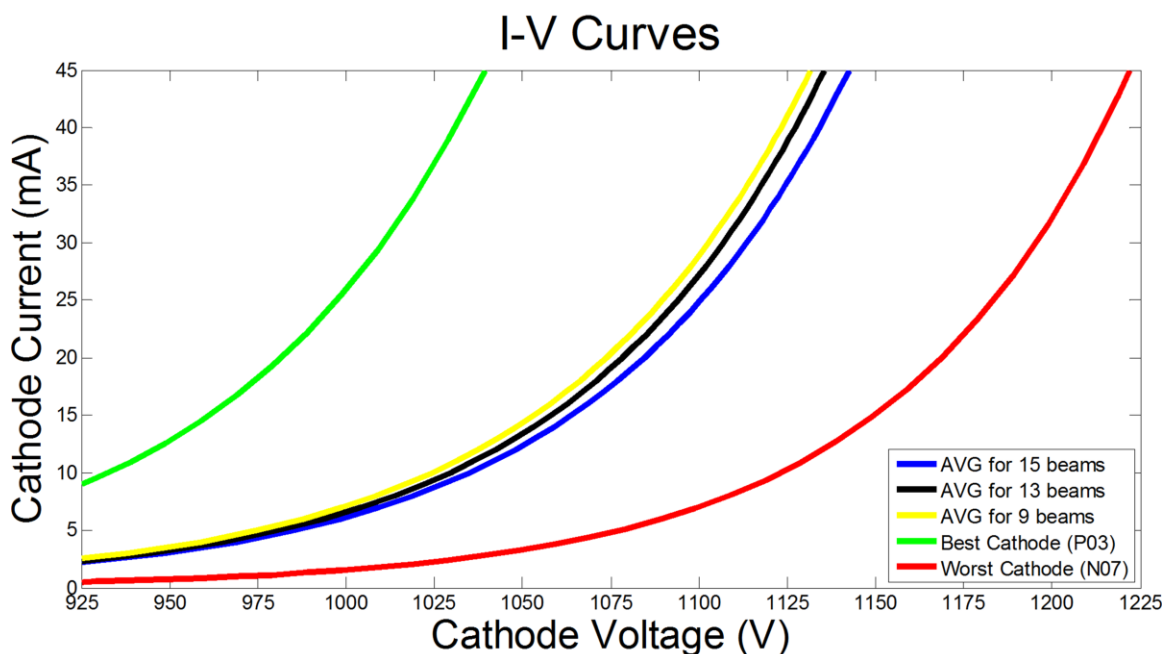


Figure 65: Plot of the average I-V curves for the three configurations used in the clinical trial and the plots for the best and worst cathodes.

11.5.4 Dose Rate

The dose rate for a particular configuration and anode-cathode potential is needed to determine the precise dose given to patients. For the clinical trial, three different configurations were used; (1) 15 beams over 30 degrees, (2) 13 beams over 30 degrees, and (3) 9 beams over 30 degrees. The dose rate was measured using the same technique previously described in **Section 7.3.2**, below the compression paddle and at a height of 4 cm. **Table 17** shows the measured entrance dose and calculated dose rate for the 3 different configurations over a range of anode-cathode potentials. The dose rate versus kVp for each configuration was fit into a third

order polynomial function. Using the functions, the entrance dose for any anode-cathode potential and any configuration can be determined.

Table 17: Measured entrance dose for all three configurations and various anode-cathode potentials. The dose rate was calculated by dividing the entrance dose by the total mAs.

Configuration	Number of Beams	Anode-Cathode Potential (kVp)	Measured Entrance Dose (mR)	Dose Rate (mR/mAs)
1	15	25	61.79	3.19
1	15	30	117.90	6.09
1	15	35	182.40	9.43
1	15	39	238.60	12.33
2	13	25	53.16	3.17
2	13	30	101.90	6.08
2	13	35	157.70	9.40
2	13	39	206.50	12.31
3	9	25	35.73	3.08
3	9	30	68.54	5.90
3	9	35	106.20	9.15
3	9	39	138.90	11.96

11.6 Patient Imaging

After all safety tests were passed and the system was characterized, it was ready for patient imaging. In December of 2013 the first patient was imaged on the s-DBT system. Both a RCC and a RMLO view were taken. **Figure 66** shows the projection images from three beams for the RCC view. **Figure 67** shows the projection images from 3 beams for the RMLO view. **Figure 68** shows reconstruction slices from the RCC and RMLO views.

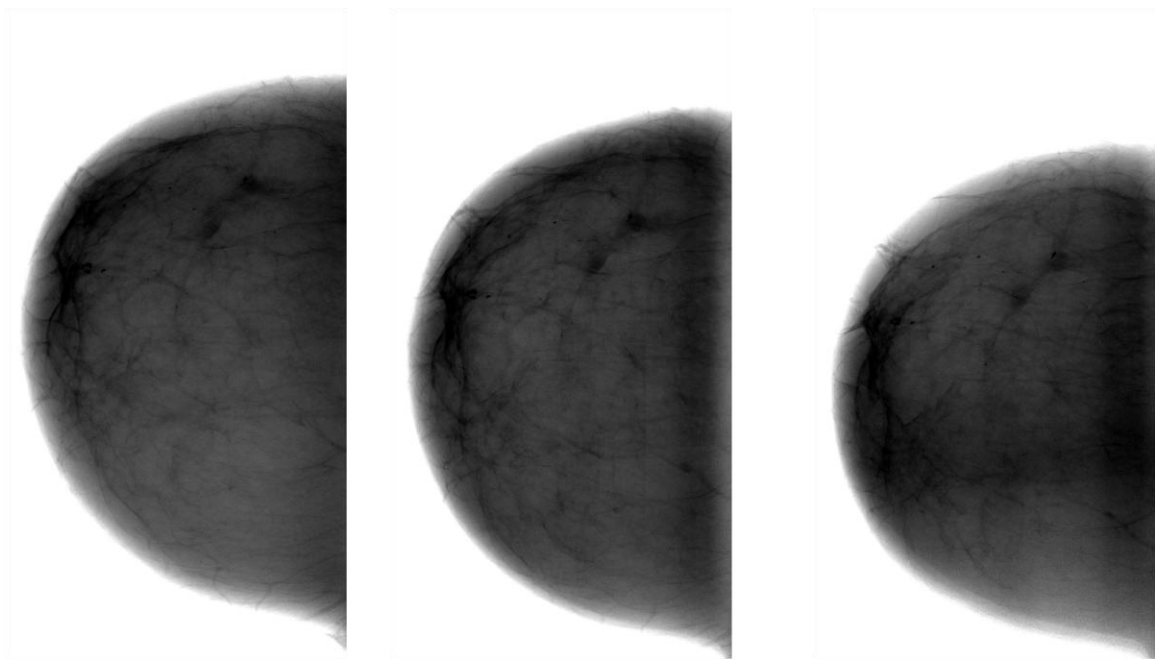


Figure 66: RCC projection images from beams N15 (**Left**), 000 (**Center**), and P15 (**Right**).

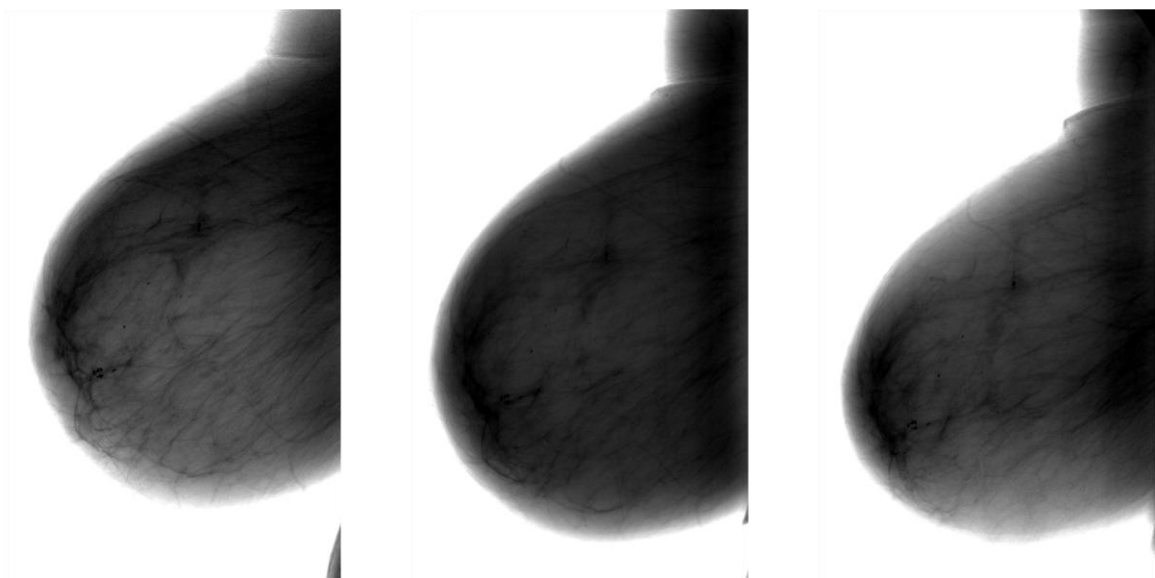


Figure 67: RMLO projection images from beams N15 (**Left**), 000 (**Center**), and P15 (**Right**).

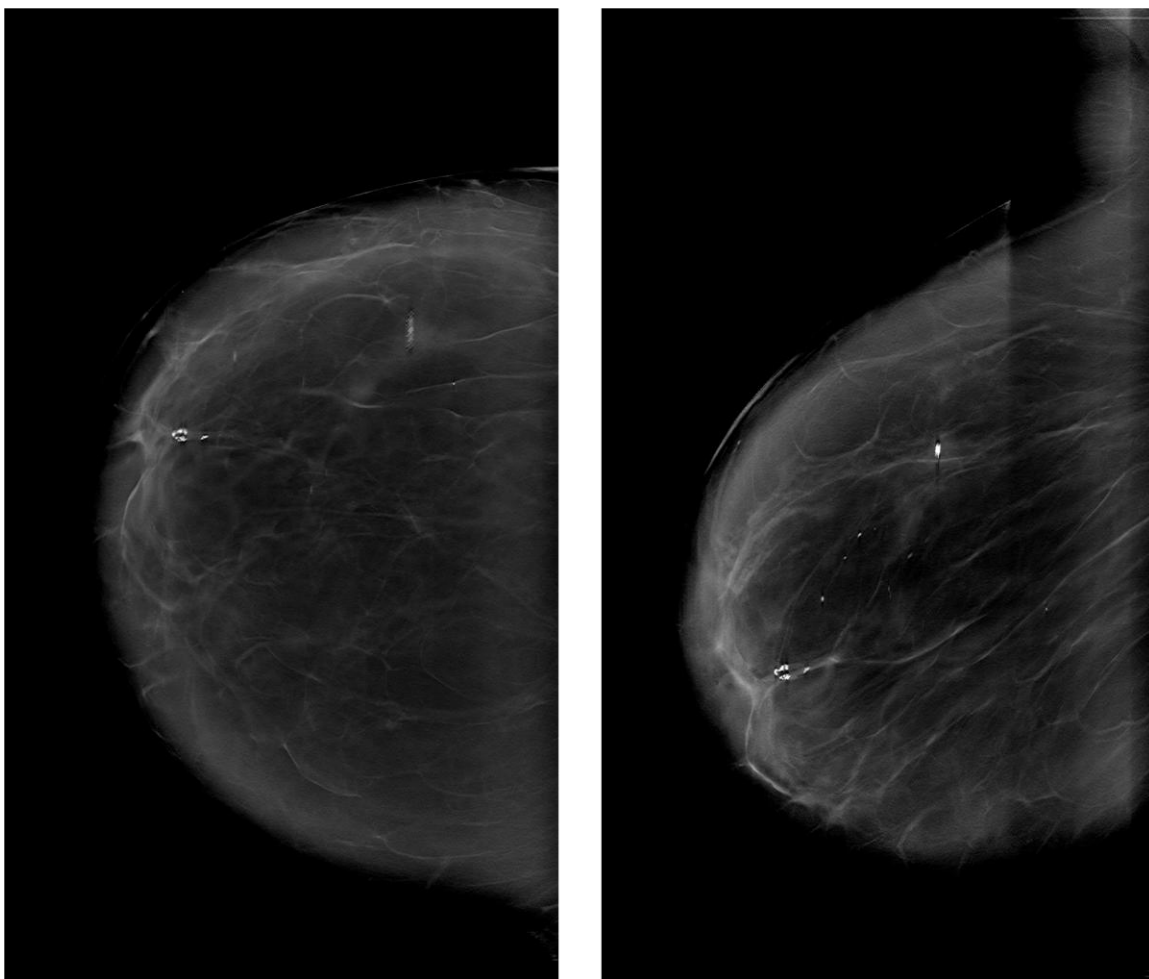


Figure 68: Reconstruction slices from the first patient from the RCC view (**Left**) and the RMLO view (**Right**). Images are in the plane of the large MC cluster on the left portion of the images. The grayscale values of these images are inverted compared to their respective projection images to demonstrate what is typically seen by radiologists.

11.7 Conclusion

A new s-DBT system was constructed and implemented into the Department of Mammography at UNC Hospitals. The system was fully characterized and tested for patient and operator safety. A 100-patient clinical trial is currently underway using the system. The trial will compare the s-DBT reconstruction images with conventional 2D mammography. Currently, two patients have been recruited and imaged.

REFERENCES

- 1 J. Kuo, P.A. Ringer, S.G. Fallows, P.R. Bakic, A.D. Maidment, S. Ng, "Dynamic reconstruction and rendering of 3D tomosynthesis images," Proc. SPIE **7961**, (2011).
- 2 X. Qian, A. Tucker, E. Gidcumb, J. Shan, G. Yang, X. Calderon-Colon, S. Sultana, J. Lu, O. Zhou, D. Spronk, F. Sprenger, Y. Zhang, D. Kennedy, T. Farbizio, Z. Jing, "High resolution stationary digital breast tomosynthesis using distributed carbon nanotube x-ray source array," Med Phys **39**, 2090 (2012).
- 3 A.W. Tucker, J. Lu, O. Zhou, "Dependency of image quality on system configuration parameters in a stationary digital breast tomosynthesis system," Med Phys **40**, 031917-031910 (2013).

CHAPTER 12: SUMMARY AND IMPLICATIONS

12.1 Overview

The original s-DBT system was characterized and optimized using a variety of input parameters. The optimal configuration was found to be one with a large angular span, an intermittent number of projection images, and an even dose distribution. It was also found that the s-DBT system had significantly higher spatial resolution (4 compared to 5 cycles/mm) when operated in unbinned detector mode compared to binned detector mode. After optimization, potential clinical applications were investigated. Specimen images were compared using the s-DBT system and a FFDM system in a reader preference study. This also marked the first human data acquired using the s-DBT system. The data trended toward a preference for the s-DBT system for both masses and surgical margin assessment. FFDM was preferred to s-DBT for imaging of MCs. Another study compared the visualization of MCs in specimen images between the s-DBT system and a continuous motion DBT system. It was found that s-DBT more accurately visualized MCs for every MC analyzed. Higher resolution imaging in the x,y, and z directions is possible with the s-DBT system. The last clinical application for s-DBT investigated was the use for it in screening patients with augmentation mammoplasty. Implant models were created and imaged using the s-DBT system and a FFDM system. Image quality was compared in a two person reader study. Additional readers are needed in order to have a definitive conclusion to this study. However, the overwhelming positive results from the first two readers shows great promise that the study will conclude that s-DBT is a feasible alternative to 2D mammography for imaging patients with augmentation mammoplasty. Finally, a new system was built for use in a clinical trial. The system passed all electrical and radiation safety tests needed for use on patients. A protocol was submitted and accepted by the University's IRB for

an 100 patient clinical trial. The system was characterized and the results were implemented into the operating software. The first patient was imaged in December of 2013.

12.2 Summary of Research

Stationary digital breast tomosynthesis can provide high resolution DBT datasets with a short image acquisition time. This gives the benefit of both the continuous motion DBT systems and the step-and-shoot systems without their inherent disadvantages. This dissertation covered characterization and construction of an s-DBT system as well as potential applications in mammography.

12.2.1 Optimization of an s-DBT System

There has been an exhaustive effort made to characterize and optimize the current DBT systems on the market.¹⁻⁹ Full characterization of medical imaging systems is needed so that appropriate image techniques can be used which optimize image quality per patient while keeping the radiation dose to the patient at a reasonable level. The s-DBT system was characterized and optimized. Five groups of comparison studies were completed: (1) Comparison of 14° versus 28° angular span for a fixed total entrance dose uniformly distributed over 15 projection views; (2) Comparison of 15 versus 29 projection views for a fixed total entrance dose uniformly distributed over an angular span of 28°; (3) For a fixed entrance dose, angular span of 28°, and 29 projection views we compare uniform versus non-uniform distributions of the mAs; (4) For a fixed angular span of 28° and 29 projection views, we varied the total entrance dose from 385 mR to 791 mR; (5) Comparison of image quality for a detector operating in full resolution mode versus 2x2 binning mode. Two physical phantoms were imaged using each configuration. The first phantom was a metal crosswire phantom used for determination of spatial resolution. The second was a mammography ACR phantom which consists of a variety of fibers, masses, and simulated MCs. The resultant projection images were then reconstructed into a pseudo-3D volume and analysis was completed on the

reconstructed slices. The value of the MTF was calculated from the reconstruction of a 50 μm wire phantom. The SdNR and ASF were calculated from the reconstructed images of a mammography accreditation phantom. An overall quality factor (QF) was determined from the three calculated values.

The in-plane resolution, measured by the MTF, was found to primarily depend on the focal spot size of the x-ray source and the detector pixel size. It is insensitive to the number of projection views, projection view angular span, total entrance dose, and mAs distribution. It was found that a uniform distribution resulted in a higher QF than the non-uniform distributions that were tested. A higher entrance dose resulted in better image quality. The number of projection images did not have a large effect on the overall image quality in our phantom study. Increasing the angular span decreases the artifact spread function thus resulting in better image quality. Changing from 2x2 binning to full resolution, in an s-DBT system, results in a 25% increase in the value of the MTF. This increase in spatial resolution comes at the cost of SdNR. A configuration with a large angular span, an intermittent number of projection views, and an even mAs distribution resulted in the best overall image quality and is thus the optimized configuration for the s-DBT system.

12.2.2 Breast Specimen Imaging with s-DBT

Before imaging human patients, the quality of the s-DBT images needed to be evaluated by trained radiologists. For this study, we sought to compare the CNT-based s-DBT system to a FFDM system in a study of breast specimens. This study represents the first human tissue imaging with the novel CNT-based device. Thirty-nine patients, with known breast lesions (BIRADS 4 or 5) from conventional mammography and scheduled for needle localization biopsy were recruited under an institutional review board-approved protocol. After excision from the patient, the specimens were imaged on a GE Senographe FFDM system (General Electric, Fairfield, CT USA) and on the s-DBT system using the optimized imaging

configuration. All specimens were returned to Department of Pathology in the hospital for standard clinical pathology evaluation. A reader study was performed with four breast fellowship-trained radiologists over two separate sessions; all images were viewed in each session. Either the FFDM images or the s-DBT images were shown to the radiologists first. Based off the original modality shown the readers gave a malignancy score between 1 and 5 (1 - benign, 3 - 50% chance of malignancy, 5 - highly malignant) for both masses and MCs in the specimen, and a confidence score for their malignancy diagnosis (0 - 100%). The numeric malignancy score was not based on BIRADS. After malignancy and confidence scores were recorded, the second modality was shown to the reader to determine the readers preference between s-DBT and mammography. Reader preference was recorded between -3 and +3 in increments of one (-3 - 2D preferred, 0 - equally preferred, +3 - s-DBT preferred). Reader preference was recorded for three different categories for each specimen, as applicable; (1) shape/morphology of masses, (2) MC assessment, and (3) margin assessment.

Two of the four readers recorded a higher sensitivity using s-DBT than 2D mammography. Two readers gave higher specificity values for 2D mammography, one gave a higher specificity value for s-DBT, and one reader (Reader 3) did not diagnose any specimens as benign. A reader preference, for masses, of 0.07 ± 1.34 was recorded, where a positive value represents a preference for s-DBT. The difference in the reader preference between the two modalities for masses was insignificant. An average preference of -0.70 ± 0.95 was recorded for MCs, where a negative value represents a preference for 2D mammography. The average preference for margins was 0.16 ± 1.22 , where a positive value represents a preference for s-DBT. A secondary analysis was completed on the reader preference results. It was tested whether the mean reader preference was larger than zero using a linear mixed model with a random intercept effect and Wald test. It was assumed the correlation in reader preference for each specimen between any two readers was the same. The results trended toward a

preference for the s-DBT system in terms of the shape and morphology of masses and margins. It was found that readers preferred FFDM over s-DBT for MC visibility (p-value < 0.05).

The first human data was acquired using the s-DBT system. Stationary digital breast tomosynthesis was found to be comparable with 2D mammography for malignancy diagnosis but readers were significantly more confident in MC visibility when using 2D mammography (p-value < 0.05). Readers, with respect to masses and surgical margins, trended toward a preference for s-DBT. These results were not significant. Given the trend of preference for s-DBT over 2D mammography for both mass visibility and margin assessment, s-DBT could be a viable alternative to 2D mammography for imaging breast specimens.

12.2.3 High Resolution Microcalcification Imaging with s-DBT

Many recent studies have shown that the use of DBT along with a 2D projection image significantly increases sensitivity and decreases the number of false positives in a screening population compared to the 2D projection alone.¹⁰⁻¹⁴ For cases with MCs, there is no significant difference between combo mode and a single 2D projection image.¹⁵ Due to the poor spatial resolution of continuous motion DBT systems, the radiation risk to benefit ratio concerning MCs using combo mode is much higher than 2D mammography alone. In order to lower ratio back to 2D mammography levels a DBT system with high spatial resolution is needed. Lumpectomy specimens were imaged using our s-DBT system and a continuous motion DBT system. Calculations were also made on MCs within the images to determine the effect of the increased spatial resolution. A simulated 3D modulation transfer function (MTF) was created to further show the differences in the spatial resolution of the two systems. Using the results of the MC size comparison, it will be determined if the higher spatial resolution of the s-DBT system translates into increased image quality in the clinic.

All patients were recruited under an University of North Carolina at Chapel Hill Institutional Review Board approved protocol. Twenty-three patients with known breast lesions,

BI-RADS 4 or 5, and scheduled for a lumpectomy procedure were recruited. After excision from the patient, specimens were imaged on the s-DBT system using the optimal configuration and on a Hologic Selenia Dimensions DBT system (Hologic Inc., Bedford, MA) using the normal imaging protocol. Specimen images with MCs were analyzed to further demonstrate the increased resolution of the s-DBT system over the continuous motion DBT system. Twelve individual MCs were selected for analysis. Each MC was analyzed for in-plane resolution (x and y directions) and for the artifact (z direction) spread function (ASF). The MTF was simulated for both systems in the x and y directions and using a detector pixel size of 140 and 70 μm at a focus height of 40 mm.

For every MC analyzed s-DBT had sharper MC localization than continuous motion DBT in the x-y directions. For some MCs, the percent decrease in area from DBT to s-DBT was as high as 43%. For every MC, s-DBT had a narrower ASF than the continuous motion DBT system. The average difference in the FWHM of the ASF was 2.00 ± 0.67 mm. The s-DBT system produces symmetric spatial frequency in every direction on the detector. The Selenia Dimensions produces different spatial frequencies for every non-orthogonal direction. This non-uniformity effect is greatly exaggerated in the 70 μm detector pixel size case. It was found that the s-DBT system gave higher resolution imaging of MCs for every MC analyzed. The stationary design allows for full DBT acquisitions with no motion blur and for large angular spans without an increase in total acquisition time. The high resolution of s-DBT could allow for the removal of the 2D acquisition requirement for DBT screening examinations.

12.2.4 Feasibility of s-DBT as a Screening Tool for Patients with Augmentation Mammoplasty

The ability of 2D mammography to be an effective screening tool for patients with implants is hindered by the overlapping of the implant with the tissue above and below in the images. DBT is an effective tool for screening patients due to its ability to visualize tissue in a particular plane with little to no overlap of tissue from other planes.¹⁶⁻¹⁹ However, motion of the

x-ray source during image acquisition degrades image resolution and quality in rotating gantry DBT systems.^{20, 21} This effect is amplified for tomosynthesis imaging of patients with augmentation due to longer x-ray exposure times. The purpose of this research is to investigate the feasibility of using s-DBT as a screening tool for patients who have undergone augmentation mammoplasty.

Six implant models were created using Natrelle brand implants from Allergan, Inc. (Irvine, CA) and slabs from a BR3D phantom (CIRS Model 020). The BR3D phantom consists of a target slab which contains specs (0.130 to 0.400 mm in diameter) arranged in clusters, fibers (10 mm in length and 0.15 to 0.60 mm in diameter), and spheroidal masses (1.80 to 6.32 mm in diameter). Each model was imaged three times on both the s-DBT system and a Hologic Selenia Dimensions (Bedford, MA) in 2D mammography mode. The same entrance dose was used between the two modalities. After collection of the images, two readers viewed the datasets and counted the number of visible lesions. The radiologist scored the images based on the smallest structure visualized. A score of 1 was given if only the largest structure was visible and a score of 0 was given if no structures were visible. In all, there were 6 masses, 7 fibers, and 6 spec clusters.

There was a total of 6 masses embedded in the BR3D phantom. For reader 1, the number of masses visible in the s-DBT reconstructions was significantly more in 5 of the 6 configurations. There were 3 configurations that reader 1 was unable to find any masses in the 2D mammography datasets. For reader 2, the number of masses visible in the s-DBT reconstructions was significantly more in 4 of the 6 configurations. There was 1 configuration that reader 2 was unable to find any masses in the 2D mammography dataset. There was a total of 7 fibers embedded in the BR3D phantom. For both readers, the number of fibers visible in the s-DBT reconstructions was significantly more in all 6 configurations. There were 3 configurations that reader 1 was unable to find any fibers in the 2D mammography datasets. There were 2 configurations that reader 2 was unable to find any fibers in the 2D mammography

datasets. There was a total of 6 spec clusters embedded in the BR3D phantom. For reader 1, the number of spec clusters visible in the s-DBT reconstructions was significantly more in 2 of the 6 configurations. There were 3 configurations that reader 1 found more spec clusters in the 2D mammography datasets, however this was not significant. For reader 2, the number of spec clusters visible in the s-DBT reconstructions was significantly more in 3 of the 6 configurations.

This study shows promising results for improved lesion visibility, increased patient throughput, and reduced discomfort and radiation dose to screening mammography patients with augmentation mammoplasty. Additional readers are needed in order to have a definitive conclusion to this study. However, the overwhelming positive results from the first two readers shows great promise that the study will conclude that s-DBT is a feasible alternative to 2D mammography for imaging patients with augmentation mammoplasty.

12.2.5 Clinical Implementation of an s-DBT System

All previous studies conducted using an s-DBT system have involved either computer/physical phantoms or breast specimens. There has been no data collected on actual human patients. In order to further demonstrate the usefulness of s-DBT for breast cancer detection, data must be collected on human patients. An s-DBT system was constructed for use in a clinical trial. Initial construction was completed in our lab on the campus of UNC-CH. The system was transferred and installed at the North Carolina Cancer Hospital at UNC Hospitals. Once construction was complete the system underwent a series of electrical and radiation safety tests to test if the system was safe for human use. The electrical grounding scheme and voltage generation isolation were the major items that needed to be addressed to pass an electrical safety test conducted by MET Laboratories Inc. (Baltimore, MD). With the help of the Department of Environmental Health and Safety (EHS), radiation levels were measured in five different locations in and around the room the system is located in. All radiation field surveys were passed. A protocol for a 100 patient clinical trial was submitted to

the Universities IRB and accepted. Before the system could be used on patients it had to be characterized for various image quality standards. Geometry calibration and spatial resolution measurements were conducted on the imaging configuration that will be used on patients. The current versus voltage curves and dose rate of the tube was also determined. Once the tube was characterized the resultant values were implemented into the imaging software. The first patient was imaged in December of 2013.

12.3 Implications

The work completed here has not only optimized the s-DBT system but has shown that it is capable of producing higher quality images than current DBT systems. Even though the system was implemented into the clinic in my research, there still is a great deal of work that could be completed on the current system. The system could be used for other trials designed to show the benefits of the system. Other possible trials include a direct s-DBT to DBT clinical trial, a trial which could show the full benefit of s-DBT for patients with augmentation mammoplasty, and a large screening trial comparing s-DBT to 2D mammography. The current trial is a comparison of s-DBT and 2D mammography for patients with highly suspicious lesions and is not powered toward negative diagnosis. Having a large screening trial would show the benefit not only for diagnosing a positive disease but also for the possible reduction in false-positives. Future studies would be able to characterize all the benefits of the system over current DBT and 2D mammography systems.

An s-DBT system in theory would be an ideal system for screening mammography. Combining the low-dose and high spatial resolution of 2D mammography with the 3D information from tomosynthesis, the system would be able to add a significant amount of information with minimal added risk to the patient. The current iteration of the system improves upon rotating source DBT systems which are currently being used in the clinic. The system not only produces higher spatial resolution images but also is capable of acquiring full sets of

tomosynthesis images in a shorter amount of time, when coupled with a high speed detector. However, the full potential of the technology has not yet been realized. The current system, although fast acquiring and high resolution, could benefit from a redesign of the X-ray source. Utilizing a thinner window, a rotating anode, and a smaller focal spot size, the system could have the potential to acquire images in less than 3 seconds and could have spatial resolution which is extremely close to the levels found in 2D mammography. Although the research here constructed a fully capable system which does improve upon current DBT systems, even more improvement could be made to further help women who are afflicted with this terrible disease.

REFERENCES

- 1 A.S. Chawla, J.Y. Lo, J.A. Baker, E. Samei, "Optimized image acquisition for breast tomosynthesis in projection and reconstruction space," *Med Phys* **36**, 4859-4869 (2009).
- 2 T. Deller, K.N. Jabri, J.M. Sabol, X. Ni, G. Avinash, R. Saunders, R. Uppaluri, "Effect of acquisition parameters on image quality in digital tomosynthesis," *Proc. SPIE* **6510**, (2007).
- 3 Y.-H. Hu, B. Zhao, W. Zhao, "Image artifacts in digital breast tomosynthesis: Investigation of the effects of system geometry and reconstruction parameters using a linear system approach," *Med Phys* **35**, 5242-5252 (2008).
- 4 I. Reiser, R.M. Nishikawa, "Task-based assessment of breast tomosynthesis: Effect of acquisition parameters and quantum noise," *Med Phys* **37**, 1591-1600 (2010).
- 5 B. Ren, T. Wu, A. Smith, C. Ruth, L. Niklason, Z. Jing, J. Stein, "The dependence of tomosynthesis imaging performance on the number of scan projections," in *Digital Mammography* (Springer, 2006), pp. 517-524.
- 6 I. Sechopoulos, C. Ghetti, "Optimization of the acquisition geometry in digital tomosynthesis of the breast," *Med Phys* **36**, 1199-1207 (2009).
- 7 E. Shaheen, N. Marshall, H. Bosmans, "Investigation of the effect of tube motion in breast tomosynthesis: continuous or step and shoot?," *Proc. SPIE* **7961**, (2011).
- 8 W. Zhao, B. Zhao, P.R. Fisher, P. Warmoes, T. Mertelmeier, J. Orman, "Optimization of detector operation and imaging geometry for breast tomosynthesis," *Proc. SPIE* **6510**, (2007).
- 9 J. Zhou, B. Zhao, W. Zhao, "A computer simulation platform for the optimization of a breast tomosynthesis system," *Med Phys* **34**, 1098-1109 (2007).
- 10 D. Bernardi, S. Ciatto, M. Pellegrini, V. Anesi, S. Burlon, E. Cauli, M. Depaoli, L. Larentis, V. Malesani, L. Targa, "Application of breast tomosynthesis in screening: incremental effect on mammography acquisition and reading time," *British Journal of Radiology* **85**, e1174-e1178 (2012).
- 11 G. Gennaro, R.E. Hendrick, P. Ruppel, R. Chersevani, C. di Maggio, M. La Grassa, L. Pescarini, I. Polico, A. Proietti, E. Baldan, E. Bezzon, F. Pomerri, P.C. Muzzio, "Performance comparison of single-view digital breast tomosynthesis plus single-view digital mammography with two-view digital mammography," *European radiology* **23**, 664-672 (2013).
- 12 L. Philpotts, M. Raghu, M. Durand, R. Hooley, R. Vashi, L. Horvath, J. Geisel, R. Butler, "Initial experience with digital breast tomosynthesis in screening mammography," *Proceedings of the 2012 Annual Meeting of the American Roentgen Ray Society*, Vancouver, BC, Canada **29**, (2012).
- 13 P. Skaane, A.I. Bandos, R. Gullien, E.B. Eben, U. Ekseth, U. Haakenaasen, M. Izadi, I.N. Jebsen, G. Jahr, M. Krager, "Comparison of digital mammography alone and digital

- mammography plus tomosynthesis in a population-based screening program," *Radiology* **267**, 47-56 (2013).
- 14 P. Skaane, A.I. Bandos, R. Gullien, E.B. Eben, U. Ekseth, U. Haakenaasen, M. Izadi, I.N. Jebsen, G. Jahr, M. Krager, "Prospective trial comparing full-field digital mammography (FFDM) versus combined FFDM and tomosynthesis in a population-based screening programme using independent double reading with arbitration," *European radiology*, 1-11 (2013).
 - 15 M. Michell, A. Iqbal, R. Wasan, D. Evans, C. Peacock, C. Lawinski, A. Douiri, R. Wilson, P. Whelehan, "A comparison of the accuracy of film-screen mammography, full-field digital mammography, and digital breast tomosynthesis," *Clinical radiology* **67**, 976-981 (2012).
 - 16 J.T. Dobbins III, D.J. Godfrey, "Digital x-ray tomosynthesis: current state of the art and clinical potential," *Physics in medicine and biology* **48**, R65 (2003).
 - 17 A.P. Smith, L. Niklason, B. Ren, T. Wu, C. Ruth, Z. Jing, "Lesion visibility in low dose tomosynthesis," in *Digital Mammography* (Springer, 2006), pp. 160-166.
 - 18 S.P. Poplack, T.D. Tosteson, C.A. Kogel, H.M. Nagy, "Digital breast tomosynthesis: initial experience in 98 women with abnormal digital screening mammography," *AJR. American journal of roentgenology* **189**, 616-623 (2007).
 - 19 I. Andersson, D.M. Ikeda, S. Zackrisson, M. Ruschin, T. Svahn, P. Timberg, A. Tingberg, "Breast tomosynthesis and digital mammography: a comparison of breast cancer visibility and BIRADS classification in a population of cancers with subtle mammographic findings," *European radiology* **18**, 2817-2825 (2008).
 - 20 B. Ren, C. Ruth, J. Stein, A. Smith, I. Shaw, Z. Jing, "Design and performance of the prototype full field breast tomosynthesis system with selenium based flat panel detector," *Proc. SPIE* **5745**, (2005).
 - 21 B. Ren, C. Ruth, T. Wu, Y. Zhang, A. Smith, L. Niklason, C. Williams, E. Ingal, B. Polischuk, Z. Jing, "A new generation FFDM/tomosynthesis fusion system with selenium detector," *Proc. SPIE* **7622**, (2010).